DISS. ETH NO. 19904

Steam Turbine Aerodynamics and Geometry Optimization for Effective Reduction of Leakage Flow Interactions

A dissertation submitted to
ETH ZURICH

for the degree of
Doctor of Sciences

Presented by

Konstantinos G. Barmpalias
Master of Science – Mechanical Engineering
Aristotle University of Thessaloniki, Greece
Born May 2nd, 1980
Citizen of Greece

Accepted on the recommendation of
Prof. Dr. Reza S. Abhari
Prof. Dr. Tadashi Tanuma
Dr. Anestis I. Kalfas

2011

λέγε εἰδὼς

to speak about something only when you know about it

SOCRATES

Acknowledgements

This thesis is the outcome of my work over the last five years at the Laboratory for Energy Conversion at the ETH Zürich. I would like to thank Prof. Reza S. Abhari for giving me the opportunity to work on an interesting and definitely challenging project, continually supported by his management and technical skills. The majority of the meetings we had were at least memorable and there was always a lesson learned. I would also like to thank Prof. Tanuma of the Tokyo university for his precious comments.

Special thanks should go Dr. Anestis I. Kalfas. His support has been continuous over these years on several places across this earth and at all times imaginable. Although he was literally absent our enlighten discussions on all kind of topics greatly assisted me and help me to stay on track.
Dr. Ndaona Chokani is greatly acknowledged. His guidance throughout my stay at the LEC especially at my first steps was of great help to me. This work would not have been possible without the precious know-how transfer of Dr. Peter Schüpbach and the successful collaboration with Philipp Jenny. I am also greatful to all my colleagues at the LEC especially those that I interacted the most. Having cooperated with people from diverse backgrounds on a multi-cultural environment was a unique experience.

The financial support of the Toshiba Corporation is acknowledged. Thanks are due to a number of individuals involved in this research project including Toshio Hirano, Naoki Shibukawa and Takashi Sasaki.

I would also like to express my gratitude to the experienced workshop people of our lab, Cornel Reshef, Thomas Künzle and Hans Suter for their patience and time dedicated to help me on numerous tasks.

My gratitude and appreciation go to my heartiest friend for our endless after work intellectually stimulating discussions on all aspects of life. His easy-going approach on everyday problems is to be remembered. Special thanks go to Anna for all the things we shared together over the last years and for her ever-lasting patience to hear the mechanical approach of solving a problem. Finally I would like to thank my family for supporting me in this effort over the last five years

Abstract

In this work the results of an aerodynamic study of various rotor inlet cavity designs are presented. The modifications were done at the inlet cavity of the second rotor of a two-stage low solidity axial shrouded turbine with the blade geometry being characteristic of a high-pressure stage of a steam turbine. Both the geometry as well as the volume of the cavity were varied, seeking the optimum cavity length scale that would control the cavity flows, minimize the mixing at the interaction zone between the cavity and main flows through alternation of the leakage flow path.

Cavity flows are responsible for generating secondary flows leading therefore to potential loss generation. Shrouded turbines are extensively used in power generation where steam turbines are employed. Although they offer higher efficiency through reduced leakage flows they suffer extensively from thermal loads and mechanical stress on the blade root. However, as they are operated at low rpm they definitely offer an advantage compared to the unshrouded turbines.

An experimental investigation has been carried out to quantify the potential benefit from the various rotor inlet cavity geometrical modifications in terms of stage efficiency gain. The experiments have been conducted at the low-speed research axial turbine of the Laboratory of Energy Conversion (LEC) at ETH Zurich. Both steady and unsteady measurements have been made with the use of in-house developed miniature in size pneumatic (4HP, 5HP) and fast response probes (FRAP) to capture and characterize the unsteady flow field. Additionally, a supplementary computational work has been performed to better visualize the highly unsteady three-dimensional flow field of the turbomachines.

The analysis of the data clearly shows the impact of the rotor inlet cavity geometry on the efficiency. The cavity volume has been modified by changing both the axial as well as the radial cavity wall length. The cavity volume has met a reduction of 14% and 28% compared to the initial cavity volume, which proved to be beneficial in terms of efficiency gain. Nevertheless, there are considerable differences between the cases with axial and radial cavity wall length reduction that provided the same cavity volume. In general the cases with radial cavity wall length reduction performed better with efficiency gain of up to 1.6% higher depending on the case.

It is of interest to notice that changes in cavity size and length scale do affect both the stator exit as well as the rotor exit. Ingress of fluid in the cavity

takes place at the second half of the axial cavity length on the rotor side and egress on stator side. The cavity size heavily impacts the size and the formation of the toroidal vortex that resides inside the cavity. The presence of the vortex although undesirable in the sense that enables flow into a circular motion and no work extraction can take place, acts beneficial as it continuously regulates the in and out flows. The non-presence of the vortex results in a sudden and abrupt movement of the flow that forms radially moving jets at the interaction zone causing greater mixing.

The extension of the upper stator-casing platform through axial cavity wall length reduction enables the flow to continue overturning before it reaches the cavity entrance and gets abruptly re-directed to 90 degrees. A reduction of the axial cavity wall length by 15%-20% leads to the cavity vortex breaking-up into two smaller vertically aligned vortices into the cavity. The lower vortex regulates less mass flow. Mixing is reduced in the interaction zone and efficiency rises up to 0.3%. On the other hand, an extension beyond the 35%-40% of the initial cavity axial length eliminates the zone of influence of the upstream stator in the cavity, leading to the generation of strong in and out of the cavity jets regulated only by the potential flow field of the downstream rotor. Extensive losses through increased mixing occur.

Reducing the radial length of the cavity impacts on the vortex position. The lower the vortex is located, the less the mass flow entering the cavity has to be re-directed from axial to radial direction. Although the leakage mass flow remains unaltered the mass flux oscillations are greatly reduced leading to lower mixing losses. An additional modification tested with the upper right corner of the cavity being rounded led only to efficiency deficits. The mass flow trapped into the counter-rotating vortex of the cavity's former corner is now enabled into the main cavity vortex. Additionally, the rounding re-directed greater mass flow to the cavity vortex introducing thus greater mixing.

Moreover, the use of non-uniform cavity entry geometry and swirl breakers has been tested. A ring attached on the stator side of the cavity was used to modify the inlet geometry enabling thus the circumferential movement relative to the stator. With the use of peaks and troughs along the circumferential cavity entry it has been attempted to hinder the inflow to the cavity and enable the outflow from the latter. Although at stator exit the losses due to mixing were reduced at rotor exit the presence of a stronger tip passage vortex cancel the gain. On the other hand the use of swirl breakers inside the cavity intended to break down the toroidal vortex resulted only in an abrupt

redirection of cavity fluid back into the main flow. Extensive mixing generated losses.

This work presents a coherent and complete study both experimental and computational of various cavity geometrical modifications. The resulting effect on efficiency has been quantified and extensively analyzed. The cavity flows have been well understood and flow models have been presented. Finally design recommendations have been derived.

Kurzfassung

In der vorliegenden Arbeit werden die Ergebnisse einer aerodynamischen Untersuchung verschiedener Designs von Rotoreintrittskavitäten vorgestellt. Die Designs unterscheiden sich in der Geometrie der Eintrittskavität des zweiten Rotors einer zweistufigen Axialturbine niedriger überdeckung mit Deckband, welche charakteristisch für Hochdruckstufen von Dampfturbinen ist. Sowohl die Geometrie als auch das Volumen der Kavität wurden variiert, um eine optimale Längenskala der Eintrittskavität zu ermitteln, die für die Kavitätsströmungen verantwortlich ist. Ziel dabei ist es, eine Minimierung der Vermischung im Gebiet der Wechselwirkung zwischen der Kavität und der Hauptströmung zu erzielen durch Eingriff in die Führung der Leckageströmung.

Kavitätsströmungen sind verantwortlich für die Bildung von Sekundärströmungen und führen daher potenziell zur Entstehung von Verlusten. Turbinen mit Deckband werden in grossem Umfang in der Stromerzeugung eingesetzt, wo Dampfturbinen zum Einsatz kommen. Obwohl sie eine höhere Effizienz durch reduzierte Leckageströmungen bieten, werden Dampfturbinen starken thermischen und mechanischen Beanspruchungen am Schaufelfuss ausgesetzt. Da sie jedoch bei niedrigen Drehzahlen betrieben werden, haben Dampfturbinen mit Deckband definitiv einen Vorteil im Vergleich zu Turbinen ohne Deckband.

Eine experimentelle Untersuchung wurde durchgeführt, um mögliche Nutzen aus den verschiedenen geometrischen Änderungen von Rotoreintrittskavitäten zu quantifizieren, wobei der Fokus im Stufen-Wirkungsgradgewinn lag. Die Experimente wurden an der Niedergeschwindigkeitsaxialturbine des Laboratory for Energy Conversion (LEC) an der ETH Zürich durchgeführt. Sowohl stationäre als auch instationäre Messungen wurden mittels miniaturisierter pneumatischer (4-Loch-Sonde, 5-Loch-Sonde) und hochauflösender schneller Sondentechnologie (FRAP) durchgeführt, um sowohl das stationäre als auch das instationäre Strömungsfeld zu erfassen und zu charakterisieren. Darüber hinaus ist eine zusätzlich numerische Strömungssimulation durchgeführt worden, um eine bessere Visualisierung des stark instationären dreidimensionalen Strömungsfeldes von Turbomaschinen zu bieten.

Die Analyse der Daten zeigt die Auswirkungen der Geometrien der Rotoreintrittskavität auf den Wirkungsgrad deutlich. Das Volumen der Kavität ist modifiziert worden, indem sowohl die axiale als auch die radiale

Wandlänge der Kavität geändert worden ist. Die Veränderungen des Volumens der Kavität sind für eine Reduzierung von 14% und 28% gegenüber dem ursprünglichen Kavitätsvolumen ausgeführt worden. Diese Veränderungen haben sich in Bezug auf den Wirkungsgradgewinn als vorteilhaft erwiesen. Dennoch gibt es erhebliche Unterschiede zwischen den Fällen mit axialer und radialer Reduktion der Kavitätswandlänge, bei konstantem Volumen der Kavität. Im Allgemeinen haben die Fälle mit radialer Reduktion der Kavitätswandlänge besser abgeschnitten, mit einem Wirkungsgradgewinn von bis zu 1.6%, abhängig vom Fall.

Es ist bemerkenswert, dass Veränderungen der Kavitätsgröße und der Längenskala sowohl den Stator- als auch den Rotoraustritt beeinflussen. Der Eintritt von Fluid in die Kavität erfolgt in der zweiten Hälfte der axialen Kavitätslänge, also auf der Rotorsseite, und der Austritt erfolgt auf der Statorseite. Die Kavitätsgröße wirkt sich stark auf die Größe und die Bildung des sich in der Kavität befindlichen Toruswirbels aus. Obwohl durch den Wirbel Strömung in einer kreisförmigen Bewegung hervorgerufen wird und keine Arbeitsentnahme stattfindet, wirkt er sich vorteilhaft aus, da er ständig den Ein- und Austritt von Strömung bestimmt. Das Nicht-Vorhandensein des Wirbels ergibt eine plötzliche und abrupte Bewegung der Strömung, welches radiale Jets zur Folge hat und wodurch eine intensivere Vermischung im Gebiet der Wechselwirkung stattfindet.

Die Verlängerung der oberen Statorplattform durch axiale Reduktion der Kavitätswandlänge ermöglicht dem Fluid solange die Fortsetzung des überumlenkung, bis es den Kavitätseintritt erreicht und plötzlich wieder auf 90 Grad umgelenkt wird. Eine Reduzierung der axialen Kavitätswandlänge von 15% -20% führt zum Zerfall des Kavitätswirbels in zwei kleinere senkrecht ausgerichtete Wirbel in der Kavität. Der untere Wirbel bestimmt weniger Massenstrom. Die Vermischung im Gebiet der Wechselwirkung reduziert sich und der Wirkungsgrad steigt um bis zu 0,3%. Auf der anderen Seite wird das Einflussgebiet des vorgelagerten Stators auf die Kavität beseitigt, sobald eine Verlängerung über die 35% -40% der ursprünglichen axialen Kavitätslänge hinaus verwendet wird. Starkes Ein- und Austreten der Kavitätsjets wird nur durch das Potenzialfeld des nachgelagerten Rotors bestimmt. Erhöhte Durchmischung führt zu höheren Verlusten.

Die Verringerung der radialen Länge der Kavität wirkt sich auf die Position des Wirbels aus. Je niedriger sich der Wirbel befindet, umso weniger Massenstrom, der in die Kavität einströmt, muss von der axialen in die radiale Richtung umgelenkt werden. Obwohl der Leckagemassenstrom unverändert bleibt, verringern sich die Massenstrom-Schwankungen in starkem Masse,

welches zu niedrigeren Mischungsverlusten führt. Eine zusätzliche untersuchte Modifikation mit einer verrundeten oberen rechten Ecke hat nur eine Verschlechterung des Wirkunsgsgrades hervorgerufen. Der Massenstrom, der eingangs an dem gegenläufigen Wirbel der ursprünglichen Kavitätsecke beteiligt war, ist nun im Hauptwirbel der Kavität vorhanden. Zusätzlich hat die Verrundung mehr Massenstrom in den Hauptwirbel der Kavität gerichtet, wodurch eine erhöhte Durchmischung eingeführt wird.

Darüber hinaus ist die Verwendung von sowohl ungleichförmigen Kavitätseintrittsgeometrien als auch Wirbelbarre untersucht worden. Dabei ist für die Veränderung der Eintrittsgeometrie ein Ring an der Statorseite der Kavität verwendet worden, wodurch Bewegung in Umfangsrichtung relativ zum Stator ermöglicht worden ist. Durch die Verwendung von Höhen und Tiefen entlang des Umfangs des Kavitätseintritts ist versucht worden, den Eintritt der Strömung in die Kavität zu verhindern bzw. den Austritt aus der Kavität zu ermöglichen. Obwohl am Statoraustritt die Mischungsverluste verringert worden sind, hat eine Verstärkung des Spitzenpassagenwirbels den Gewinn ausgeglichen. Auf der anderen Seite haben die Wirbelbarre, mit denen der Zerfall des Toruswirbels beabsichtigt worden ist, lediglich zu einer abrupten Umlenkung des Kavitätsfluids zurück in die Hauptströmung geführt. Erhebliche Durchmischung hat Verluste erzeugt.

Die vorliegende Arbeit stellt eine zusammenhängende und vollständige, experimentelle sowie numerische Studie vor, in der verschiedene geometrische Modifikationen der Kavität vorgenommen worden sind. Der resultierende Effekt auf den Wirkungsgrad ist quantifiziert und umfangreich analysiert worden. Die Kavitätsströmungen sind gut verstanden und Strömungsmodelle vorgestellt worden. Abschliessend sind Design-Empfehlungen abgeleitet worden.

Table of contents

1. Introduction

1.1 Introduction

The continuous growth of world's population together with the emerging economies of developing countries such as China and India that enter the market indisputably highlight the need for an increased energy production. Strong long-term growth in the emerging economies drives the fast-paced growth in energy demand. World marketed energy consumption has almost double in the last three decades [1] and will grow by 50% in the next 25 years [76]. New technological achievements that make our life easier are introduced to an increasing number of people worldwide on a daily basis increasing demand of electrical energy. The ACI announced a total number of worldwide flights of 74.1 millions which although faced a slight decrease due to deepening economic uncertainty still represents the mean of transportation chosen by 4.8 billion people in 2009 [2].

Although renewable technologies for use in energy production and transportation are receiving a continuously rising attention, the main energy producers nowadays and for the following decades are turbomachines with the primary source being still the fossil fuels. As fossil fuel prices are the dominant cost factor of such machines the rising fuel prices demand highly efficient turbomachines.

Turbomachines are divided into two main categories based on the energy flow direction. Those that absorb power to increase the fluid pressure (compressors, pumps) and those that produce power by expanding fluid to a lower pressure (steam, gas turbines). Gas turbines are described thermodynamically by the Brayton cycle whereas the Rankine cycle is the one describing the steam turbine thermodynamic cycle, Figure 1.1. Rankine cycle converts heat into work. High pressure fluid enters the boiler where it is heated under constant pressure by external heat source to become dry saturated vapour. Right after the vapour expands through the turbine generating power. Steam turbines plants producing well over 1000 MW of shaft power with an efficiency of 40%, that can go up to 60% in a combined cycle are now being used.

Even though mechanically, turbines are less complex compared to internal combustion engines because of the absence of any reciprocating or rubbing parts, still modern turbines systems may have a vast system of piping, heat exchangers and numerous other equipment. And face critical issues such as blade thermal problems and vibratory response that can impact on the durability and life expectancy of these machines. Moreover, turbines themselves as being state of the art require a sophisticated manufacturing procedure to achieve high efficiencies. Considering the extended use of turbines in power generation even minor efficiency improvement transform to billions of savings in a worldwide scale.

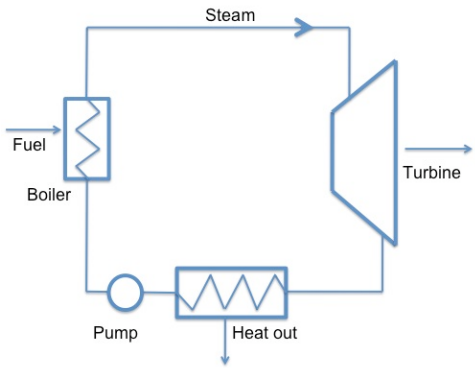

Figure 1.1: Rankine cycle

The turbines are composed of stages, pairs of stationary and rotating blade rows. The stator deflects and accelerates the working medium in the circumferential direction. The following rotor row converts the energy contained in the fluid into angular momentum as the fluid is turned back into axial direction before it enters the next stator row. On the way from inlet to exit of the turbine and during the expansion process the flow experiences a number of aerodynamic loss generating mechanisms that reduced the efficiency of the machine. Passage vortices, cavity flows, tip leakage, horseshoe vortices, blade row interactions drive the flow into a plane normal to the streamwise direction. Undesired secondary flow is created within this highly three-dimensional flowfield and gets transported downstream. Secondary flows are an inherently detrimental effect, which a designer cannot avoid.

1.1.1 Secondary Flows

Secondary flows although undesirable, dominate the flow field in turbines consisting a major source of loss in axial turbines. A lot of work has been dedicated to the description of secondary flows. A detailed review of secondary flows has been given by Sieverding [70] followed later by Langston [40]. They both offered a detailed description of secondary flow vortex structures and their effect on end wall boundary layer characteristics and loss growth through straight turbine blade passages as this was given in the open literature. Sharma and Butler [68] using flow visualization data and detailed measurements of viscous flow development through cascades re-interpreted secondary flow theories formulating a calculation procedure to predict losses caused by endwall secondary flows.

The main type of secondary flow is the induced recirculating flow, which leads to the passage vortex. The source of the induced recirculating flow is the cross flow in the endwall boundary layer that forms as a result of the force equilibrium in curvilinear motion. The momentum equation in the cross-section direction can be written in the form

$$\frac{\rho u^2}{R} = \frac{\partial p}{\partial n} \tag{1.1}$$

With a decrease of the velocity in the boundary layer, a reduction of the streamline curvature radius in the boundary layer flow is required in order to balance the pitchwise pressure gradient formed in the channel. As a consequence, the boundary layer flow is turned more than the main flow in the blade-to-blade channel, leading to a crossflow from the pressure to suction surface in the endwall boundary layer. A compensating return flow must then occur at a certain distance from the endwall, giving rise to the circulating flow described by Hawthorne [26], Figure 1.2. From this circulation flow, a passage vortex is formed.

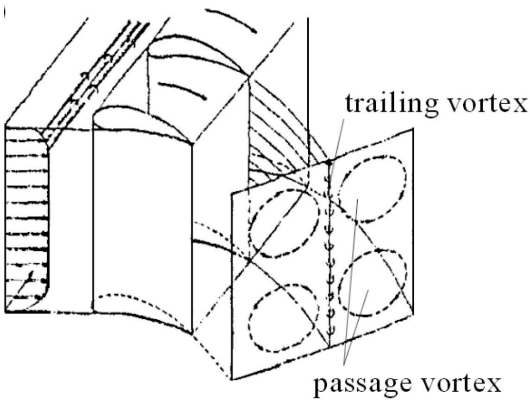

Figure 1.2: Secondary flow model in turbine cascade by Hawthorne [26]

Another element of the secondary flows is the horseshoe vortex. The process of formation of the horseshoe vortex at the leading edge of the blade and its downstream transport was explained among others by Langston [39]. As the boundary layer is decelerated by the adverse pressure gradient it separates at a saddle point in front of the blade's leading edge. The boundary layers formed on the endwall and on the blade surfaces give rise to the horseshoe vortex with its two legs; the pressure side leg and the suction side leg of the horseshoe vortex. The suction side leg stays attached to the suction side surface of the blade whereas the pressure side leg under the pressure gradient moves from the pressure side of the blade to the suction side of the neighbouring blade resulting in the passage vortex. Hawthorne [27] was among the first to describe the secondary circulation that manifest itself as the passage vortex followed by Langston et al. [38], Goldstein and Spores [21], Wang et al. [80] and Gregory-Smith et al. [24]. The smaller in size and counter-rotating suction side leg of the horseshoe vortex wraps around the passage vortex. The significant difference in size between the two vortices may lead to the entire dissipation of the secondary kinetic energy of the suction side leg due to shear interaction with the stronger passage vortex.

The corner vortex described by Sieverding [70] as the counter-rotating vortex (compared to the passage vortex) located in the endwall suction side corner. It is a shear driven secondary flow structure formed as a result of the passage vortex impingement on the suction side. The corner vortex requires large turning angles and is rarely observed experimentally.

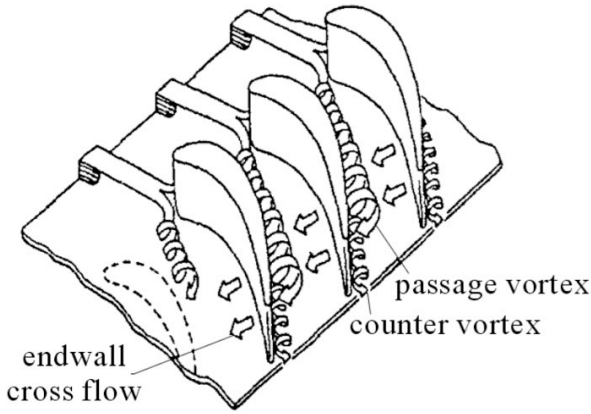

Figure 1.3: Secondary flow model in turbine cascade by Langston [39]

Many of the studies presented refer to experiments performed in cascades. It should be noted that the main differences between rotating machines and cascades are the annular shape, which introduces a radial pressure gradient, and the skewing of the inlet boundary layer caused by the relative movement of the stationary and rotating rows. Additionally the real machines require blade cooling, which protects the material, but introduces secondary flows.

1.1.2 Unsteady Flow Interaction

Flow in turbines is highly unsteady due to the relative motion of stationary and rotating blade rows. Flow distortions generated by the upstream bladerows and the potential flow field of the downstream rows significantly affect the turbine's stage efficiency. Important issues as blade loading, mechanical fatigue due to blade fluttering, heat transfer, thermal fatigue and noise generation have their origin in the unsteadiness of the flow field. Potential flow interactions, wake-blade interactions and vortex interactions are mechanisms that generate unsteadiness. Unsteadiness has two parts; a random part related with turbulence and the periodic part owed to the blade

passing frequency. The degree of unsteadiness is evaluated though the reduced frequency parameter defined as

$$\bar{f} = \frac{Convection\ Time}{Disturbance\ Time} \tag{1.2}$$

The convection time is defined as the time needed to go through the blade passage and the disturbance time is the time needed for one rotor blade to sweep one stator passage. The magnitude of reduced frequency is a measure of the balance between the unsteady and quasi-steady effects. If $\bar{f} = 1$, unsteady and quasi steady effects co-exist whereas, if $\bar{f} >> 1$ unsteady effects are of greater importance. In the test cases examined in this study $\bar{f} = 2.64$.

1.1.3 Potential Flow Interaction

Blades exposed to internal flow, build around them a potential flow field. The relative motion between stationary and rotating blade rows causes an interaction of these potential flow fields which in contrast to the convective mechanisms they are also transported upstream. As a result of this interaction an unsteady time-varying, rotor driven pressure field is generated. Parker and Watson [49] discussed the mechanisms of interactions between the blade rows studying the noise and vibration excitation because of these interactions and stated that the potential effect experiences an exponential decay with distance.

1.1.4 Wake-Blade Interaction

Every bladerow is subjected to periodic unsteadiness caused by the proximity and relative motion of adjacent bladerows. There are two primary forms of periodic unsteadiness. These are the wakes from the bladerows upstream and the potential fields of the bladerows both upstream and downstream. At the trailing edge of the blade the boundary layers of the pressure and suction sides merge and form the so-called wake. It is an area with low momentum fluid. Meyer [48] argued that each wake could be thought of as a ‘negative’ jet flowing toward the origin of the wake superimposed on a uniform freestream. The unsteady velocity vectors of Figure 1.4 reveal the existence of negative jets that are present throughout the wake progression within the blades. Smith [71] noted that as a result of the blade circulation, the wake segments experience bowing, reorientation,

elongation and stretching as they progress through the blade passage. The higher velocities in the mid-passage compared to in front of the leading edge initiate the bowing of the wake. Once in the passage the wake is stretched as it accelerates over the suction surface increasing its width re-orientation and elongation occur constantly due to cross passage differences in velocities, Hodson and Howell [30]. The behavior of the wakes can be important in relation with the laminar-turbulent transition of the boundary layer on the suction side affecting the blade row performance.

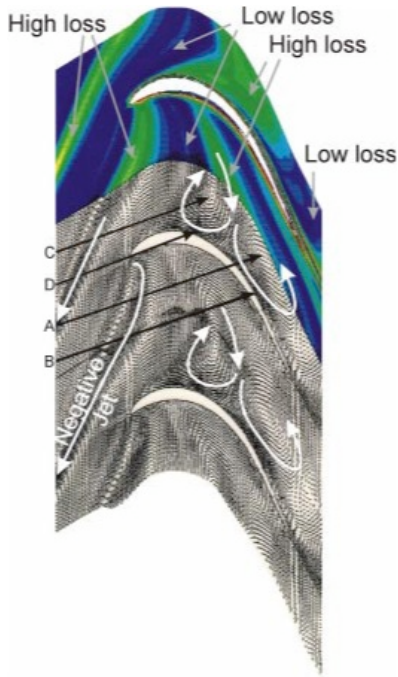

Figure 1.4: Predicted contours of entropy and unsteady velocity vectors by Hodson and Howell [30]

1.1.5 Vortex Interaction

The interaction of vortices shed from the upstream blades with the downstream bladerow is also not negligible. Especially in low aspect ratio machines vortices occupy a considerably large portion of the span. In low

solidity turbines as the one considered the shedding of larger vortices is more pronounced as fewer blades are used to produce the same work through higher turning angles. Unlike wakes, vortices are not chopped by the downstream bladerow but they are convected through the blade passages after having been around the blade. Chaluvadi et al. [12] using smoke traces, identified the upstream suction side leg of the stator passage vortex being positioned on top of the newly formed rotor passage vortex whereas the pressure side leg had merged with the rotor passage vortex. Further work on the vortex interaction with the downstream blade rows has been performed by Binder et al. [9] who had stated that the vortices break down and kinetic energy transforms to turbulence, Sharma et al. [69] and Behr [8].

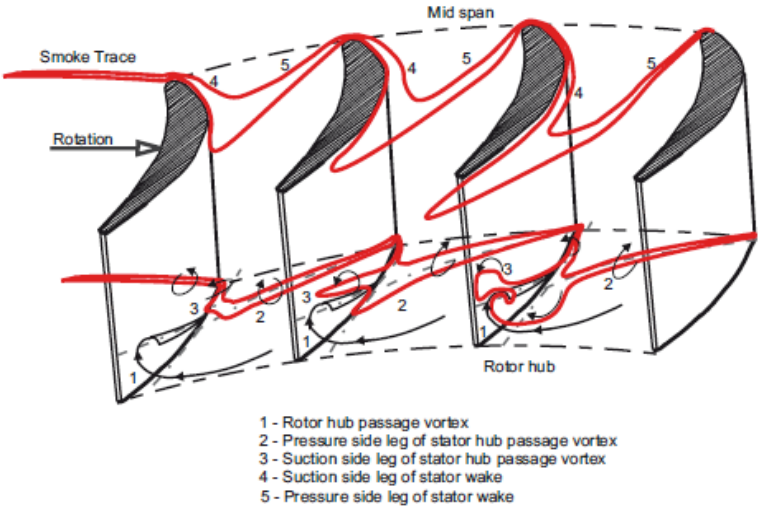

Figure 1.5: Vortex blade interaction [12]

1.1.6 Low Solidity Blades

Low solidity bladerows offer a direct reduction in the manufacturing cost, the time needed and the weight of the machine through a direct reduction in the blade count. On the other hand, they are prompt to increased secondary flows production leading potentially to loss generation. Fewer blades to produce the same work directly translates to higher turning angles and thus larger wakes and vortices are being shed. Nevertheless, Tashima et al. [74]

showed that the same level of efficiency can be maintained when comparing two cases; one with high solidity and a second one with low solidity. The reduced count of the secondary features compensates their larger size. Song et al. [73] compared three different low solidity turbine cascades and verified the potential to maintain high levels of efficiency with reduced parts count. Extensive work has also been done in the area of high lift turbine blading for LP gas turbines, Solomon [72] and Howell et al. [31]

Figure 1.6: High and low solidity stator blades with a ratio of 3:4

1.1.7 Shrouded vs. Unshrouded Configuration

In any kind of turbomachinery a certain gap is inevitably required between the rotating and stationary components achieved by a number of different design approaches primarily focused on the reduction of leakage flows over the blade. Leakage flow is considered to be a main source of aerodynamic loss. It comprises 1/3 of the total aerodynamic losses of a turbine stage. The minimization of the gap is more than desirable but mechanical considerations and mainly thermal expansion of the materials set certain limits. Normally, this distance is of the order of 1% of the blade span. Shrouded blades perform better on the issue of sealing. Nevertheless, they require a complicated cooling arrangement that finally will create an efficiency penalty and significantly increases the manufacturing cost per blade. Moreover, the added weight on the outer diameter of the machine considerably increases the centrifugal forces acting on the blade, reducing life expectancy. Therefore, shrouded turbines are used in power generation where

the machine runs at lower rpm and the temperature is by far lower than that of a gas turbine used in a jet engine.

a. b.

Figure 1.7: (a) Shrouded turbine blade and (b) unshrouded turbine blade

1.1.8 Labyrinth Seals

Labyrinth seals have been under study for years and the research is still ongoing. A shrouded design approach requires the presence of a labyrinth seal to allow the relative movement between rotating and stationary parts. Labyrinth seals reduce the amount of leakage flow that by-pass the main flow path through the rotor, increasing thus efficiency. Numerous labyrinth geometries are used by the turbine designers depending on the application but all of them consist of an inlet and exit cavity and a number of closed cavities in between. The size of the cavities needs to be relatively large compared to the blade height to allow for the axial displacement of the rotor due to thermal growth or axial thrust variations. Examples of various labyrinth geometries are given in Figure 1.3. Labyrinth seals offer a reduced leakage mass flow compared to the tip leakage that escapes over unshrouded blades.

Nevertheless, as the leakage mass flow does not produce any work on the rotor major efforts have been undertaken to quantify this mass flow as a first step and reduce it through an improved seal design as a second step. Egli [15]

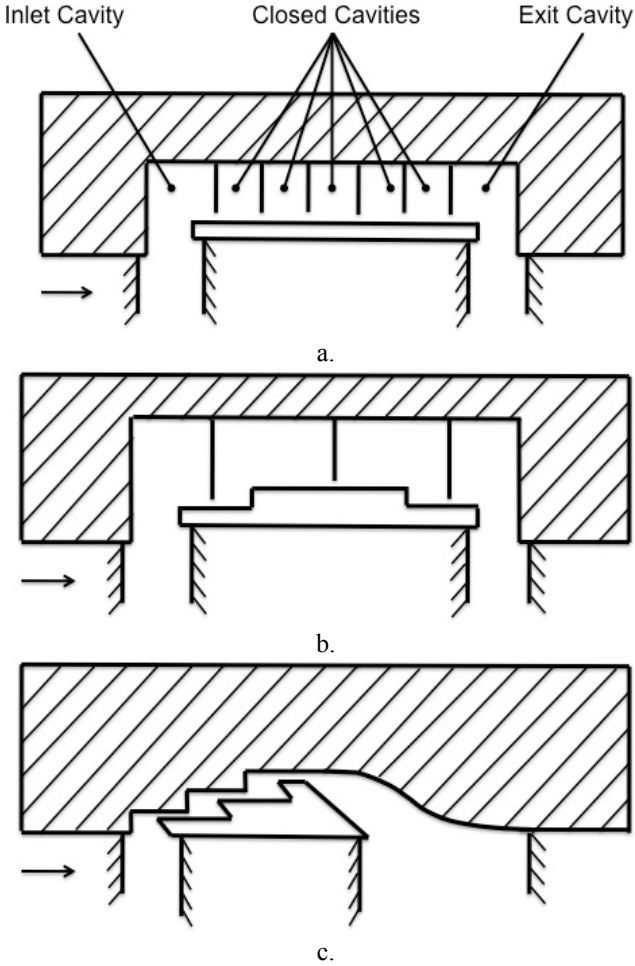

Figure 1.8: Examples of labyrinth seal configurations; look through (a), stepped labyrinth (b), and gas turbine (c)

and Traupel [75] presented respectively theoretical and an experimental approaches in their attempts to quantify mass leakage flow through labyrinth seals. Egli [15] assumed a perfect dissipation of the kinetic energy into heat within the cavity as well as zero initial velocity upstream of the gap. For his empirical correlation, Traupel [75] uses a discharge coefficient based on labyrinth geometry. Mixing of the leakage flow within the inlet cavity recirculation in the interaction with the main flow zone and reinjection at the exit cavity causing negative incidence on the following blade row are processes resulting in efficiency penalties.

1.1.9 Heat Transfer and Shrouded Blades

Heat transfer prediction has long been a research topic. The coupling of heat transfer prediction with blade aerodynamics is where the problem rises. A heat transfer prediction requires a proper knowledge of the surface pressure distribution. Although heat transfer prediction with the use of computational tools has nowadays a better accuracy it is still away of being accurate. While the aerodynamic performance can be evaluated within an accuracy of 1%, heat transfer prediction lies between ± 10%.

As already mentioned the shrouded turbine blades although they generally offer higher efficiency, the shroud itself need to be cooled, cancelling partially thus the initial gain. The conventional shroud cooling strategies, such as film cooling and internal convection cooling [17], result in heavier shrouds, Figure 1.9b. This restricts the rotational speed and hence the stage work output. Maintaining an adequate lifetime and reliability requires improved cooling methodologies. Numerous studies on the topic of heat transfer have been performed. Kanjirakkad et al. [35] and Janke et al. [34] have investigated passive shroud cooling concepts to avoid thick shrouds with active internal and film cooling, Figure 1.9a. A coolant injection at the rotor inlet cavity from a stationary point cools more effectively the shroud faces. Lehmann et al. [43] applied also passive cooling technique and revealed regions of high heat transfer on the suction side of the shroud, Figure 1.7.

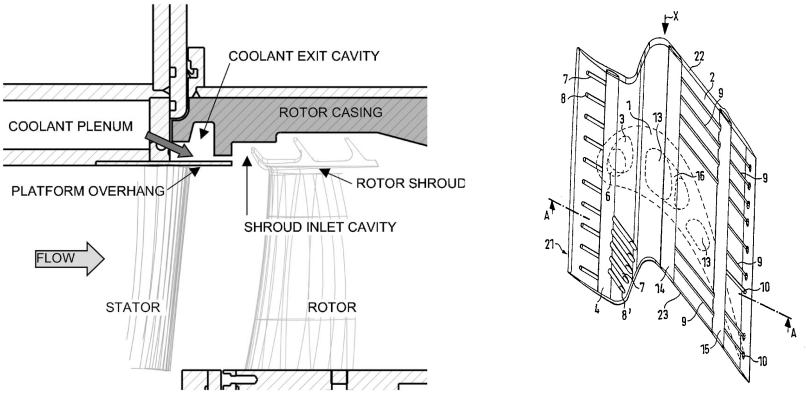

a. b.

Figure 1.9: (a) passive cooling by Kanjirakkad et al. [35] and (b) internal cooling by Evans et al. [17]

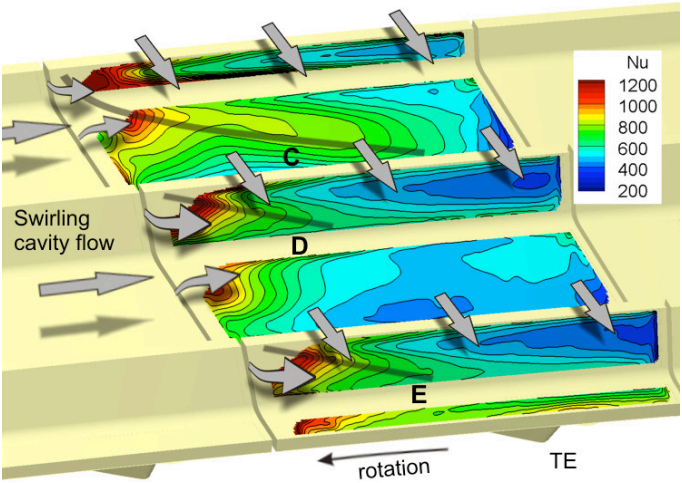

Figure 1.10: Measured heat transfer distribution on the top surfaces of the shroud Lehmann et al. [43]

1.1.10 Leakage Flows in Shrouded Turbines

Efficiency losses attributed to leakage flows in shrouded blades account for a substantial part of the total aerodynamic losses in turbomachinery especially in highly loaded turbines with low aspect ratio blades. Potential work that could have been extracted from the rotor blades not only bypasses the main flow but also causes extensive losses because of mixing in the interaction zone but also in the tip region of the blades due to changes in the incidence angle.

Wellborn and Okiishi [81] reported a 1% efficiency reduction for every 1% increase in the clearance to span ratio. Loss generation in the tip section of the shrouded blades is primarily associated with the mixing process that takes place in the interaction zone between the cavity flow and the main stream. In his review on secondary flows in axial turbines, Langston [40] gave an overview of the work that has been done on secondary flows up to 2001, highlighting the necessity for a better understanding of the associated mechanisms. Earlier, Denton [14] in his work on loss mechanisms in turbomachines more specifically identifies the mixing process during re-entry of the leakage flow as the main entropy creating process causing losses with shrouded blades. Rosic et al. [61] numerically studied the significant influence on the aerodynamics of shroud and inner cavity geometry on turbine performance. He reported the beneficial reduction of cavity length and the insignificant effect of shroud thickness on efficiency. Anker et al. [5] focused on physical effects and losses of leakage and main flow in the rotor and in particular those introduced by the interaction of the main and cavity flows with respect to loss generating mechanisms. He showed the weakening of the upper passage vortex due to the egress of the leakage flow, while the upper secondary passage vortex of the subsequent stator strengthens as the leakage flow is re-injected after the rotor. Hunter and Manwaring [32], and Li et al. [44] talked about leakage flows influencing the downstream flow field even after two blade rows. Research has also been undertaken on the fins of the labyrinth themselves. Vakili et al. [77] studied seal design to examine their influence on leakage characteristics. Having done PIV measurements and computational work, they reported the significance of the fin axial location and angle and the step height on leakage reduction. Flow visualization was also used by Rhode et al. [58], [59] to measure leakage resistance in their water test facility with regard to step shape and height. The interaction of

cavity and main flow has also been studied by Peters et al. [52]. They performed steady state measurements together with simulations to report a strongly affected flow field at the subsequent stator at the tip region. Schlienger et al. [66] studied the use of inserts at the exit cavity in an attempt to improve re-entry of the leakage flow, but surprisingly his efficiency results were negative. In another approach, Wallis et al. [79] state that modern sealing arrangements have considerably reduced the leakage fractions to a degree that further improvements can only be achieved by controlling the leakage flow itself, especially the way it re-enters the main flow. By the use of bladelets positioned at the exit cavity onto the shroud they tried to redirect the leakage jet and align it with the main stream. They reported efficiency deficits through poor performance of the bladelets with the main flow now travelling further upwards into the cavity. Rosic and Denton [61] on the other hand manage to better control the tangential velocity by positioning the bladelets at the stationary wall of the exit cavity, shown on Figure 1.11 increasing the efficiency by 0.4%. Pfau et al. [54], [55] systematically investigated cavity flows by analyzing a set of experimental data. They described in detail the dominating kinematic flow feature in the region, the toroidal vortex: a vortex fed with high pressure fluid from the pressure side of the stator blade. The associated fluctuating mass in turn results in negative incidence on the rotor. After having discussed and quantified the secondary flow development and mixing losses they derived design recommendations.

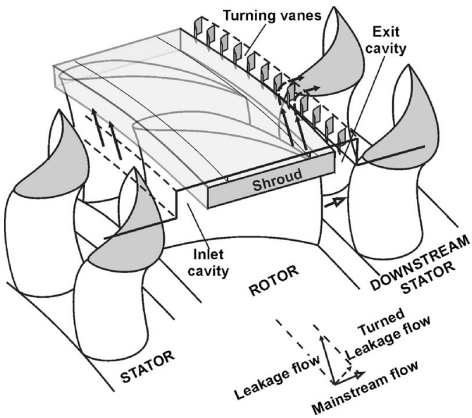

Figure 1.11: Schematic of the turning vanes at the exit rotor cavity adopted by Rosic and Denton [60] to guide the leakage flow back into the main flow

Pfau et al. [55] identified the inflow area and quantified the mass flow that enters the cavity (Figure 1.12). They aimed at the understanding of the secondary flow at the tip region so as to prevent the inflow to the cavity through re-designing the labyrinth seals.

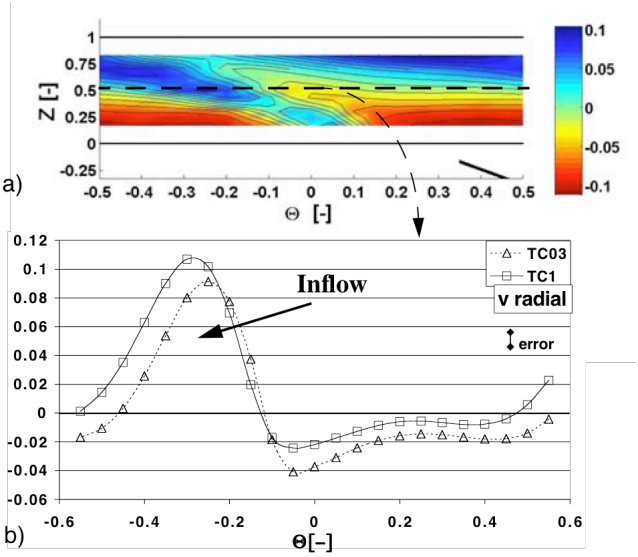

Figure 1.12: Radial velocity component at the interface between cavity and main flow [54]

They proposed nonaxissymetric shaping of the labyrinth interaction flow path to better control the toroidal vortex residing in the rotor inlet cavity along with the leakage jets that flush the cavity in and out. They proposed the pressure side of the rotor passage to be positioned at a higher radius than on the suction side. Therefore, the streamlines of a lower curvature would enter on the pressure side and less fluid will be pushed inside the cavity. On the suction side the cavity fluid would have to reach a lower radii in order to be sucked into the rotor passage. In terms of streamline curvature more fluid would be pushed into the cavity at the suction side than on the pressure side.

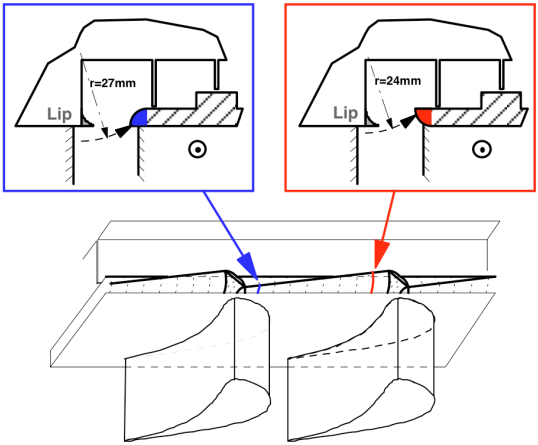

Figure 1.13: Shroud leading edge design for reduced rotor passage to cavity flow interaction [55]

1.1.11 Integrated Design of Rotor Leading Edge and Cavity Flows

Losses owed to changes in incidence angle at the tip section of the blade due to prior mixing of the cavity and main flows account for a substantial part of the total aerodynamic losses in shrouded turbines. Part of the leakage flow that is driven by the pressure difference across the rotor through the labyrinth, after having been circulated inside the rotor inlet cavity by the toroidal vortex re-enters the main flow causing extensive mixing in the interaction zone [14]. The difference in flow angle between the re-injected cavity flow and the main flow is what facilitates the off-design incidence on the downstream bladerow. Wallis et al. [79] and Rosic and Denton [60] attempted to guide the cavity flow back into the main flow with the use of bladelets positioned on the shroud and on the stationary cavity wall respectively. Only Rosic and Denton [60] manage to successfully lead the cavity flow with a corrected flow angle back into the main flow reporting an efficiency increase of 0.4%. Using a similar approach, Mahle [46] reported marginal efficiency gains in a computational study. Peters et al. [52], Anker et al. [5] and Gier et al. [20] reported on the strong interactions between cavity and main flow and examined the different loss-generating mechanics. They discussed the secondary channel vortex and its strengthening due to the egress of the cavity

flow. On the same topic, Pau et al. [50] studied the impact of the leakage flow on the main flow. They showed that there is an enhancement of all counter-rotating vortices with respect to the main passage vortex due to the low turning that is experienced by the leakage flow. The strong negatively signed vorticity that dominates the secondary flows at the interaction zone has also been reported by Adami et al. [3]. Gregory-Smith et al. [25] succefully introduced the use of endwall profiling procedures to modify the secondary flow. Sauer et al. [62] proposed the use of leading edge modifications at the tip region to decrease secondary losses. Brenner et al. [10], Becz et al. [7] and Perdichizzi and Dossena [51] studied the influence of the leading edge geometry on secondary and endwall losses respectively. These studies have shown effectiveness in controlling secondary flow under controlled inflow conditions. Nevertheless, the inflow conditions are highly unsteady and three-dimensional [76, 71]. Blade row interactions [30, 13] wake-blade and vortex blade interactions [31, 66] as well as the presence of open cavities [55] they all contribute to the unsteadiness of the flowfield. A lot of work has been dedicated to the mixing occurring at the interaction between the cavity and main flows at the rotor exit cavity and its consequence on the downstream bladerow. On the other hand, the interaction between the two flows at the rotor inlet cavity that leads to an off-design incidence on the tip section of the rotor blade has not receive much attention.

Research Objectives

Nowadays in view of the declining energy resources and the consequential fuel price increase, highly efficient turbines have become a necessity. Improving the turbine performance and at the same time reducing the cost due to fuel consumption is not at all an easy task. Nevertheless through advanced planning, imaginative research, persistent development and painstaking evaluation, a whole new turbine generation has been created in the last years. There is a wide selection of designs of the various components to meet the specific requirements of pressure and temperature conditions of every application. In the overwhelming majority of these cases industrial and cogeneration systems are designed to provide the operating flexibility to economically utilize steam. The aerodynamic performance of the turbine is of central importance. Bearing in mind that cavity related losses represent a large portion of the total aerodynamic losses, the study of the cavity flows is of great interest.

The objective of this work is to investigate the impact on efficiency of various inlet rotor cavity geometrical modifications and provide the turbine designers useful guidelines for cavity design. Both the geometry as well as the cavity volume have been modified. Qualitative and quantitative results elaborated the mixing processes in the interaction zone between cavity and main flow. Data analysis of both steady and unsteady measurements performed inside the cavity, at rotor inlet and at rotor exit provided information on the effect of downstream rotor flow field changes with respect to cavity geometry and length scale. A flow model has been derived for all the cases examined and an optimum cavity design has been proposed.

Thesis Outline

Chapter 1

A literature review with the following topics being addressed is given: Secondary flows, unsteady flow interaction, low solidity blades, shrouded vs. unshrouded configuration, labyrinth seals and leakage flows in shrouded turbines.

Chapter 2

In this chapter the test rig will be described along with the measuring techniques. The various probes used in the campaign will be introduced and their uncertainty in measurement will be analyzed. The computational tool used for the qualitative analysis will be presented.

Chapter 3

The total-to-static efficiency is presented for all cases considered in this study. Furthermore the inlet flow field conditions to the second stage are presented and discussed.

Chapter 4

In this chapter the effect of the cavity volume on efficiency will be discussed. Five cases will be examined divided into two groups. Cavity volume reduction is achieved through extension of the upper stator-casing platform reducing thus the available inlet cavity area and through the radial cavity wall reduction. Cavity volume is reduced by 14% and 28% for both cases of axial and radial wall length reduction compared with the baseline case. Each of the two cases is compared to the baseline case. Additionally, the use of swirl brakers is discussed.

Chapter 5

In this chapter the effect of geometry on stage efficiency is studied. Cavity volume is kept constant between the cases examined so as to exclude any influence on the efficiency. The effect of the cavity length scale is studied. The dynamics of the toroidal cavity vortex are studied and its influence on the leakage mass flow and on the re-entry path. Also the effect of

a curvature introduced in one of the cavity's corner is examined. Cavity volume is maintained constant between the cases. The impact on the toroidal vortex, leakage mass flow and the re-entry path is presented. The use of non-uniform inlet cavity design to control the cavity flow is studied. In the second part of this chapter the available inlet cavity area is blocked by 80%, maintaining only a minimum operating safety distance from the rotor shroud to examine the influence on cavity flows and leakage.

Chapter 6

In this chapter the coupling between the rotor leading edge and cavity flows shall be addressed. The geometry of the rotor leading edge will be modified and the impact on efficiency will be discussed. A sensitivity analysis is also performed on the impact of tip clearance gap on cavity flows

Chapter 7

In the last chapter the main conclusions drawn out of this work will be presented along with the proposal for future work.

2. Research Facility And Methods

2.1 Experimental Facility

2.1.1 Overview

The test facility used for the experimental part of this work is the axial research turbine facility named 'LISA' of the Laboratory for Energy Conversion of the ETH Zurich. The facility can accommodate either a 1½ stage or a maximum of 2 stages of an axial turbine. It is a closed loop, 3 stores high facility opened to the atmosphere at the exit of the turbine. The air is delivered by the 750 kW radial compressor with a maximum pressure ratio of 1.5 and a maximum massflow of 13 kg/s. Adjustable inlet guide vanes can achieve the exact operating point of the compressor. After the exit of the compressor the air goes through the two successive water to air heat exchangers to regulate the inlet turbine temperature to a constant value of 37.8^{o}C. Before entering the turbine test section the air passes through a filter, a 90° bend and a vertical straight duct 4m long containing a honeycomb and a flow straightener to generate a homogeneous flow. The fluid expands in the axial vertically positioned turbine. The mechanical power generated by the turbine is transmitted through a twin-shaft arrangement and two torquemeters that individually measure the torque of the two shafts, to the DC generator. The axially positioned DC generator of 400 kW maximum power and 2200 RPM maximum rotational speed absorbs the turbine power regulating the turbine rotational speed. The accuracy achieved in controlling the RPM is of ± 0.1 RPM/3000 RPM. An electrical power converter feeds back the current into the grid. Between the turbine and the generator a 90° spiral toothed gearbox halves the rotational speed. A ventouri nozzle situated before the compressor accurately measures the mass flow. A summary of the main parameters of the operating range of the test facility are presented in Table. 2.1.1-1

Compressor power	750kW	Turbine speed (max.)	3000rpm
Compressor massflow	6 – 14 kg/s	Turbine torque (max.)	1500 Nm
Compressor pressure ratio	1.1 – 1.5	Turbine inlet temperature	35 – 55 ^{o}C
Generator power	400 kW	Turbine exit pressure	Atmospheric
Working fluid	Air	Turbine tip diameter	800 mm

Table 2.1 Main working parameters of the test facility LISA

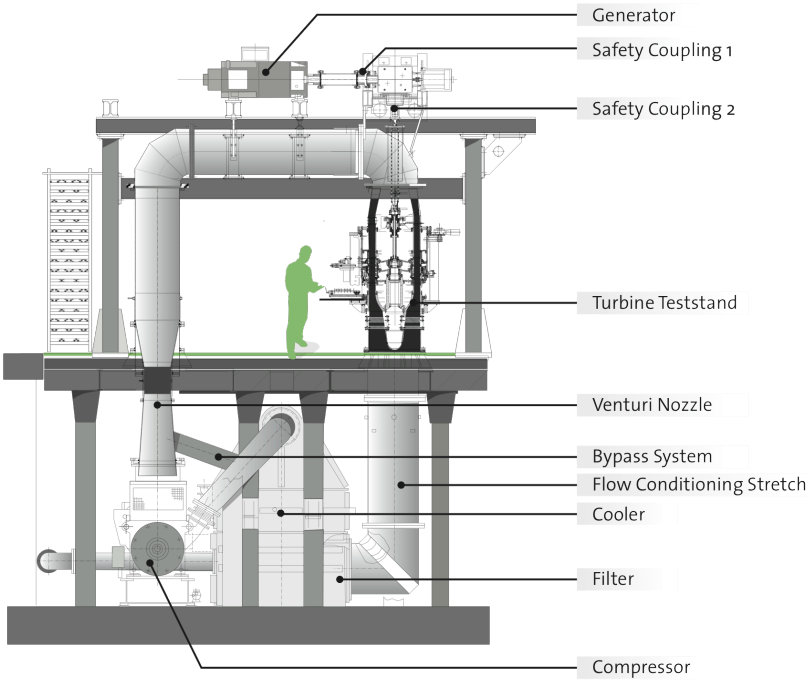

Figure 2.1: Schematic view of the LISA research turbine test facility

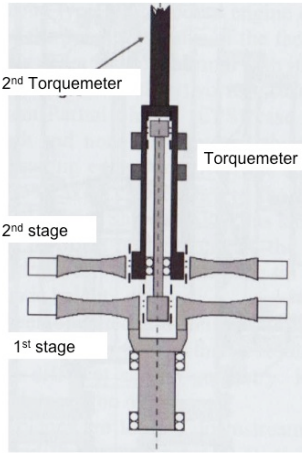

Figure 2.2: Schematic of the twin spool turbine design and torquemeters arrangement, [57]

The facility is equipped with several transducers that are used to monitor and control the turbine flow conditions as well as the bearings temperature and mechanical vibrations a set of accelerometers and proximity sensors are connected with a diagnostic system. An emergency shut down system is activated based on the vibration values measured. Additionally the gearbox can be decoupled on both sides from the turbine and the generator through clutches in case of an over-torque incident. Turbine pressure drop, RPM, independent torque measurement of the first and second rotor, mass flow rate and in and out temperatures are continuously monitored.

2.1.2 2-Stage Turbine

In the current work the turbine consisted of two stages. Both rotors have 48 blades as well as the first stator with a solidity of 1.43. The second stator has a solidity of 1.25; that means 36 blades. The ratio between the stator blade counts is 3:4. In Table 2.2 the specifications of both stators is presented. Both stators are designed to have the same exit flow angle. The axial chord remains the same between the cases. The schematic of the blade profile is shown in Figure 2.3.

Parameter	HS stator	LS stator
Blade count Zs	48	36
Axial chord* C_z [mm]	50	50
Chord length* C [mm]	66.3	77.4
Pitch* t [mm]	46.5	62.0
Blade span H [mm]	90	90
Aspect ratio AR = H/C [-]	1.36	1.16
Solidity σ = C/t [-]	1.43	1.25

Table 2.2: Geometric details of stator blades.
(* indicates that dimension is at 50% span)

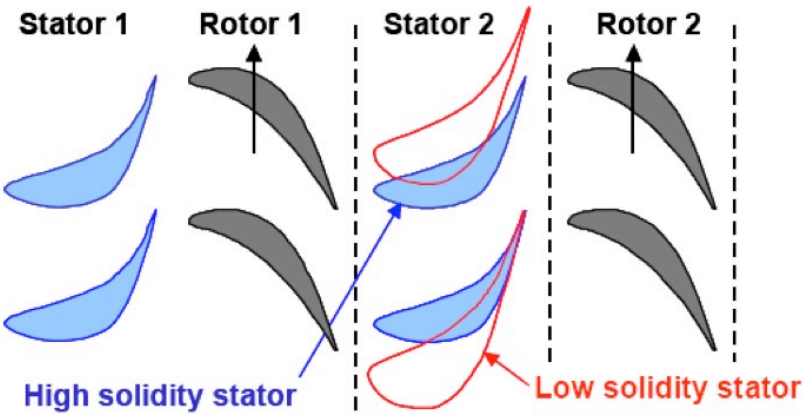

Figure 2.3: Schematic of blades profile

The blade profile under investigation is representative of a typical high-pressure section of a steam turbine for power generation plant. In Table 2.3 the main parameters of this test case configurations are shown. The baseline test case was initially measured in by Tashima et al. [74]

Rotor speed [RPM]	2750
Overall pressure ratio [-]	1.32
Mass flow [kg/sec]	7.87
Turbine inlet temperature [^{o}C]	37.8
Blade number count stage-1 (stator/rotor)	48/48
Blade number count stage-2 (stator/rotor)	36/48
Tip/hub diameter [mm]	800/620
Flow coefficient (stage-2) [-]	0.3
Loading coefficient (stage-2) [-]	1.0
Mach number (stator/rotor)	0.32/0.1
Reynolds number (rotor)	2×10^5

Table 2.3: Main parameters of the test case configuration based on the characteristics of the LS stator

The rotors are shrouded. The labyrinth consists of an open inlet and exit cavity and three intermediates. The gap size, the radial distance between the shroud and the fins is 0.44% of the blade span size. A schematic of the turbine is presented in Figure 2.4.

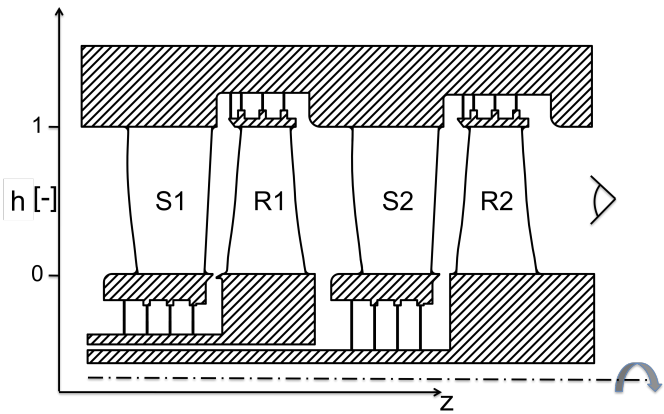

Figure 2.4: Schematic diagram of the two-stage axial shrouded turbine 'LISA'

2.1.3 Inlet Cavity Configurations

The baseline cavity is shown in Figure 2.5. The dimensions are $0.24C_z$ and $0.36C_z$, respectively, in the axial and radial directions, which provides a minimum operating safety distance of $0.16C_z$ between the rotor shroud and stator casing.

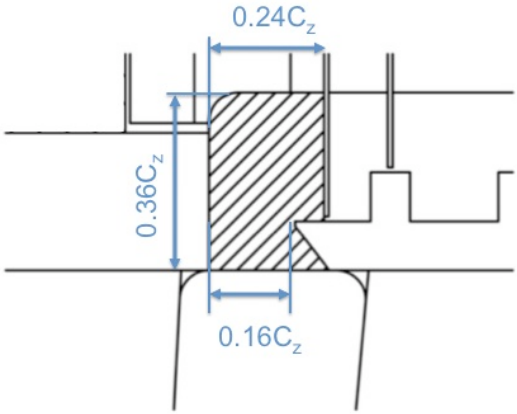

Figure 2.5: Illustration of the inlet cavity

The additional to the baseline test cases examined in this work are shown in Figure 2.6. The cavity sizes under investigation are 14% and 28% smaller relative to the baseline case. The volume reduction is accomplished either by an extension of the upper stator casing platform (Figures 2.6a, 2.6b) or by a reduction of the cavity's radial wall, Figures 2.6c, 2.6d. The upper stator casing was extended by 17% and 34% of the initial axial cavity length. For the cases with the radial wall length reduction the wall length was shortened by 13% and 25% of the initial radial length.

In every group the cavity volume is kept constant so as to exclude any influence of the cavity volume on the mass flow that escapes through the labyrinth over the rotor. In the two cases where the upper stator casing platform was extended, the cavity's axial length was reduced by 17% and 34% respectively, shown in Figures 2.6a and 2.6d. The radial wall length was reduced by 14% and 25%, Figures 2.6b, 2.6c, 2.6e and 2.6f to achieve the cavity volume reduction of 14% and 28% respectively. The lowering of the

upper axial cavity wall intended to the creation of a more circular cavity vortex by eliminating the area where fluid was originally drifting between the cavity vortex and the wall. The design intension of the additional curvature of the cases presented in Figure 2.6c and 2.6f is to eliminate the counter-rotating vortex that resides in the corner formed between the downstream radial cavity wall and the upper axial wall. All cases originated from the baseline case with the use of extensions. The extensions are depicted in red in Figure 2.6.

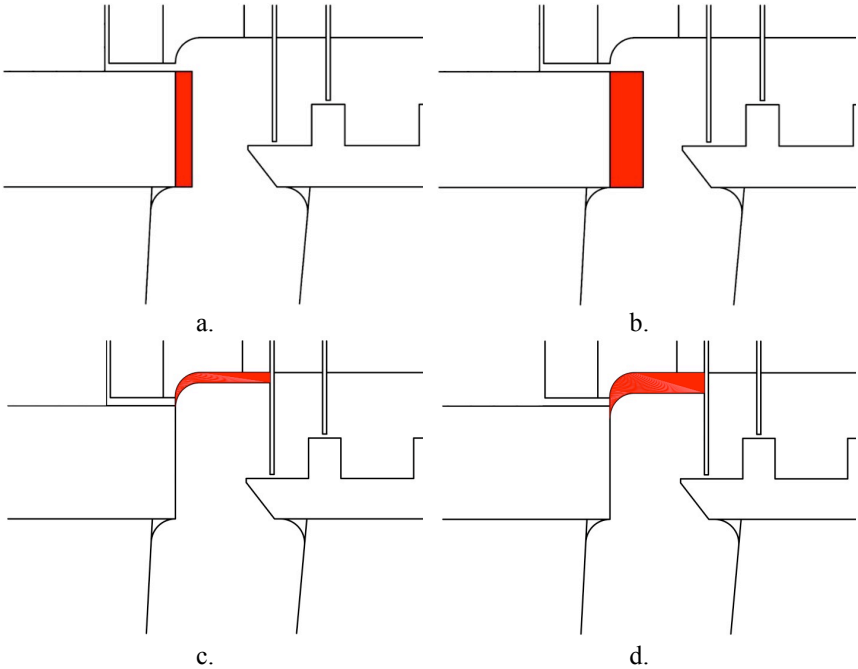

Figure 2.6: Inlet cavity configurations. Cavity volume reduction 14% for (a) 14.0 and (c) 14.1, and cavity volume reduction of 28% for (b) 28.0 and (d) 28.1. Extension of the upper casing stator platform by a. 17% and b. 34% of the cavity's axial length and shortening of the radial wall length by 13% for (c) and 25% for (d).

In the next two cases the radial cavity wall was shortened as well. In these cases an additional rounding in the upper downstream cavity corner was introduced. The design intention of the curvature was to eliminate the counter-rotating vortex present in the corner reducing thus mixing.

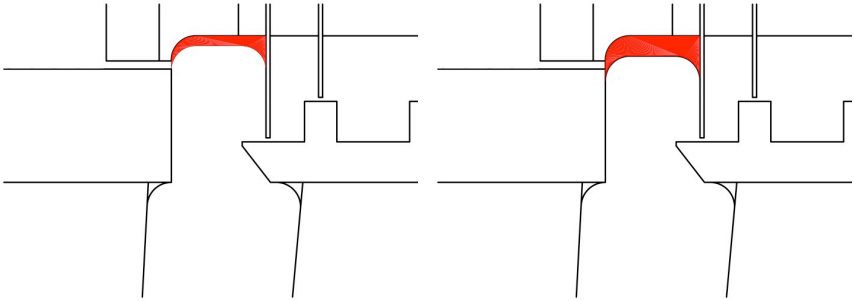

a. b.

Figure 2.7: Inlet cavity configurations. Cavity volume reduction 14% for (a) 14.2 and 28% for (b) 28.2. Additional rounding introduced in the upper downstream cavity corner.

The next case reduced the cavity volume by introducing a non-uniform, wavy design of the upstream radial wall. The axial profile varied from a minimum stator casing extension of 17% to a maximum of 34% of the initial axial cavity length. The design included 36 peaks and troughs, the same as the number of stator blades and could be circumferentially clocked with respect to the stator trailing edge. In Figure 2.8a the non uniform ring is installed at the exit of the second stator, clocked at 25% circumferential clocking position. The circumferential clocking positions mentioned throughout the text are shown in Figure 2.8b. They are expressed as a percentage of the stator pitch at span 1.0 away from the stator trailing edge. The design intention of the non uniform cavity inlet area was to halter the high pressure fluid originating from the stator pressure side from entering the cavity through the extension of the casing (peak) but also to reduce mixing in the interaction zone through improvement of the re-entry path (trough), [54-55]. Two different designs, design A and B were tested being different in the extended area maintaining though the cavity volume reduction to the level of 14% compared to the baseline case, Figure 2.8c.

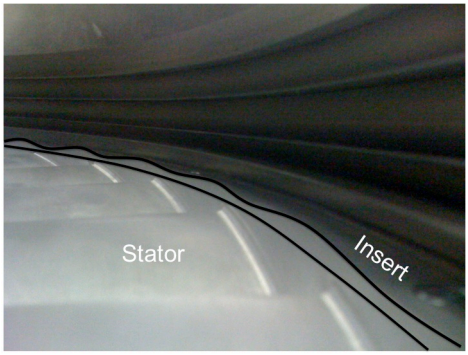

a.

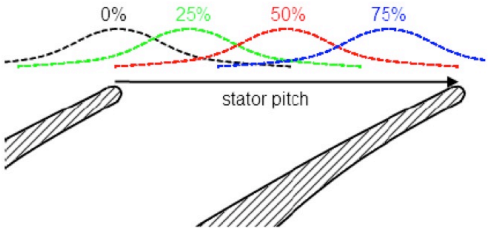

b.

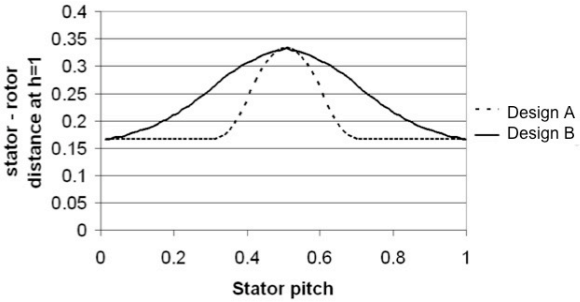

c.

Figure 2.8: (a) Non-uniform ring installed at the exit of the second stator, clocked at 25%. (b) Circumferential clocking positions of the non-uniform ring with respect to the stator trailing edge. (c) Design of the non uniform ring at cavity inlet for the two cases.

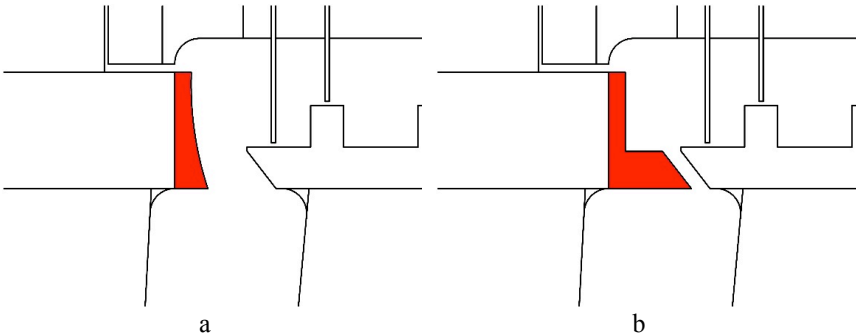

Figure 2.9: Inlet cavity configurations. Cavity volume reduction 14% for (a) and 28% for (b). Non-uniform 3D design for (a) and slanted design for (b).

In the slanted case the available inlet cavity area at span 1.0 was reduced by 85%. There was only a safety distance left between the stationary ring and the shroud. As it can be seen from Figure 2.9b there is no potential for the fluid to travel radially upwards and enter the cavity. If it is to enter the cavity then the fluid has to travel backwards. In this case the probe access is prohibited and therefore no experimental data are available.

2.1.4 Rotor Leading Edge Modifications

Three different leading edge geometries of the second rotor were tested in this study. The baseline case and the two modifications that are illustrated in Figure 2.10. The first modification has a positive metal angle, Figure 2.10a and the second a more negative Figure 2.10b, compared to the baseline case. The first modification has a positive metal angle to better match the positive incidence measured at the baseline case. On the contrary, the second modification received an even more negative metal angle. The profile of the blades was modified in the upper 30% of the blade height. Care was taken not to create a point of inflexion on both sides of the blades. Moreover, the centre of pressure was kept constant for all three cases examined. From this point on the modification with the positive metal angle will be referred to as Design A whereas, the modification with the negative metal angle as Design B.

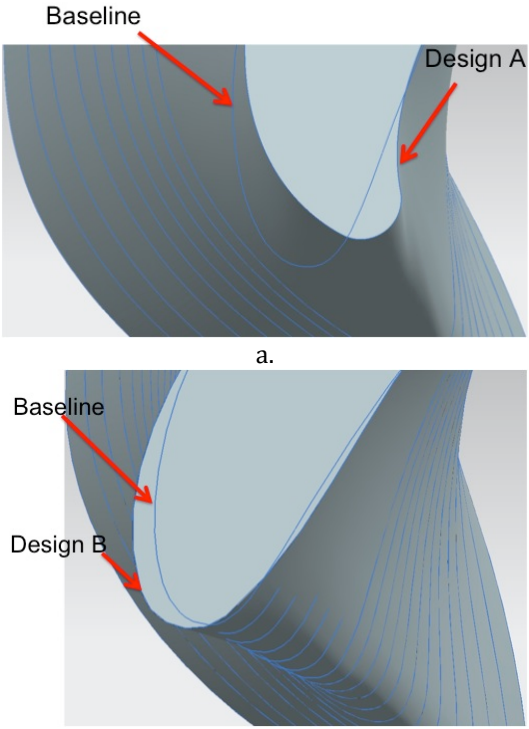

Figure 2.10: Modifications of the rotor leading edge (a) positive metal angle, +12° and (b) negative metal angle, -30°. Baseline metal angle is at -19° . Data are from 100% of the blade span.

2.1.5 Tip Clearance Gap

Two different tip clearance gap sizes were computationally studied and compared. The case 28.1 (Figure 2.6d) that had the best efficiency from the cases examined was used as a reference case, named case A. the case B had a reduced gap size of 50% compared to the reference case.

2.1.6 Swirl Brakers

Swirl brakers were installed at the rotor inlet cavity (Figure 2.11a). Having 1mm safety distance from the rotor shroud and 1mm from the upper axial cavity wall, 36 swirl brakers were installed one every 10°, same as the number of stator blades (Figure 2.11b). The swirl brakers are of 1mm in width reducing thus the total cavity volume less than 1 percent. The swirl brakers can be circumferentially clocked with respect to the upstream stator and positioned every 25 percent of the stator pitch. Steady and unsteady measurements were performed with the swirl brakers installed at 0 percent circumferential position. The swirl brakers were aligned with the stator trailing edge.

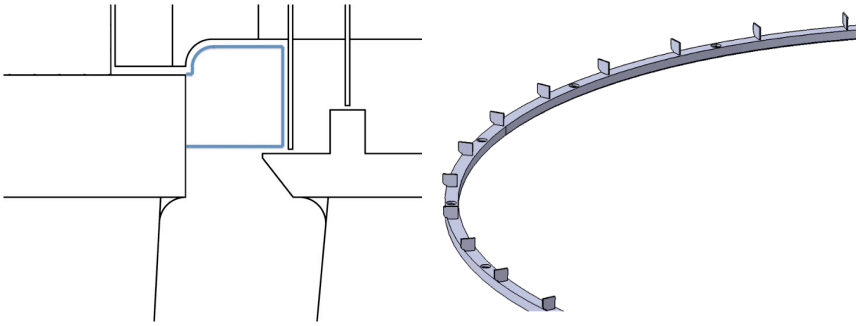

a. b.

Figure 2.11: (a) A meridional cut of the rotor inlet area with the swirl brakers installed and (b) the 3D design model of the swirl brakers ring

2.2 Data Acquisition

There are four independent main data acquisition chains, which include operating conditions, multi-channel pressure measurement system, vibration monitoring and probe measurement.

2.2.1 Operating Conditions

The measured operating conditions include pressures, torque, rotational speed, temperatures, humidity and massflow.

Pressure

Two 16 channel differential pressure PSI modules measure the most important operating pressures. This include the pressures used for the massflow calculations of the massflow measuring devices, the inlet total and static pressure, the ambient pressure and the hub and tip pressure values of each row. The inlet total pressure is measured with a pitot probe permanently mounted at half the channel height on thin struts. The struts are circumferentially displaced relative to the traverse area. All other pressure values are measured with wall pressure tappings of 0.5 mm diameter. The ranges of the two modules are 34.47kPa and 4.98kPa respectively. Apart from the pressures used for the massflow calculations all other pressures are measured against the same pressure reference to reduce uncertainties. As reference pressure a hub pressure at the exit of the first stage is used so as all sensors are operated in their optimum range.

Temperature and Humidity

At the turbine inlet and exit four PT100 resistance thermometers are used to acquire the air temperature. At the exit of the heat exchanger a PT100 thermometer measures and regulates the temperature used as input to the control loop. Additionally, the temperature is measured at the inlet of the measuring mass flow device. Prevention of condensation is done through a humidity sensor installed at the exit of the turbine.

Massflow meter

The massflow is measured with a calibrated ventouri nozzle. Since the upstream length does not conform with the minimum length defined is ISO 5167-3, the ventouri nozzle including the two upstream bends has been calibrated at Delft Hydraulics on a certified calibration rig. The discharge coefficient of the nozzle can be determined as a function of the Reynolds number. The calculation of the massflow requires the absolute pressure, temperature and humidity of the flow at the exit of the nozzle and the pressure drop across the nozzle contraction.

Torque

The first and second rotors are mechanically decoupled by means of two concentric hollow shafts. The second turbine stage is connected with a calibrated torquemeter through the hollow shaft. Inside the torquemeter two proximity sensors read the signal generated by two gears. When a torque is applied, a torsional deflection occurs on the shaft. The relative phase shift of the upper and lower transducer signals is proportional to the torque. By applying a set of calibration parameters, the actual torque can be measured. In Figure 2.2 the two shaft arrangement is presented.

Vibration

The vibration of the rotating parts are measured with displacement and acceleration sensors. The signal are processed and displayed by a Schenk vibration module (VibroControl 4000). It indicates the displacement amplitudes and vibration velocities. Three acceleration sensors are used to monitor the vibrations of the gearbox, one for the generator and four are located in the turbine bearings.

Multi-Channel Pressure Measurement System

The multi-channel pressure measurement system consists of two digital sensor array enclosures with Windows embedded operating system to allow Ethernet connection. The first enclosure is equipped with 3 ZOC16TC modules each containing 16 10'' H_2O range pressure transducers. Additionally, it contains two servo pressure calibrators SPC 3000 and the control pressure module CPM 3000 for the sensor calibration. The second enclosure contains 7 ZOC16TC modules each containing 16 5PSI range pressure transducers. The data acquisition and the conversion to engineering units is done through the Scanivalve DSMLINK V2.98 software. A full range calibration at the beginning of the campaign and a daily re-zeroing was performed to remove any offsets.

2.3 Probe Technology

2.3.1 Introduction

The flow field in turbomachines is highly unsteady and three-dimensional. Main contributors of this flow are the presence of secondary flows generated near the endwalls, due to the presence of cavities and leakage flows, the wakes shed from the blades. Generation evolution and propagation of such flows in axial turbomachine is of great importance if the aerodynamic performance is to be assessed and improved.

To gain deeper understanding of the flow and to improve the blade design the turbine designers are in need for measurement data. Hot-wire anemometry, laser Doppler anemometry (LDA) or pressure probe techniques, such as the FRAP probe for fast response measurements or 5-hole probe for steady flow measurements. The first two methods (anemometry) deliver only the flow velocity components but do not provide any information on the static and total pressure distribution in the flow field. This relevant quantity in turbomachinery (defines the thermodynamic state of the flow field) can only be derived from an intrusive method such as a pneumatic probe. Various probe concepts for pneumatic probe measurements have been developed in the past and are widely used in the academic and industrial environment. The most significant difference between those concepts is the number of holes that each probe uses to derive the flow quantities and the measurement frequency (steady or fast response probes). For pneumatic probe steady flow measurements, there exist single and multi-hole probes (Typical 1-, 3- , 4- and 5-Hole Probes). The pneumatic x-hole probes are commonly used for steady flow measurements. The well known 5-hole probe delivers the 3D flow velocity vector as well as the static and total pressure at a specific traversing point. It is currently considered as the most reliable for performance evaluation and reaches nowadays the complete development.

Due to the relative motion between the rotor and stator of a turbine wheel the resulting flow is always unsteady. The measurement of this flow field by means of pneumatic probes (steady) never delivers the required information for the rotor-stator interaction mechanism and is therefore not a useful tool to measure fluctuations in a turbomachine. In the early 70's the fast response pressure probes come into play. With the use of a semi conductor pressure sensor, Seeno et al. [67] and later Matsubaga et al. [47] measure two and three-dimensional flow with a single probe. In the next decade the sensors

were mounted on the probe directly [37, 16]. In the 90's the fast response probe designers focused on minimizing the probe head to reduce the blockage effects. All kind of different shapes have been suggested in numerous works [4, 22, 11].

A single sensor probe can provide information about the two-dimensional field. Using the 'virtual 3-sensor' mode in which the single sensor is yawed at three different probe angles. With the phase lock of the three measurements at the same blade position flow quantities can be evaluated only in there deterministic part as the stochastic part of the signal is lost. Fuijta and Kovasznay [19] initially applied the aforementioned technique using hot-wire anemometry. An additional sensor provides information on the turbulence intensity and Reynolds stress tensor, [29, 79, 23, 42, 54].

Nowadays, with extensive studies at the ETH the fast response aerodynamic probe has been developed, perfected and extensively used for unsteady measurements in compressors and turbines. Its reliability has been shown in numerous publications, [8, 55-58]

Pneumatic Probes

A 5-hole cobra shaped, and a 4-hole probes are used. The tip diameter of the 5-hole probe is 0.9 mm. The advantage of the cobra shaped probe is the large distance (5mm) of the probe shaft from the measurement volume. The probe was used for measurements at the exit of the rotors where sufficient space between bladerows existed. For the measurements at the second stator exit the 4-hole probe with elliptically shaped head was used with a tip diameter of 1.2 mm. Although less accurate it reduces blockage effects while measuring within the cavity. The simplicity of the measurement chain qualifies this technique to provide reliable reference data of the steady pressure field. The pressure tubes of the pneumatic probe connecting the probe tip with the pressure sensor causes frequency damping of the unsteady pressure signal. Therefore, the pressure read by the sensor is referred to as pneumatically averaged pressure.

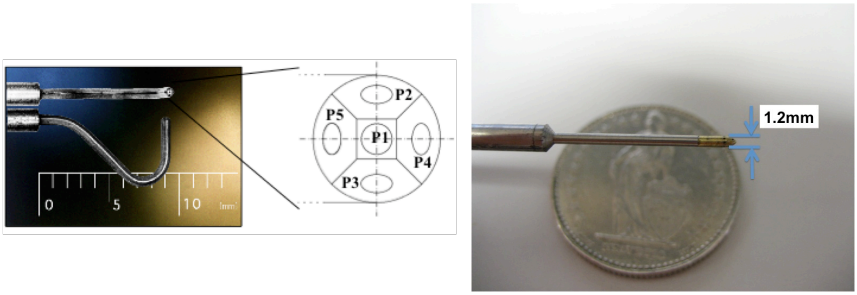

Figure 2.12: Cobra shaped 5-hole probe (left) and miniature 4-hole probe (right)

FRAP Probe

Time dependent flow parameters such as total and static pressures, flow angles and Mach No. can be evaluated using the Fast Response Aerodynamic Probe (FRAP). The FRAP technology has been developed over the last 2 decades in the LEC at ETH Zurich. Initially developed by Kupferschmied [37] and Gossweiler [22] it is nowadays widely used to measure the highly unsteady flow of the turbomachines. The measurement concept is based on emulating a 4-sensor probe using 2 sensors. The concept is graphically presented in Figure 2.13. The yaw sensitivity is gained from rotating the probe in 3 angular positions. A middle one and $\pm 42^{o}$. As a result of the virtual approach only the periodic part of the time-resolved yaw angle information can be resolved due to phase locking. The probe is capable of capturing unsteady flow features up to frequencies of 48Hz concerning total and static pressure, flow angles and the Mach No. whereas, the temperature is limited to a frequency of 10Hz. The probe head is cylindrical with an inclined, curved tip. The probe body at the tip has a miniature diameter of 1.8mm that allows for measurements inside the cavities with minimum blockage.the probe tip contains two pressure taps with a diameter of 0.35mm. One sensor is located in the cylindrical part and the second in the inclined surface of 45° 2.5mm apart. At the back side of each pressure tap a piezo-resistive pressure sensor is located. The pressure tap with the sensors are sealed and the internal part of the probe can be pressurized providing the necessary back pressure. The signal acquired is transmitted to the amplifier at the back of the probe. The probe tip shape has been developed and applied to two complimentary single-sensor FRAP by Pfau [56]. The probe tip diameter of these probes is 0.84mm. One is yaw sensitive and the other is used for the pitch measurement.

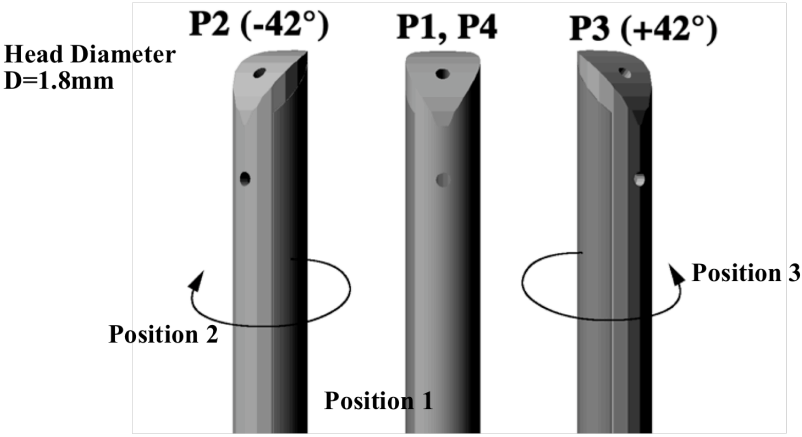

Figure 2.13: Measurement concept in virtual 4-hole mode with 2-hole probe

2.3.2 Calibration

Freejet facility

Before using the probes for the flow measurements the calibration against a known reference has to take place. They are calibrated in the freejet facility against yaw and pitch angles and total and static pressure at a given Mach number. The axisymetric freejet has a uniform velocity profile and a turbulence level of 0.3%. The nozzle diameter at the exit is 100mm. A detailed description of the facility can be found in Kupferschmied [37] In the freejet facility the probes can be calibrated for a yaw angle range of $\pm 180^{o}$ and a pitch angle range of $\pm 36^{o}$ and for a maximum Mach number of 0.9.

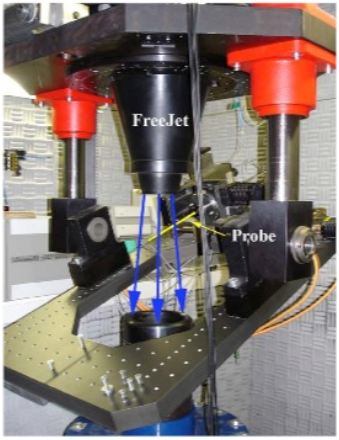

Figure 2.14: The freejet facility used for the aerodynamic calibration of the probes, [45]

Pneumatic 5-Hole Probe

The cobra-head pneumatic 5-hole probe is used for measurements of the steady 3D flow. The probe consists of a soldered bundle of four tubes arranged around a center tube. The tip of the probe has a diameter of 0.9mm is shaped as a quadratic pyramid with 45° inclined surfaces and a chopped tip. The holes are located in the center of each one of the surfaces with the centered hole being on a surface, which is orthogonal to the probe tip axis. The 5-hole probe has been calibrated for a yaw and pitch angle range of $\pm 20^o$ in steps of 2°. The probe was calibrated for a Mach number of 0.1 corresponding to the Mach number at the exit of the rotors. Out of a calibration a set of coefficients is determined. The equations to evaluate the sensitivity coefficients K_i are given below.

$$K_\varphi = \frac{p_2 - p_3}{p_m},\ K_\gamma = \frac{p_4 - p_5}{p_m},\ K_t = \frac{p_t - p_1}{p_m},\ K_s = \frac{p_t - p_s}{p_m} \quad (2.1)$$

with

$$p_m = p_1 - \frac{1}{4}\sum_{i=2}^{5} p_i \quad (2.2)$$

Pneumatic 4-Hole Probe

The 4-hole probe has been calibrated for a yaw and pitch angle range of ±20° in steps of 2°. The probe was calibrated for a Mach number of 0.3 corresponding to the Mach number at the exit of the stators. Out of a calibration a set of coefficients is determined. The equations to evaluate the sensitivity coefficients K_i are given below.

$$K_\varphi = \frac{p_2 - p_3}{p_m},\ K_\gamma = \frac{p_1 - p_4}{p_m},\ K_t = \frac{p_t - p_1}{p_m},\ K_s = \frac{p_t - p_s}{p_m} \quad (2.3)$$

with

$$p_m = p_1 - \frac{1}{2}\sum_{i=2}^{3} p_i \quad (2.4)$$

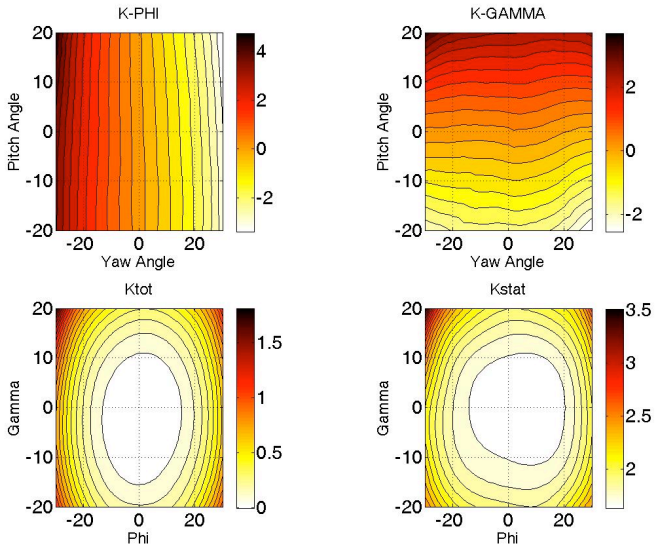

Figure 2.15: calibration charts of the 5-hole pneumatic probe at Ma=0.3

FRAP Probe – sensor calibration

The pressure sensor used in the FRAP probe comprises of four piezo-resistors connected on a Wheatstone bridge. The excitation of the electrical circuit by constant current generates an output voltage signal U pressure dependent and a U_e temperature dependent. In order to quantify the pressure and temperature sensitivity of the sensors a 3rd order interpolation is used to derive the relationship between U, U_e and the pressure and temperature. The probe is exposed to different temperature steps, which are expected during the measurement. At each temperature step the pressure is varied undergoing a cycle of pressure levels.

FRAP Probe – aerodynamic calibration

The probe calibration for role angles of $\pm 80^o$ in steps of 2° to emulate the two missing sensors and pitch angle of $\pm 25^o$ in steps of 5°. The usable range of the probe is determined by the pressure distribution around the probe head. The pressure on the holes has to evolve monotonically, which is the case until

72° limiting the probe yaw angle range to ±30°. The calibration coefficients are identical with the one used for the 4 hole pneumatic probe.

2.3.3 Traversing System and Resolution

Traversing System

The test rig is equipped with a 3-axis fully automated traversing system. Two stepper motors move the probe in radial direction and rotation around its axis. The third motor enables the tower to move in the circumferential direction. The turbine is equipped with sliding rings that allow sliding between the casing rings. The design is well explained in Schlienger [64]. The accuracies and ranges of the traversing systems are given in Table 2.4.

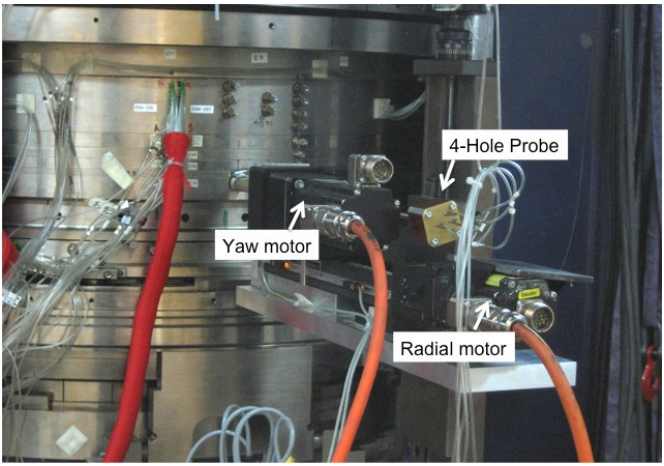

Figure 2.16: The traversing system of the probe mounted on the traversing table of the rig

Traversing Axis	Range	Accuracy
Circumferential	45°	0.002°
Radial	150mm	0.1mm
Yaw Angle	360°	0.003°

Table 2.4: Range and accuracies of the traversing system

Resolution

The spatial resolution of the measurement grid for a pneumatic area traverse consists of 48 radial clustering near the end walls and 60 circumferential points, which covers three stator pitches, 30°. The last traverse should be such that repeats the first one so that the periodicity is checked.

2.4 Data Reduction

2.4.1 Pneumatic Probe Data

The pneumatic data post processing can be divided into two steps:

1. Data - Processing

2. Visualization

Data-Processing

The operational and probe data are logged with the same time stamp. The calibration coefficients along with the 4/5-hole pressures the flow angles, total and static pressure are calculated with the polynomials given below:

$$\begin{aligned}
\varphi &= \sum_{i=0}^{6}\sum_{j=0}^{6} a_{\varphi,ij} k_{\varphi}^{i} k_{\gamma}^{j} \\
\gamma &= \sum_{i=0}^{6}\sum_{j=0}^{6} a_{\gamma,ij} k_{\varphi}^{i} k_{\gamma}^{j} \\
k_t &= \sum_{i=0}^{6}\sum_{j=0}^{6} a_{t,ij} \varphi^{i} \varphi^{j} \\
k_s &= \sum_{i=0}^{6}\sum_{j=0}^{6} a_{s,ij} \varphi^{i} \varphi^{j}
\end{aligned} \tag{2.5}$$

The coefficients α_φ ,α_γ,α_s and α_t of the polynomial approximation can be determined by a Gaussian least square fit method. The degree of polynomial approximation defines the fitting of the line to the points of the calibration. Higher order polynomial approximations although better fits to the points it is prompt to introduce unphysical oscillations. On the other hand, the use of lower order does not always fit to the points.

With the associated time stamps the operating conditions of the turbine are assigned to each probe measurement point. Through triangulation the measured calibration coefficients are related to the calibration data. The turbine flow angles together with the total and static pressures are derived. Positive flow yaw angle is in the direction of rotor rotation, while positive flow pitch angle is for fluid moving radially outwards. Since the turbine loop is open to atmospheric conditions, the measured pressure should be corrected to account for daily changes in the atmospheric pressure. This correction is done through the non-dimensional pressure coefficient C_p.

$$C_p = \frac{p_i - p_{s,ex}}{p_{t,in} - p_{s,ex}} \tag{2.6}$$

The visualization can be done either as line plots or area plots.

2.5 Uncertainty Analysis

To correctly interpret the highly unsteady flows in turbomachinery, to validate the numerical tools and to perform an evaluation of the components based on experimental results it is essential that the measurement uncertainties are known. The Guide of Uncertainty in Measurements (GUM) [33] is used to perform the necessary uncertainty analysis. According to this method all uncertainties are initially converted to probability distributions. In the case of pressure measurements in turbines the evaluation of the correlated parameters and their combined uncertainty is in need of initially defining cross-correlated parameters. DIN 1319-3 accurately defines the evaluation process of the results with their associated uncertainty. According to this method the evaluation strategy can be structured by the following four steps:

1. Development of the model, which describes the measurement problem in the form of mathematical equations.

2. Preparation of the input data and of additional information.

3. Calculation of the results and the associated standard uncertainties with the given input quantities and the given model.

4. Notification of the complete measurement result including the measurement uncertainty.

In the 2nd step the data have to be expressed as probability distributions. Based on the distribution the expected value as well as the variance can be calculated. The GUM method differentiates between two kinds of input data.

Type A: observed statistical data collected during a measurement

Type B: Non-statistical data, which are known prior to the measurement

As an example, if there is no specific knowledge about the possible intermediate values and only the upper and lower limits are known, then a rectangular probability distribution is recommended. The standard uncertainty u of the rectangular distribution with a known half-width a is calculated as

$$u(x_i) = \frac{a}{\sqrt{3}} \tag{2.7}$$

in the 3rd step the partial derivatives of the model function y are calculated to obtain the sensitivity c_i of every input quantity x_i

$$c_i = \frac{\partial y}{\partial x_i} \tag{2.8}$$

the uncertainty contribution $u_i(y)$ is calculated by a multiplication of the sensitivity coefficient c_i with the standard uncertainty of the input quantity

$u(x_i)$.

$$u_i(y) = c_i \cdot u(x_i) \tag{2.9}$$

The law of the error propagation is given as follows:

$$u^2(y) = \sum_{i=1}^{n} u_i^2(y) \left[+2 \cdot \sum_{i=1}^{n-1} \sum_{j=i+1}^{n} r(x_i, x_j) \cdot u_i(y) \cdot u_j(y) \right] \tag{2.10}$$

The GUM method uses a term called expanded uncertainty U, defined as

$$U = k \cdot u(y) \tag{2.11}$$

The choice of the factor k, which is usually in the range of 2 to 3, is based on the coverage probability or level of confidence required of the interval. A coverage factor of k=2 is used, which corresponds to a confidence level of 95%. Behr [8] has calculated the error propagation for the pneumatic 5-hole probe technique using the calibration polynomial model. In the Table below the uncertainty for the probe for an expansion factor of 2 and for the Mach numbers of 0.1 and 0.3 is given.

Flow quantity	M=0.1	M=0.3
Yaw angle	1°	0.3^o
Pitch angle	1.1^o	0.35^o
Total pressure	80Pa	90Pa
Static pressure	90Pa	110Pa

Table 2.5: Expanded uncertainty of the pneumatic 5-hole probe

Massflow

In order to derive the expanded uncertainty of the mass-flow meter and the turbine efficiency the two model functions are needed. The massflow calculation is performed as follows

$$m_i = \frac{\pi}{4} d^2 \frac{C_d}{\sqrt{1-\beta^4}} \varepsilon \sqrt{2\Delta p \rho} \tag{2.12}$$

In the Table below the full scale uncertainties of all measurement devices are given. All input data are converted into rectangular distributions with a half-width corresponding to the indicated uncertainty.

Measurement device	Parameter	Range	Uncertainty
Scanivalve ZOC16	Δp	0…35kPa	±0.065%FS
PSI 9016 diff. press.	Δp_{υ}	0…5kPa	±0.15%FS
PSI 9016 diff. press.	Δp	0…35kPa	±0.065%FS
Keller X33 abs. press.	p_{atm}	0.8…1.2bar	±0.05%FS
Resistance thermometer	T	0…60°C	±0.3%FS
Relative humidity sensor	H	0…100%	±1.0%FS

Table 2.6: Accuracy of measurement devices

Input quantity	Parameter	Relative uncertainty $\Delta x/x$
Discharge coefficient	C_d	±0.16%
Throat diameter	d	±0.002%
Inlet diameter	D	±0.001%

Table 2.7: Accuracies related to the main Ventouri

Based on the GUM method the extended uncertainty of the turbine massflow is ±0.22%. The two main contributors of the massflow uncertainty are the uncertainties of the discharge coefficient of the calibration procedure (53%) and the differential pressure measurement across the ventouri (45%). The rest 3% is contributed by the absolute pressure measurement, the humidity and the temperature measurement, [18].

Efficiency

The total-to-static efficiency of the second stage is evaluated according to the equation (2.13).

$$\eta = \frac{\omega \cdot T_q}{\dot{m}_{2^{nd},stage} \cdot C_p T_{in} \left[1 - \left(\frac{p_{s,ex}}{p_{t,in}} \right)^{\frac{k-1}{k}} \right]} \tag{2.13}$$

The total pressure at the inlet of the second stage is the mass-averaged total pressure measured by the 5-hole probe at the R1exit. The static pressure at the exit of the second stage is measured by tapings at the exit of the turbine at the hub. The measured speed and torque are taken from the operation file and are averaged over the probe traversing period. The inlet temperature is not measured directly but estimated using the measured inlet and exit temperature of the turbine. The expanded uncertainty (k=2) according to the GUM-method for the total-to-static efficiency is 0.27%, [18].

2.6 CFD

The numerical study was performed using the ANSYS CFX flow solver. The second stage of the turbine (Figure 2.17) was meshed using an unstructured mesh with 8 million nodes, as shown in Figure 2.17. The stator-rotor blade count ratio of the second stage is 3:4. As the periodicity is related to the stator-rotor blade count ratio, 30 deg were meshed; i.e. three stator passages and four rotor passages. The y^+ values on the walls were all below 30. The flow solver was run in unsteady mode using the transient rotor-stator interface. The results of the steady simulations were used as initial conditions. As a convergence criterion a reduction of the maximum mean square value for the residual from 10^{-2} to 10^{-6} was used. The standard k-ε turbulence model with a turbulence intensity of 5% at the inflow boundary layer was employed. The experimentally measured mass-averaged total pressure, together with the flow angle distribution and the static temperature constituted the boundary

conditions at the inflow, whereas at the outflow the measured static pressure distribution was used for the steady simulation, which provided a good initial solution. The circumferential boundaries are periodic and a no-slip condition was applied at the adiabatic walls. The cavities at the hub were not simulated; instead a clean endwall has been modelled. It was assumed that the hub cavity flows did not influence the flows at the top region of the blade.

The inlet cavity was modeled using 25-30 elements along its radial length and 20 in the axial direction. The positioning of the interface between the two domains inside the cavity is of great importance. The cavity is influenced by both the stator pressure exit flowfield and the rotor potential flowfield. The position of the interface has to ensure the full transition of the flow from one side to the other in both directions. In Figure 2.15b the position of the interface is shown marked with a green line.

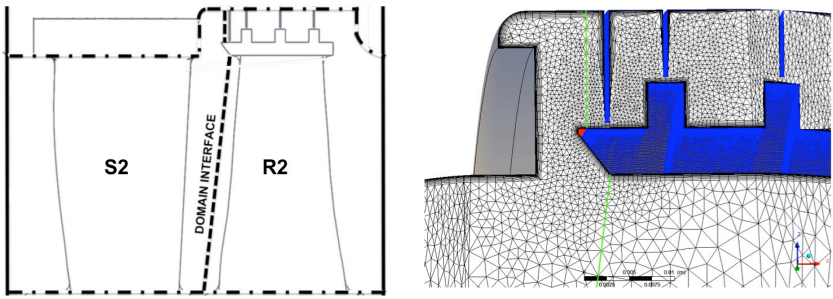

a. b.

Figure 2.17: The simulation domain is bordered by the measurement planes, solid lines at stage inlet and outlet. The center line sketches the simplified fluid path without the stator hub cavity. The domain interface is indicated by the dashed line

The model was compared against the experimental results (Figure 2.18). A difference between the experimental and numerical results is only present in the trailing edge of the blade, reaching up to 0.5%.

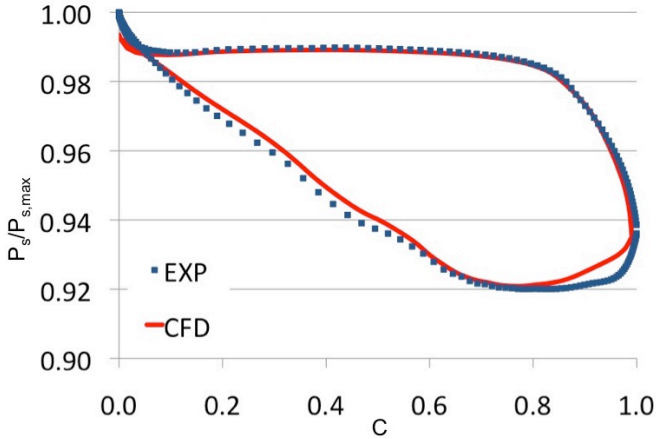

Figure 2.18: Pressure distribution on the LS stator blade. Comparison between experimental measurement and CFD

Validation

The computational model was validated against the mass-averaged averaged experimental results. The baseline case was used. The axial velocity and the yaw flow yaw angle were compared at the stator exit.

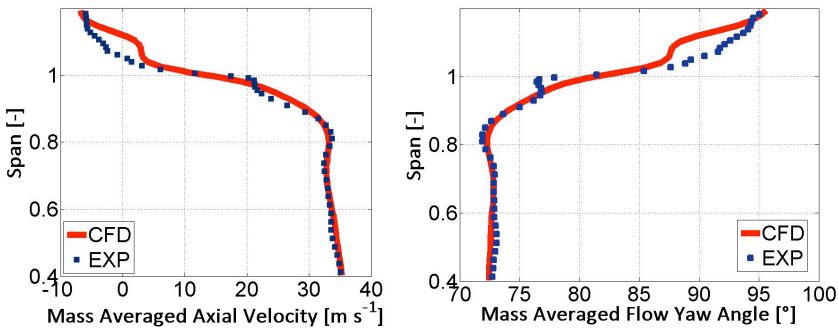

a. b.

Figure 2.19: Comparison of experiment and CFD for (a) the pitchwise mass-averaged flow yaw angle distribution and (b) the pitchwise mass-averaged axial velocity distribution at stator exit.

There is a very good agreement within 0.5 deg for the yaw angle up to 0.95 of the span. The CFD does not predict the underturning of the flow close to the upper casing. Moreover, inside the cavity, because of the strong secondary flows and due to the large flow pitch angles that cannot be captured by the probe the difference between experimental and computed results rise up to 5 deg. The pitchwise mass-averaged axial velocity shows a very good agreement over the blade span. The difference is within 1 m/s. Inside the cavity although the trend is captured the CFD predicts higher velocities.

3. Turbine Performance and Flowfield

3.1 Efficiency

The operating point of the turbine was set to a specific pressure drop that was accurately repeated on every measurement day. Since the exit of the turbine was open to the atmosphere, the atmospheric pressure determines the level and the density of the turbine flow, mass flow variations at constant pressure drop occurred. Throughout the measurement campaign the maximum atmospheric pressure variation was 2000 Pa. Therefore, the average atmospheric pressure in Zurich city was used for reasons of non-dimensionalizing. In the table below the total-to-static efficiency values of all the test cases considered in this study are shown. The total-to-static efficiency of the baseline case is used as a reference.

The first stage of the turbine does not influence the efficiency of the turbine since no hardware change takes place. The flow inlet conditions to the second turbine stage are the same for all cases studied. The axial extension of the stator upper casing although it acts beneficially meets a deflection point and the efficiency drops again. On the other hand, radial cavity wall reduction proved to be advantageous. All cases with radial cavity wall length reduction increased efficiency. The optimum test case was 28.1. The slanted and the non-uniform cases did not lead to efficiency gain.

For all cases it was made evident that the handling of the cavity vortex both in terms of size and positioning play an important role. The mass flow enabled in the cavity vortex was interacting with the main flow fluid leading to, depending on the vortex position mixing at the cavity inlet area. Additionally, the mass flow distribution inside the cavity between the flow getting trapped by the cavity vortex and the one that counter rotated in front of the fin and over the shroud was of high significance.

Case		ΔEfficiency
Baseline		0%
14.0		+0.33%
14.1		+1.1%
14.2		+1.2%
28.0		-0.2%
28.1		+1.5%
28.2		+0.8%
Slanted		-0.3%
Non-uniform	25	-0.1%
	50	-0.2%
	75	0%
Swirl braker		-0.3%

Table 3.1: Changes of efficiency for the test cases considered

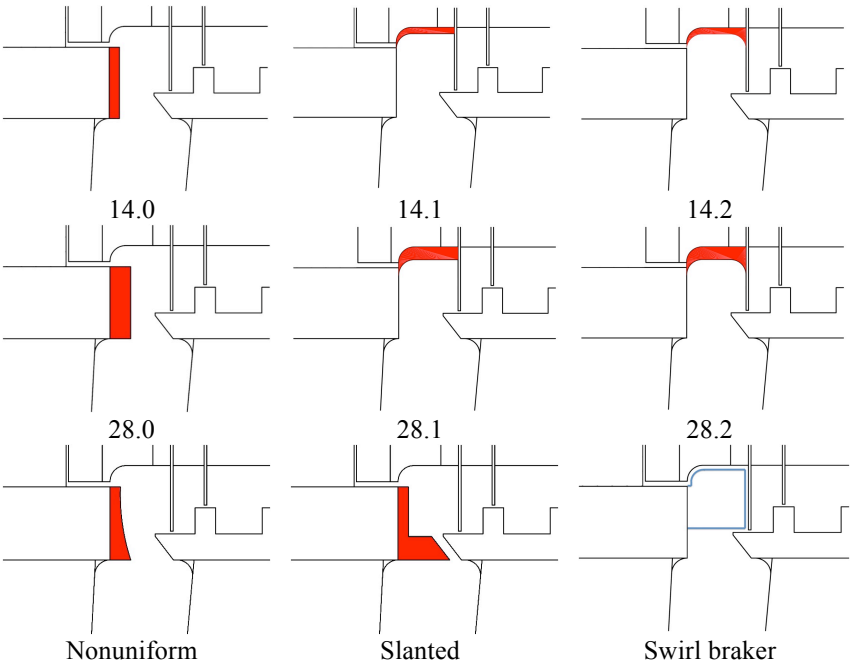

Table 3.1: cases examined

3.2 Inlet Flowfield to Second Turbine Stage

The pitchwise mass-averaged distribution of the axial velocity and the flow yaw angle are depicted in Figure 3.1. The measurement plane is located at $0.7C_{ax}$ upstream of the stator blade at 50% of the blade span. Overturning and underturning is observed between 10%-30% and 80%-95% indicating the location of the hub and tip passage vortices. The regions are also identifiable at the axial velocity distribution plot. The impact of the shroud is visible at the upper 10% of the blade span where the axial velocity decreases by almost 15m/s. As far as the flow angle is concerned on the same region the difference between the leakage flow and the main flow angle reaches 20 degrees.

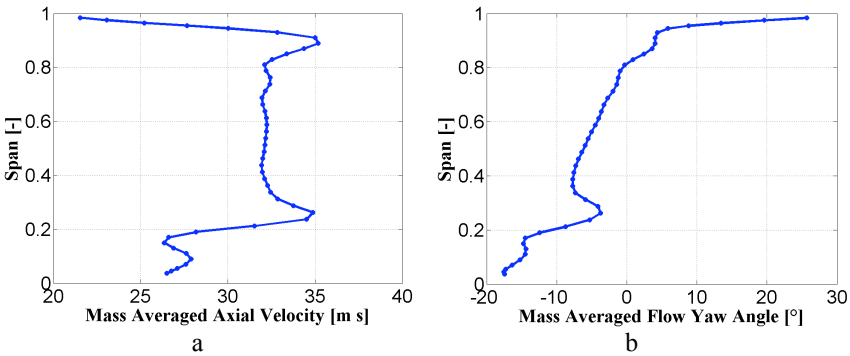

Figure 3.1: Pitchwise mass-averaged profile at the inlet of the second stage, (a) axial velocity, (b) flow yaw angle

4. Impact of Cavity Volume on Efficiency

4.1 Axial Cavity Wall Length Reduction

The experimentally measured stage efficiency for the three cases examined in this work is shown in Figure 4.1. Overall, the efficiency increases by 0.33% for the 14.0 compared to the baseline case. A further reduction of 28.0 to the initial CV decreases the efficiency by 0.2% compared to the baseline case.

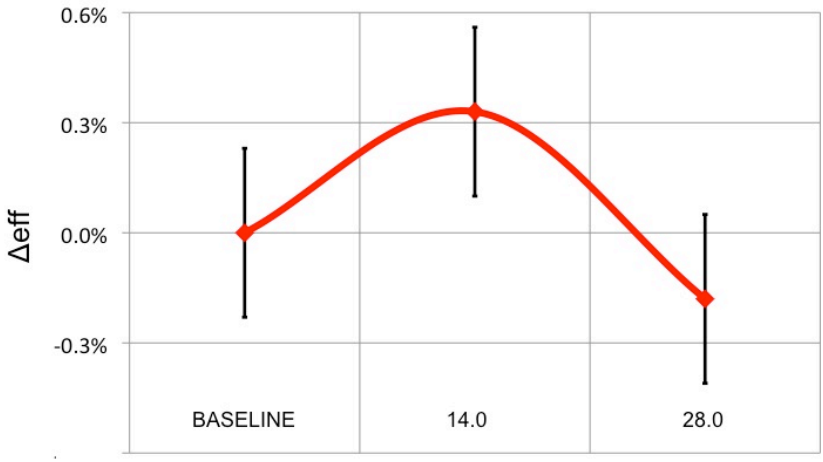

Figure 4.1: Δeff for the baseline, 14.0 and 28.0. Efficiency of the baseline case with the initial cavity volume used as a reference.

The experimentally measured total pressure loss coefficient at stator exit for the three cases is presented in Figure 4.2. The total pressure coefficient is pitchwise mass-averaged. Above 100% span the measurements are of flow inside the cavity. The extension of the upper casing results in lower loss generation in the region where the boundary layer develops, from 0.9 – 1.0 span. The boundary layer that forms on the upper stator casing exits the stator blade passage and continues turning as long as the casing still exists, until it reaches the cavity entrance, where it experiences a sudden, shear-generating turn in the circumferential direction. An elongated platform provides the necessary boundary for the flow to continue overturning and therefore less shear is observed downstream of the stator exit, as shown in Figure 4.2. Inside the cavity, a reduced volume lowers the pressure, which in turn lowers the pressure difference and hence the driving force of the flow across the labyrinth between the inlet and exit cavities. Nevertheless, the leakage fraction derived as the ratio of leakage to main mass flow for the three cases examined, given in Table 4.1, does not vary significantly. The shortening of the cavity's axial length along with the CVR does not affect the amount of the leakage flow that finally escapes through the labyrinth as both CVR cases experience a leakage flow that differs by no more than 1.5% compared to that of the baseline. Moreover, the geometry changes of the cavity inlet do not affect the flow field below 90% of the blade span at stator exit.

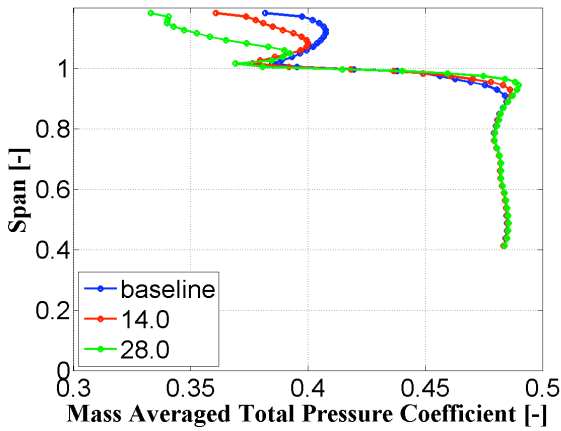

Figure 4.2: Experimentally measured pitchwise mass-averaged total pressure coefficient at stator exit.

Case	Baseline	14.0	28.0
Leakage fraction [%]	1.22	1.24	1.21

Table 4.1 Leakage fraction at inlet cavity.

Contrary to the trend observed at the stator exit, no trend is observed at the rotor exit. In Figure 4.3, the pitchwise mass-averaged flow pitch angle distribution at the rotor exit is presented. While there is a similarity between the baseline case and the 28.0 case, the flow field is significantly different for the 14.0 case. The tip passage vortex of the 14.0 case is considerably reduced in both size and magnitude and seems not to affect the flow field at lower spans unlike the two other cases, as shown in Figure 4.3. Large non-uniformities are present for the baseline case and the 28.0 across the whole span, notably at 0.7 and 0.4-0.6. A larger vortex at the rotor exit circulates more mass flow and ultimately leads to more mass flow being exchanged. A larger vortex, manifested by the larger mass-averaged pitch angle in Figure 9, occupies more space in the tip section of the blade as it extends to lower span locations. Therefore, the flow underneath is squeezed. Additionally, due to more mass flow being handled by the tip passage vortex, the formation of smaller vortices in series across the span is facilitated, giving larger mass-averaged pitch angle oscillation at mid-span. While the shortening of the axial inlet cavity gap is beneficial in terms of loss generation at rotor inlet, the flow field at rotor exit seems to cancel out that benefit. In the following, the results of the unsteady computational analysis are presented in order to examine this flow behavior in more detail.

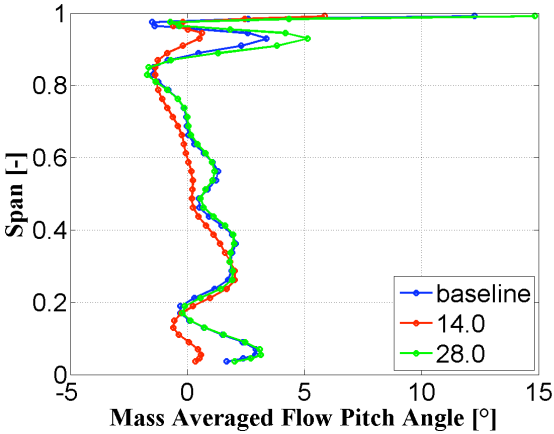

Figure 4.3: Experimentally measured pitchwise mass-averaged flow pitch angle at rotor exit.

Overall, three different phenomena affect the flow field in the cavity area. Firstly, there is a captive vortex in a driven cavity. As the flow exits the stator passage at an angle to the blade and passes underneath the cavity, it drives the flow of the cavity into a circular motion. Secondly, the flow that has been turned within the stator passage tends to move upwards on the pressure side of the stator blade and downwards on the suction side. Once the opposite moving flows reach the cavity entrance they interact with the cavity flow. Lastly, the pressure side leg of the horseshoe vortex that has already started to form on the rotor blade is highly affected by the interaction of the upward moving jet with the cavity flow. Although the aforementioned are valid for the baseline case and the 14.0 case, they are not observed in the 28.0 case, since there is no vortex formation within the cavity due to the lack of the necessary axial gap. The cavity volume impacts drastically on the flow vortex that dominates the entire cavity. The core is located in the middle of the upper half of the cavity at h=1.11 and stays steady during in and outflow. The vortex is fed by high-pressure fluid originating from the pressure side of the stator blade. With a 0.17c extension of the stator casing and during inflow the vortex migrates slightly higher to h=1.12, but it remains unaffected in terms of size, as seen in Figure 4.4b. Nevertheless, during outflow (Figure 4.4e), an additional vortex appears at the lower part of the cavity at the interaction zone. Right after the rotor blade trailing edge passes by, the newly formed

vortex interacts with the main flow at a ratio of 3:4 with the rotor pitch. It disappears when close to the pressure side of the rotor blade, as high-pressure fluid, coming from the stator and influenced by the potential flow field of the rotor is redirected upwards and inside the cavity. The situation undergoes a dramatic change when the cavity inlet is reduced even further to 0.34c, as in Figures 4.4c and 4.4f. The flow is characterized by a total absence of a toroidal vortex inside the cavity. When at the pressure side of the rotor blade, the cavity is washed out along its whole radial length by a strong upward-moving jet. What used to form the toroidal vortex now appears to be attached to the upper axial wall of the cavity with considerably reduced size and strength. On the suction side of the blade a downward moving jet dominates the cavity. Two small corner vortices appear attached to the shroud. An initially large vortex that was axially confined finally splits into two smaller vortices of the same rotational sign.

For both the cases where the toroidal vortex is formed within the cavity, the fluid will exit the cavity when the low-pressure fluid originating from the suction side of the stator blade passes underneath. By extending the upper casing platform by 17% of the axial cavity gap, the flow is hindered from exiting the cavity and this happens at a location further downstream. The remaining 83% of the axial cavity length has to accommodate both the ingress as well as the egress of the flow. The large vortex in the baseline case extends inside the main flow contrary to the 14.0 case, where the lower branch of the bifurcated vortex, being smaller in size, does not penetrate into the main flow, as shown in Figure 4.5. Bearing in mind that in both the baseline and 14.0 cases the mass flow handled is within the limited range of 1.5% based on the baseline leakage flow, the vortex of the lower half of the cavity of the 14.0 case will only circulate half of the mass flow compared to the baseline case.

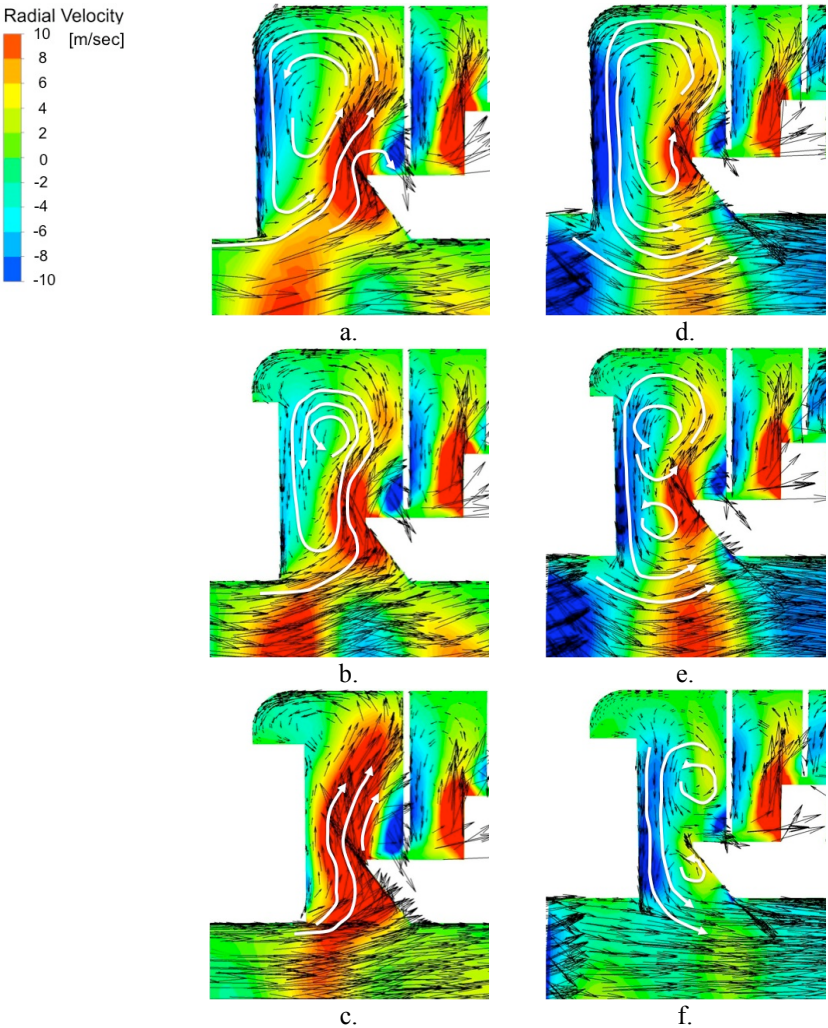

Figure 4.4: CFD simulations of the inflow for the cases (a) baseline, (b) 14.0, and (c) 28.0; and the outflow for the cases (d) baseline, (e) 14.0, and (f) 28.0. The simulations show a meridional cut on the pressure for (a), (b) and (c), and on the suction side for (d), (e) and (f) of the rotor blade. The planes are colored with radial velocity and the secondary flow vectors are projected onto them. The flow path is denoted by white lines.

The other half is trapped in the upper branch. Therefore, half the mass flow will be involved in the mixing process at the interaction zone during outflow. When the axial cavity length is reduced even further, the gap size is insufficient for a vortex to be formed to handle the leakage mass flow. A jet appears instead and flushes the cavity in and out.

Cavity flows at the interaction zone are influenced both by the stator and the rotor. The stator and the rotor have the same influence zone extending to 60% of the initial axial cavity gap on either side. In Figure 4.6, the mass fluxes at a point in time are plotted over the repeating stage and the axial cavity entrance length at the cavity inlet. Red colored areas show the radially upward-moving fluid, whereas the blue colored areas represent the fluid egress. On the stator side of the plot 3 peaks and troughs can be identified, which are related to the 3 stator blades of the repeating sector, whereas on the other side 4 rotor blades interact with the cavity entrance. The superimposition of the upward-moving fluid originating from the pressure side of the stator blade on the fluid that is redirected radially upwards due to the rotor potential flow field occurs in the middle of the cavity for the baseline case, and is shown with a solid circle in Figure 4.6a. Shortening the axial cavity length by 0.17c reduces the stator influence on the interaction zone. The flow is more rotor-driven and the maximum mass flux ingress occurs further downstream due to the shortened length, shown by the solid circle in Figure 4.6b. In the 28.0 case, Figure 4.6c, the influence of the stator has completely disappeared and the flow is only rotor-driven along its whole length. This is evident as the four peaks and troughs are clearly identifiable as originating from the rotor potential flow field. The reduced streamwise direction of the flow impacts negatively on the efficiency as negative incidence is imposed on the rotor blade. The ratio of the cavity's axial-to-radial wall length determines the flow kinematics in terms of vortex size. A ratio of 0.44 in the baseline case allows the formation of one large vortex that dominates the entire cavity. While maintaining the main flow velocity at the stator exit, a decrease of the ratio to 0.33 in the 14.0 case forces the vortex to be broken up into two smaller, vertically aligned vortices that would maintain their characteristics if there was no intervention by an external force. Although the overall mass flux along the cavity's axial gap follows an identical flow pattern, there is an area in the 14.0 case, highlighted by the solid black line in Figure 4.6b, where the radial mass flux is increased by 23% because of the smaller axial gap compared to the baseline case. As a result of this increased mass flux, the bifurcated vortex reconnects.

Figure 4.5: Schematic of vortex bifurcation during outflow and reconnection during inflow for the 14.0 case

The maximum mass flow ingress occurs at a more downstream position, at 0.72c for the 14.0, as compared to the baseline case where the largest inflow is in the middle of the axial gap. However this inflow is spread over the larger axial cavity length, as can be seen in Figure 4.7. The maximum inflow for the 28.0 case lies between the two previous cases, at 0.62c with its maximum being a 54% increase relative to the baseline case. With an axial-to-radial wall length ratio of 0.22 for the 28.0 case, the magnitude of the peaks of the mass flow cavity ingress show that the magnitude of the maximum mass flow increases monotonically with the ratio of the axial-to-radial cavity wall lengths.

The greater mass flow exchange at the interaction zone for the baseline case results in a larger tip passage vortex being formed on the pressure side of the rotor blade. The downward-moving flow of the stator suction side is enhanced by the egress of the cavity fluid. This flow, together with the upward moving fluid, continues along a streamwise path until it intersects with the rotor leading edge. This pair of fluids that move opposite to each other can potentially evolve to form a vortex with the same sign of rotation as the pressure side leg of the horseshoe vortex.

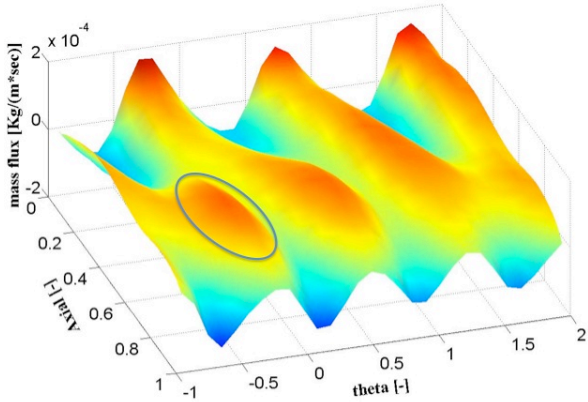
x 10^-4
mass flux [Kg/(m*sec)]
2
0
-2
0
0.2
0.4
0.6
0.8
1
Axial [-]
-1
-0.5
0
0.5
1
1.5
2
theta [-]

a.

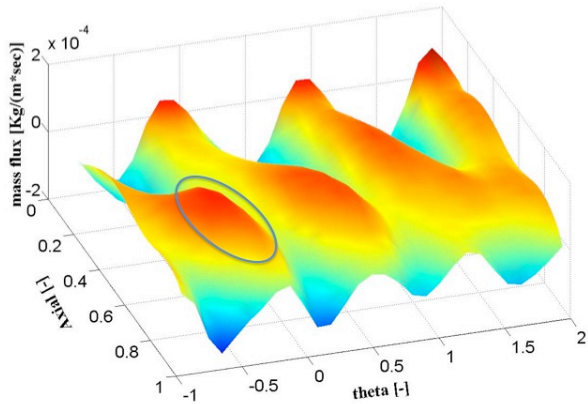
x 10^-4
mass flux [Kg/(m*sec)]
2
0
-2
0
0.2
0.4
0.6
0.8
1
Axial [-]
-1
-0.5
0
0.5
1
1.5
2
theta [-]

b.

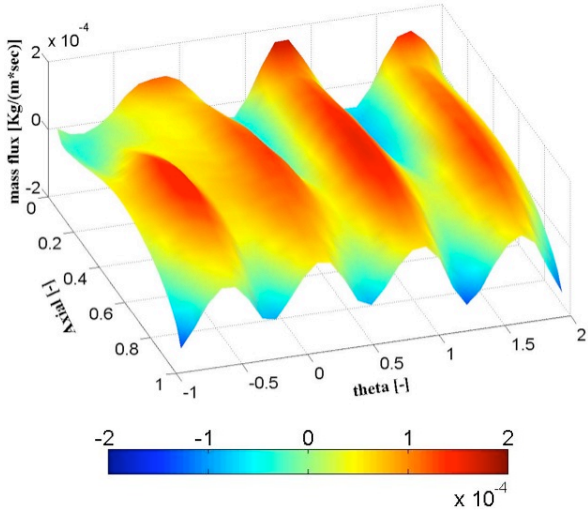

c.

Figure 4.6: CFD predicted instantaneous mass fluxes at cavity inlet for (a) baseline, (b) 14.0 case, and (c) 28.0 case. Red colored areas show fluid moving upwards, blue colored areas show fluid exiting the cavity

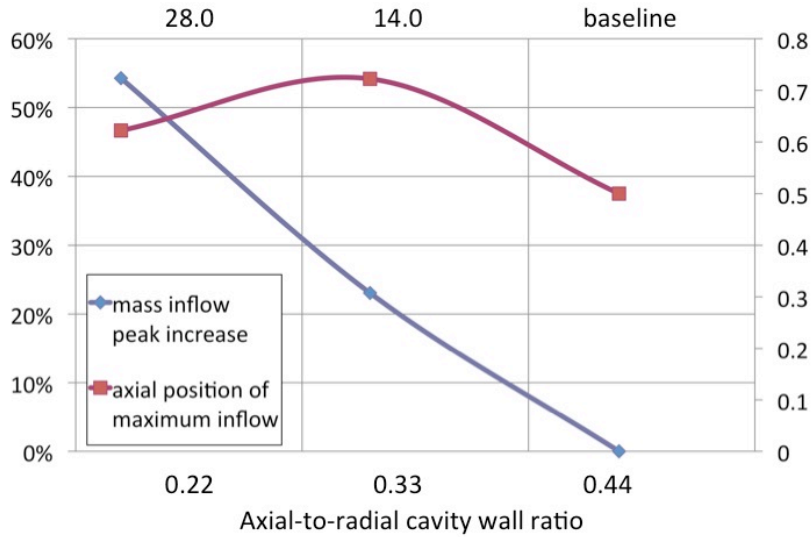

Figure 4.7: CFD predicted mass inflow peak increase relative to the baseline case, blue line, axis on the left, and non-dimensionalized axial position where the maximum inflow occurs, red line, axis on the right.

The interaction of these two vortices leads to the strengthening of the horseshoe vortex. On the other hand, a shortening of the available axial gap by 0.17c leads to a smaller mass flow egress. The vortex that resides in the lower half of the cavity handles only half the mass flow compared to the toroidal vortex of the baseline case. Therefore, less mass flow is being re-injected back into the main flow and with a swallow angle as the smaller vortex of the 14.0 case does not penetrate into the main flow. As a result, a weaker tip passage vortex will be formed. A further reduction of the available cavity's axial length completely eliminates the presence of the toroidal vortex, as already mentioned. Since the amount of mass flow that finally escapes through the labyrinth over the 2nd stage rotor remains the same, the absence of a vortex that would smoothly regulate the mass flow exchange at the interaction zone is now replaced by a strong jet that fills the cavity and subsequently exits from the cavity. The flow that exits the stator passage is redirected upwards once it is in front of the pressure side of the rotor blade. All the mass flow that was to enter the cavity mainly through the middle of the cavity's axial gap now enters the cavity, and fills the entire axial cavity

gap, as seen in Figure 4.8. The inflow region is now located circumferentially closer to the rotor blade, contrary to the circumferentially elongated and axially-centered inflow pattern. Thus it covers one-third of the stator pitch, as opposed to half for the baseline and 14.0 cases (Figure 4.8a, 4.8b). The outflow region has also been circumferentially moved towards the suction side of the stator blade. The inflow region occupies circumferentially less area and a stronger jet is thus formed. Fluid originating from the lower stator blade span positions is also trapped in this upward movement and is transported downstream to the rotor leading edge. The pressure side leg of the horseshoe vortex is re-enforced, as more mass flow becomes involved, because of this upward movement of the fluid.

In Figure 4.9, the tip passage vortex is visualized using secondary flow vectors on the exit plane downstream of the rotor exit. Although there is a relative resemblance between the baseline and 28.0 cases in terms of the position of the vortex core and its magnitude, the 14.0 case is substantially different. The vortex core in the 14.0 case is displaced upwards closer to both the casing and the suction side of the blade. A more energetic vortex at the rotor exit will tend to deviate more from the blade exit angle and expand in size, therefore enabling more mass flow into its circular motion (Figure 4.9a, 4.9c). The smaller magnitude of the tip passage vortex in the 14.0 case is also visualized in Figure 4.10 by the use of streamlines. Streamlines originating from 3 different span locations at rotor inlet (yellow at 99%, red at 95% and green at 90% of the blade span) clearly show the smaller vortex formed at the rotor exit for the 14.0 case compared to the baseline and 28.0 cases, Figure 4.10b. Moreover, the strong upward movement of fluid originally at lower span locations is especially evident for the 28.0 case shown in Figure 4.10c. As more mass flow is involved in the rotor tip passage vortex for the 28.0 case, a stronger and more energetic vortex forms that migrates towards the pressure side of the neighboring rotor blade as it convects through the rotor passage.

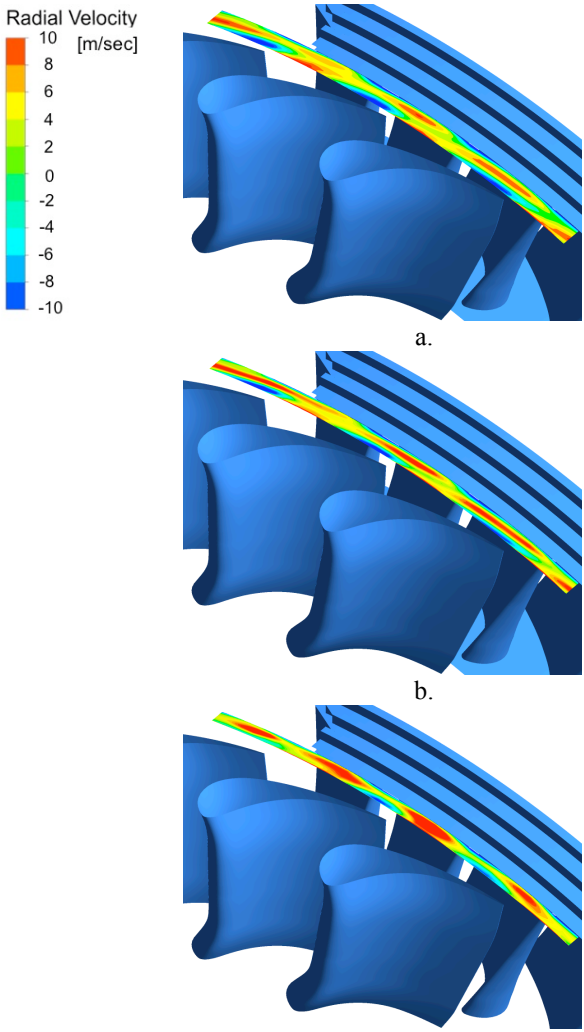

Figure 4.8: CFD predicted inflow and outflow at cavity entrance for (a) baseline case, (b) 14.0 case and (c) 28.0 case. The cavity inlet is colored to show the radial velocity. Red indicates fluid moving upwards into the cavity; blue indicates fluid that exits the cavity

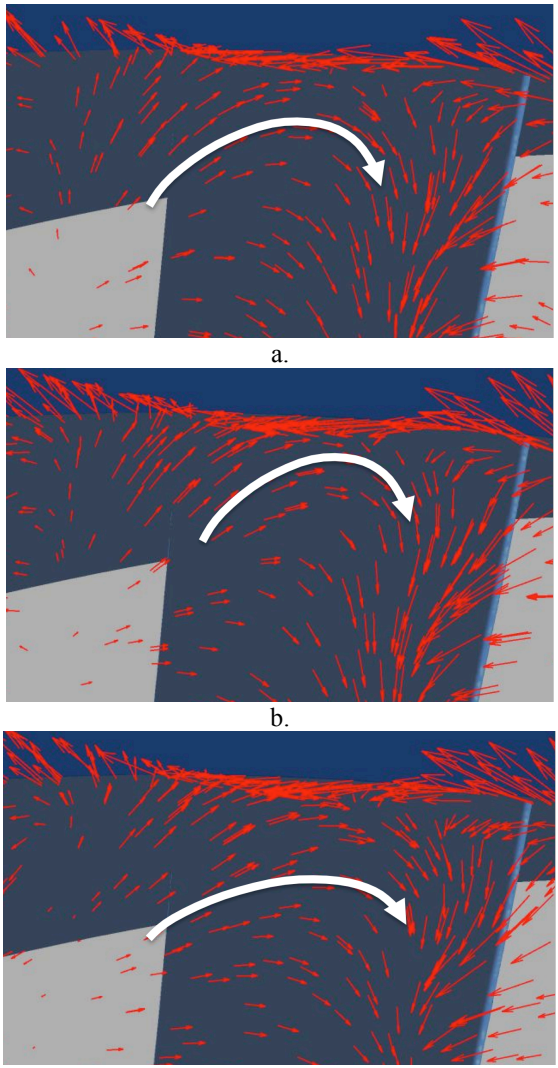

Figure 4.9: CFD predicted tip passage vortex at rotor exit as seen from a downstream location for (a) baseline case, (b) 14.0 case and (c) 28.0 case.

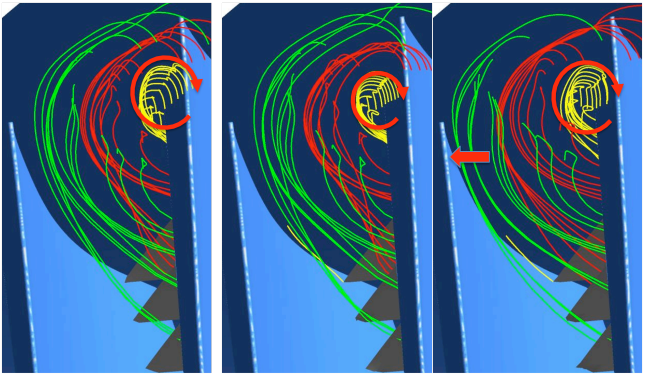

a. b. c.

Figure 4.10: CFD predicted tip passage vortex visualized with the use of streamlines at rotor exit for (a) baseline case, (b) 14.0 case and (c) 28.0 case. The streamlines originate from three planes at rotor inlet: yellow 99%, red 95% and green 90% of the blade span. Upstream view.

While the extension of the upper stator casing platform positively affects the flow field at stator exit, the simultaneous cavity volume reduction acts beneficially only as long as the vortex still forms inside the cavity. Moreover, the flow field at the interaction zone greatly influences the formation of the rotor tip passage vortex, which is fed by fluid originating from the interaction zone. A large cavity vortex that extends beyond the limits of the cavity into the main flow for the baseline case, as well as the formation of jets because of the insufficient axial gap to form a vortex in the 28.0 case, lead to larger tip passage vortices and thus also lead to a work extraction deficit over the rotor. Overall, the rotor inlet cavity volume and its axial inlet length have a profound impact on efficiency through their influence on the path of the cavity flows and therefore the mixing procedure at the interaction zone. The cavity volume and length scale should allow for a beneficial cavity vortex to be formed that continually regulates the in and outflows. A rectangular cavity shape that initiates the break-up of an initial larger vortex into two smaller vortices leads to efficiency gains through decreased mass flux oscillations at the interaction zone and smoother re-injection angles. An axial to radial cavity wall length ratio of 0.33 was proved here to support the presence of two smaller vortices. Nevertheless, since the vortex size is related to its frequency,

a designer should carefully couple the cavity size with the stator exit velocity, which is the vortex driving mechanism.

4.2 Radial Cavity Wall Length Reduction

The experimentally measured stage efficiency for the cases considered is shown in Figure 4.11. For the cases with radial wall length reduction there was an increase in efficiency of 1.1% for the 14.1 case and 1.6% for the 28.1 case compared to the baseline case.

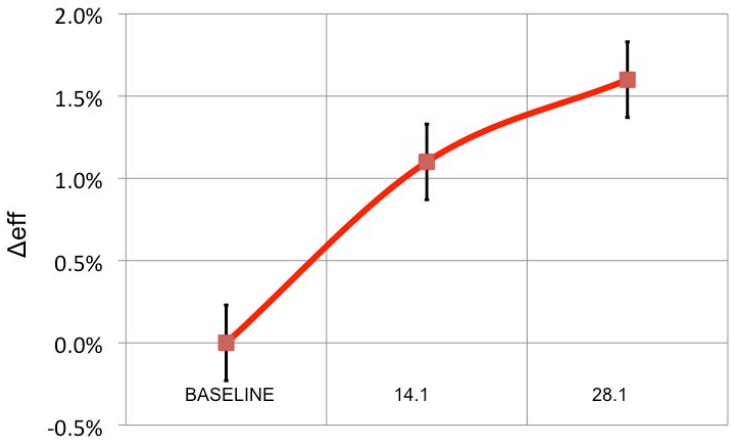

Figure 4.11: Δeff for the cases with radial cavity wall length reduction. The baseline case is used as a reference for the cases presented.

The experimentally measured pitchwise mass-averaged flow pitch angle is shown in Figure 4.12 for the baseline case and the two cases with radial wall length reduction. No measurable differences are identified in the main flow below 95% of the blade span. For the upper 5% of the blade span the pitch angle shows smaller values with the decrease in the radial wall length along with the cavity volume. Less fluid moving upwards towards the cavity inlet area signifies less mixing at the interaction zone. Inside the cavity the trend followed by the cases shown in Figure 4.12 is similar.

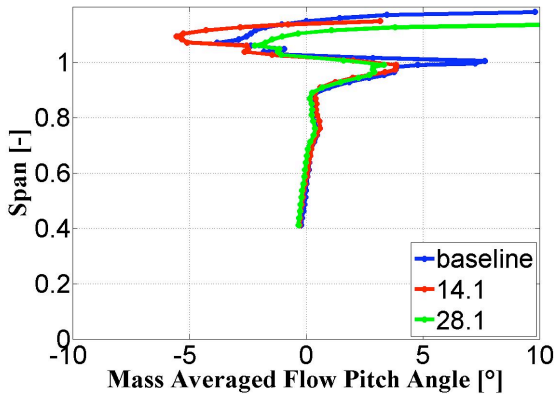

Figure 4.12: Experimentally measured pitchwise mass-averaged flow pitch angle (a) for the baseline case, 14.1 and 28.1 cases and (b) for the cases with a cavity volume of 14% and 28%. Stator exit

The experimentally measured pitchwise mass-averaged relative flow yaw angle at rotor exit is shown in Figure 4.13 for the baseline case, and the 14.1 and 28.1 cases. The radial wall length reduction influences the rotor tip passage vortex formation, which is partially facilitated by fluid exiting the inlet cavity. Between h=0.65 and h=0.8 case 14.1 exhibits a smaller sized tip passage vortex.

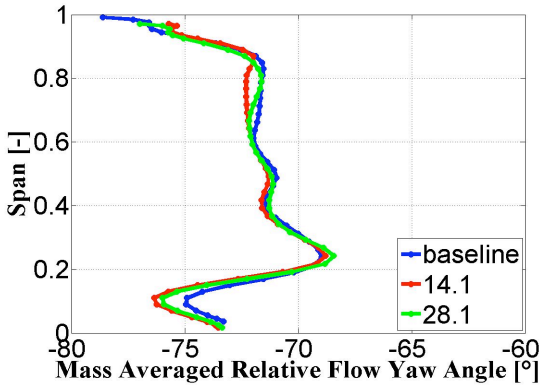

Figure 4.13: Experimentally measured pitchwise mass-averaged relative flow yaw angle for the baseline case, and cases 14.1 and 28.1. Rotor exit

In Figure 4.14, the computed radial velocity distribution is plotted on a meridional plane at the exit of the stator and for h=0.95 till h=1.18, for the baseline case and cases 14.1 and 28.1. The red color indicates upward fluid movement. The right hand side plots are for a time instant and during inflow to the cavity whereas on the left during outflow. Secondary flow vectors are projected onto the plane. White lines denote the flow path. The cavity volume reduction through the radial cavity wall shortening mainly affects the formation and positioning of the cavity vortex. The corresponding ratio of axial to radial wall length, presented in Table 4.2, has a direct impact on the vortex formation. The ellipsoidal vortex of the baseline case with a ratio of axial to radial wall length of 0.66 showed a more circular shape when the ratio increased to 0.77 and to 0.9 for the 14.1 and 28.1 cases respectively.

Case	Baseline	14.1	28.1
a/b	0.66	0.77	0.9
Leakage flow [%]	0	2.5	-1.6

Table 4.2 Ratio of axial to radial cavity wall length a/b and leakage flow that escapes through the labyrinth expressed as a percentage. The leakage flow of the baseline case is used as a reference

Between the cases with reduced cavity volume the increase of the a/b ratio only influenced the vortex position rather than the shape. The lowering of the upper axial wall by 13% and 25% respectively for the 14.1 and 28.1 cases, eliminated the fluid that used to drift between the cavity vortex and the upper axial wall leading to extra losses. Additionally, the lowering of the center of the vortex for the 28.1 case offered a comparative advantage over the other two cases. Flow entering the cavity needs to be re-directed from the streamwise to the radial direction, thus reducing the potential work extraction and enhancing the mixing at the interaction zone. The lowering of the vortex's center for the 28.1 case brought the lower side of the vortex closer to the interaction zone. The mass flow entering the cavity became involved in the cavity vortex without a prior need to be radially transported. Therefore, the 28.1 case generated an even greater efficiency increase compared to the 14.1 case. In both the cases of the baseline and 14.1 the bigger cavity volume compared to the 28.1 allows the cavity vortex to expand in size. Once the upward moving jet passes over the shroud is leaned towards the downstream radial cavity wall, pushed also by the jet exiting the cavity. The counter-rotating vortex that lies under the leaned jet and over the shroud is confined in terms of space during outflow. The decreased volume pushes the flow to pass through the gap over to the first closed cavity introducing thus greater leakage flow for the baseline and 14.1 cases, shown in Table 4.2. In Table 4.2 the leakage flow is expressed as a percentage of change relative to the leakage flow of the baseline case.

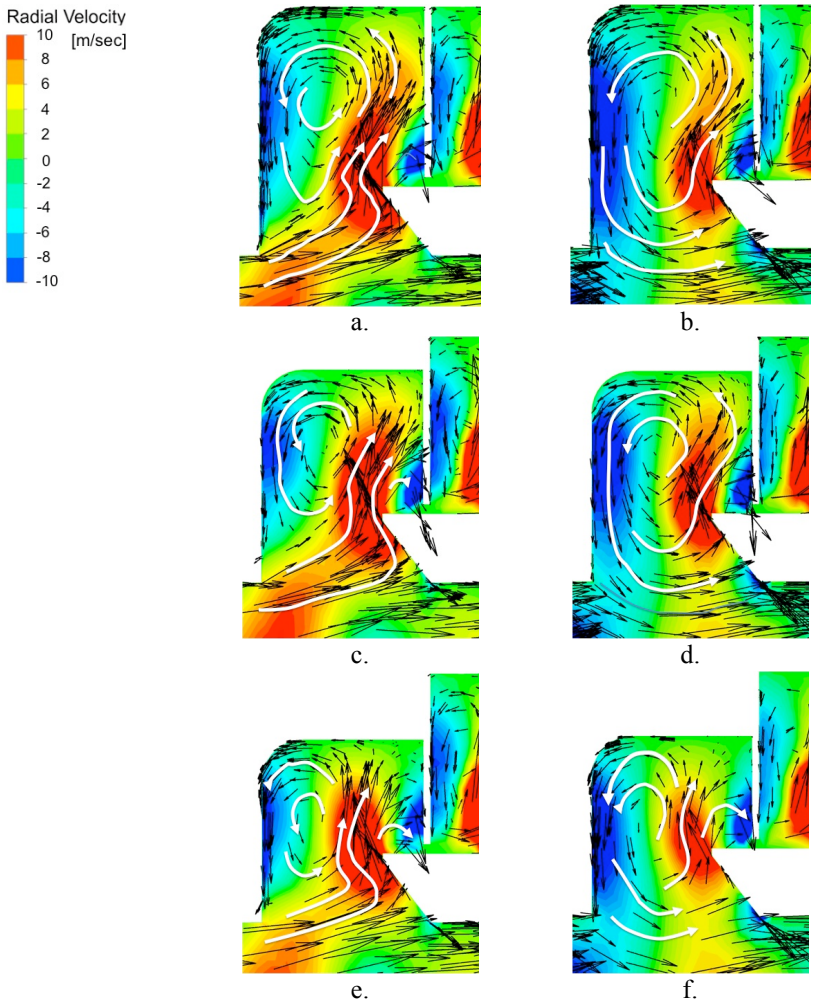

Figure 4.14: CFD computed results of the inflow to the cavity for the (a) baseline case, (c) 14.1 and (e) 28.1 cases and for the outflow (b), (d) and (f). The simulations show a meridional cut at the exit of the stator and for h=0.95 till h=1.18. The planes are colored with radial velocity and the secondary flow vectors are projected onto them. The flow path is denoted by white lines.

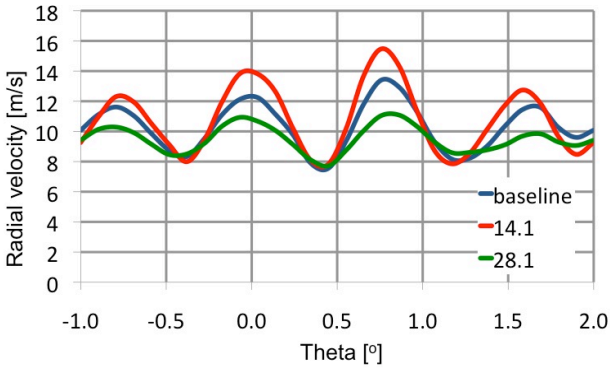

a.

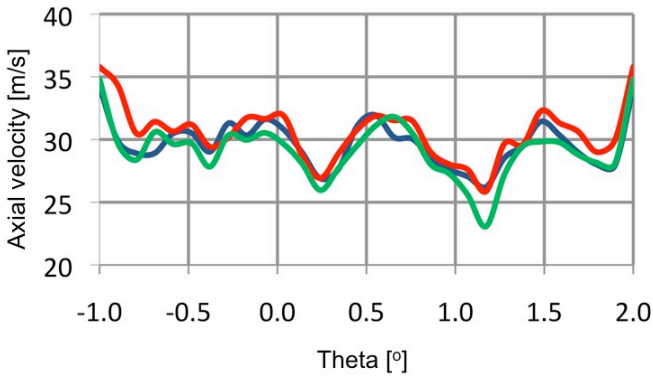

b.

Figure 4.15: CFD computed (a) mean radial velocity over the axial distance c=0.5 to c=0.8 at h=1.07 and (b) mean axial velocity over the radial distance between first fin and shroud and for 3 stator pitches.

In Figure 4.15a the radial velocity over the axial distance from c=0.5 to c=0.8 at h=1.07 is presented. This represents the axial distance where the radial jet entering the cavity is located. The mass flow contained in the jet originates from the stator pressure side nevertheless its path is dictated by the rotor potential flowfield. This becomes evident by the four peaks in the radial velocity distribution distanced 7.5^{o} apart. The peak values of the radial jet are

smaller by 20% and 40% when compared with the baseline and 14.1 cases. The smaller and lower located vortex of the 28.1 case does not allow the radial jet to increase its radial velocity as the later is immediately enabled in the cavity vortex. A stronger jet leads to potentially higher losses due to mixing. On the other hand, the increased volume of the cavity for the baseline and 14.1 cases results in the jet being leaned over to the downstream radial cavity wall. The leakage mass flow quantified in Table 4.2 can be graphically explained by the plot on Figure 4.15b. The mass flux over 30° is plotted radially summed over the gap size. Both cases, the baseline and the 14.1 meet higher leakage mass flow compared to the 28.1 case

4.3 Swirl Brakers

The use of swirl brakers deteriorated efficiency by 0.3% compared to the baseline case. The mass-averaged total pressure coefficient at the stator exit for the baseline and the swirl brakers cases is presented in Figure 4.16. the flow field is identical up to 85 percent span. At the upper 15 percent extensive losses are present for the swirl braker case.

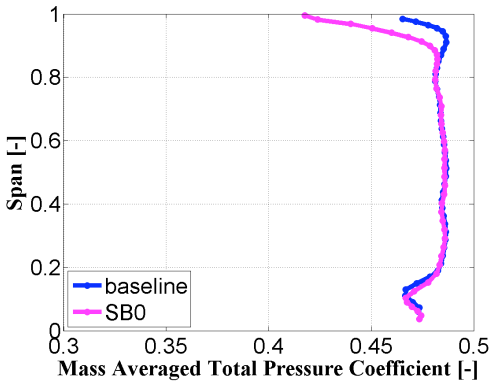

Figure 4.16: Experimentally measured pitchwise mass-averaged total pressure coefficient for the cases baseline and swirl brakers circumferentially aligned with the stator trailing edge. Stator exit

The time-averaged 2D plot at stator exit for the two cases examined is shown in Figure 4.17. In the baseline case the fluid moves upwards till h=1

and then gets re-directed clockwise to feed the low-pressure fluid of the wake of the adjacent blade. On the other hand, the use of the swirl brakers, Figure 4.17b creates a strong leakage jet (red area) in the pressure side of the stator blade that extends to half a pitch in the circumferential direction and down to 80 percent of the blade span. It is apparent that a strong jet also exits the cavity on an adjacent plane.

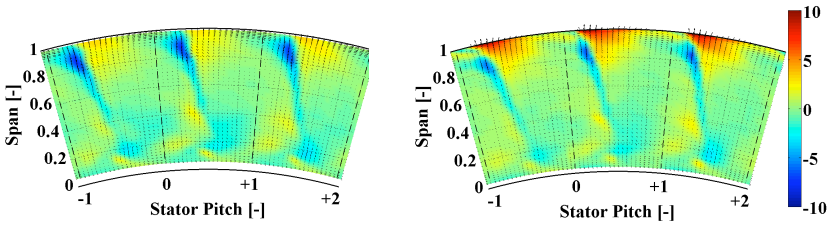

a. b.

Figure 4.17: Experimentally measured 2D radial velocity plot at stator exit for the cases (a) baseline and (b) swirl braker

The mass fluxes at h=0.975 for the two cases are shown in Figure 4.18a. the mass flux of the swirl braker case is overall higher with the peak values showing even 100 percent increase. Fluid inside the cavity moves in the circumferential direction till it is stopped by the swirl braker on the pressure side of the swirl braker. The fluid is re-directed back into the main flow generating extra losses. On the suction side of the swirl braker inside the cavity there is a recirculation bubble generating reverse flow into the cavity. Due to higher losses on the tip region caused by the blockage and recirculation of fluid imposed by the swirl brakers the efficiency of the swirl braker case is lower. Especially on the operating point the turbine experienced a drop of 0.3 percent in efficiency.

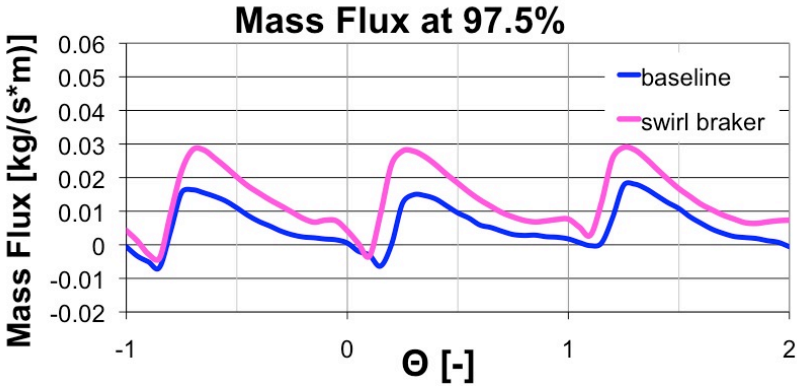

a.

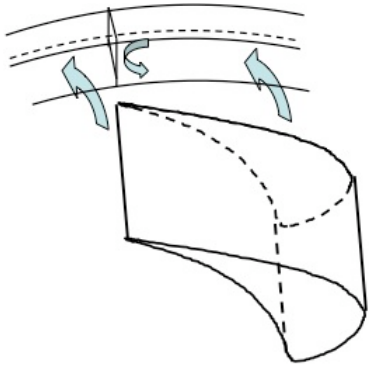

b.

Figure 4.18: (a) Mass flux at h=0.975 for the two cases and (b) proposed flow

The flow field for the two cases at rotor exit is presented in Figure 4.19. A large underturning is present for the swirl braker case from 0.7 – 0.9 span, the region where the tip passage vortex develops. On the other hand, the pitch angle variation shows a uniform radial distribution of the swirl braker case from 0.6 – 0.95 span height indicating a reduced interaction with the cavity flow.

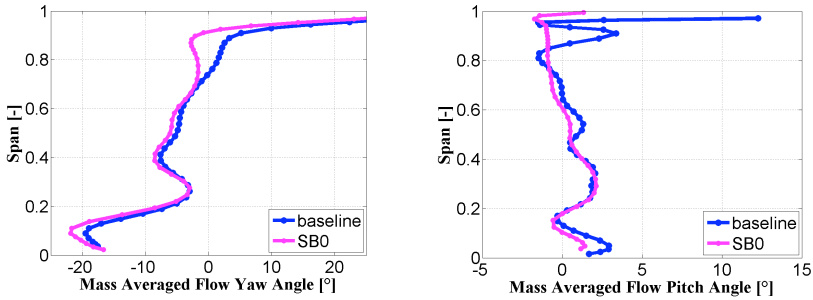

a. b.

Figure 4.19: Experimentally measured mass-averaged flow (a) yaw and (b) pitch angles at rotor exit for the cases baseline and swirl brakers

Summary

The mixing process occurring at the interaction zone between the cavity and main flows has been examined. In the first part a series of experiments has been carried out to investigate the influence of three different rotor inlet cavity volumes along with an extension of the upper casing stator platform on stage efficiency. Experimental results were supported by computational analysis.

The initial cavity volume of the baseline case was reduced by 14% and 28%. This was achieved by a uniform extension of the upper stator casing platform by 17% and 34% of the initial axial cavity length. The extension of the stator casing allows for a greater overturning of the flow before the cavity entrance is reached and the flow turns in a circumferential direction. The smaller the jump experienced by the flow, the smaller the losses in the tip section at the exit of the stator blade. Inside the cavity, the decrease of the axial cavity's length impacts on the flow kinematics and the formation of the vortex itself.

A 14% cavity volume reduction results in the break-up of the single vortex during inflow into two smaller vortices during outflow, as compared to the presence of the single vortex at all times for the baseline case. The smaller vortex in the lower half of the 14% CVR case causes less mixing at the interaction zone as it circulates less fluid. Furthermore, it improves the re-entry of the flow that takes place at a smoother angle, as the vortex does not penetrate into the main flow. Thus, it does not support the pressure side leg of the rotor horseshoe vortex at its onset as much as in the baseline case. A further reduction of the cavity volume completely changes the behavior of the cavity flows, which are characterized by the absence of any toroidal vortex and which are now replaced by strong in and outflow jets. Greater mixing due to the strong jets as well as a larger rotor tip passage vortex, facilitated by the strong in and out flow, are present. While the impact on stage efficiency is positive and an increase of 0.33% is observed compared to the baseline case for the 14% CVR, the further reduction leads to an efficiency deficit of almost 0.2% relative to the baseline case.

This study suggests that the reduction of the rotor inlet cavity volume through the extension of the stator casing platform acts beneficially on stage efficiency till the point when the toroidal vortex of the cavity breaks down due to a lack of the necessary axial distance that allows the latter to form.

On the second part three more rotor inlet cavity configurations were investigated in terms of their impact on stage efficiency. Cavity volume was

decreased again by 14% and 28% compared to the initial baseline cavity volume through radial cavity wall length reduction.

The radial wall length reduction that led to 14% and 28% cavity volume reduction increased the efficiency. An efficiency increase of 1.1 percent was experimentally measured for the 14% CVR case compared to the baseline case. The additional wall length shortening offered even greater increased efficiency of 1.6 percent compared to the baseline case. Apart from introducing a square-shaped cavity and thus a cavity vortex of the same shape, the lowering of the center of the vortex towards the interaction zone acts beneficially for cases 14.1 and 28.1. The closer the vortex is to the cavity inlet, the less the fluid entering the cavity has to be radially transported, thus reducing the potential work extraction.

This study suggests that a square-shaped cavity performs better than a rectangular cavity. Cavity design plays a key role in the cavity vortex formation and positioning. The lower side of the cavity vortex should be close to the interaction zone. This study would therefore suggest that cavity design should push the vortex to be even lower, but not extending beyond the cavity limit.

The use of swirl brakers to break down the toroidal vortex inside the cavity deteriorated the efficiency by 0.3 percent. The swirl braker created a barrier that braked the cavity flow and re-directed it towards the main flow causing extensive mixing on the upper 15-20 percent of the blade span.

5. Impact of Cavity Geometry on Efficiency

5.1 Axial vs. Radial Cavity Wall Length Reduction

In this chapter the cases examined are divided into two groups. In each group the cavity volume is kept the same so as to exclude any influence on the leakage mass flow. In the first group the cases 14.0, 14.1 and 14.2 are examined with 14% CVR compared to the initial baseline case whereas in the second group with 28% CVR the cases examined are 28.0, 28.1 and 28.2. The experimentally measured stage efficiency for the cases considered in this study is shown in Figure 5.1. Overall the radial wall length reduction compared to the axial one performs better for both the cases of 14% CVR and 28% CVR. For the cases 14.2 and 28.2, the use of the additional curvature between the upper axial cavity wall and the downstream radial wall does not act beneficially. It offers 0.15% efficiency gain for the 14.2 case compared to the 14.1 case and an efficiency drop of 0.7% for 28.2 case compared to the 28.1 case.

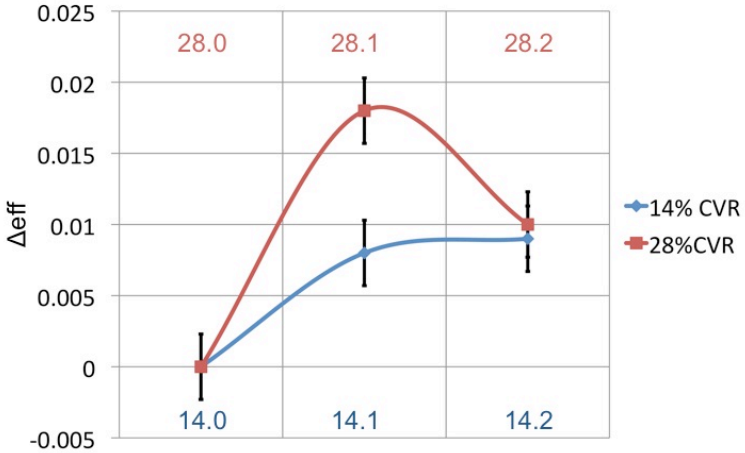

Figure 5.1: Δeff for the cases examined in this study. The cases 14.0 and 28.0 are used as references for the cases with the same CVR

The experimentally measured pitchwise mass-averaged total pressure loss coefficient is shown in Figure 5.2a for the cases with 14% cavity volume reduction and in Figure 5.2b for the cases with 28% cavity volume reduction. No measurable differences are identified in the main flow for the cases with 14%CVR. The stator casing platform extension of the 14.0 case does not influence the formation of the boundary layer on the casing. Inside the cavity the axial cavity wall length reduction leads to lower pressure inside the cavity, which potentially decreases the leakage mass flow through the labyrinth. The comparison between the cases with 28% CVR shows an area of lower loss being generated at the tip section of the blade in the region of the casing's boundary layer. The extension of the stator casing platform acts beneficially.

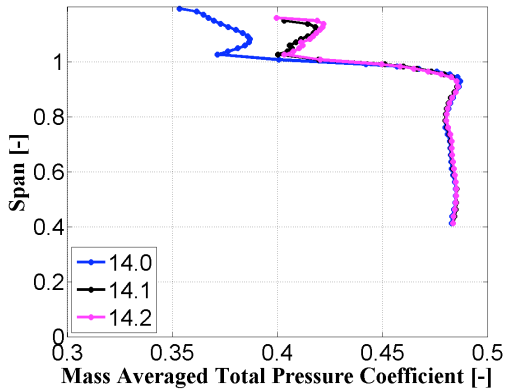

a.

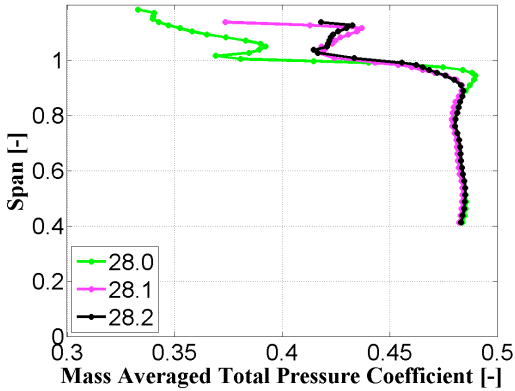

b.

Figure 5.2: Experimentally measured pitchwise mass-averaged total pressure coefficient for the cases with 14% CVR (a) and the cases with 28% CVR (b). Stator exit

The experimentally measured pitchwise mass-averaged relative flow yaw angle is shown in Figure 5.3a for the cases with 14% cavity volume reduction and in Figure 5.3b for the cases with 28% cavity volume reduction. For the cases with 14% CVR contrary to the resemblance of the 14.0 and 14.2 cases, the 14.1 case exhibits a smaller tip passage vortex. The straight black line

from 0.6 to 0.85 of the span coincides with the designed metal exit angle of the rotor blade. Also for the 28% CVR cases there is a resemblance for the case 28.0 and 28.2 with the 28.1 being different. The tip passage vortex in the 28.1 case is located at a lower span position compared to the 28.0 and 28.2 cases. This causes also some disturbance in the flow underneath at 0.4 span.

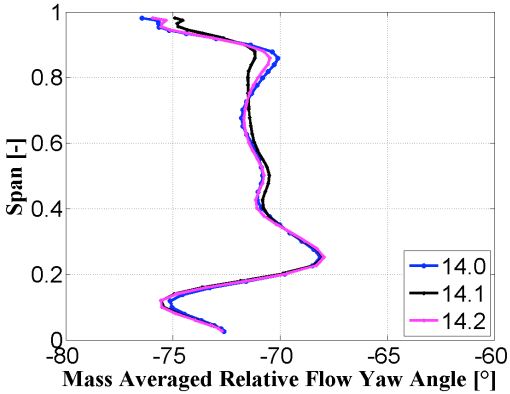

a.

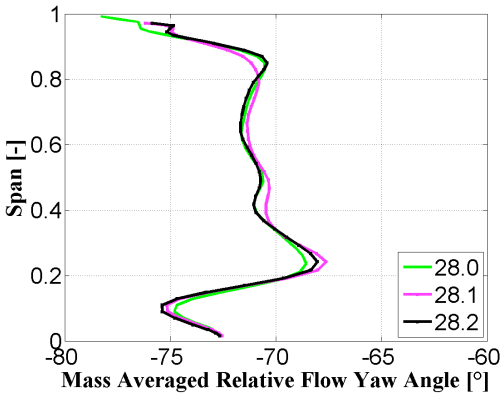

b.

Figure 5.3: Experimentally measured pitchwise mass-averaged relative flow yaw angle for the cases with 14% CVR (a) and the cases with 28% CVR (b). Rotor exit

In Figure 5.4 the computed radial velocity distribution is plotted on a meridional plane at the exit of the stator and for h=0.95 till h=1.18, for all cases examined in this study. Red colour indicates upward fluid movement. The plot is for a time instant and during inflow to the cavity. In Figures 5.4a, 5.4b and 5.4c the 14% CVR cases are presented whereas, in Figures 5.4d, 5.4e and 5.4f the 28% CVR cases. Secondary flow vectors are projected onto the plane. White lines denote the flow path.

Case	14.0	14.1/14.2	28.0	28.1/28.2
a/b	0.55	0.77	0.44	0.9

Table 5.1: Ratio of cavity's axial to radial wall length

Great differences are present between the cases of axial and radial CVR for the same volume. The ratio of axial to radial wall length, presented at Table 5.1 has a direct impact on the vortex formation inside the cavity. The vortex formed in the 14.0 case has an ellipsoidal shape owed to the ratio of the cavity walls' length. The rectangular cavity shape with a ratio of axial to radial wall length of 0.55 stretches the vortex in the radial direction. On the contrary the radial wall length reduction of the cases 14.1 and 14.2 leads to the formation of a more circular vortex with its centre located at a lower radial position compared to the 14.0 case. The radial wall length reduction offers an efficiency improvement. The upper 15% of the cavity was dominated by the counter-rotating vortex and fluid residing between the main cavity vortex and the wall. The lowering of the upper axial wall by 14% of the 14.1 case eliminated the fluid that used to drift between the cavity vortex and the upper axial wall leading to extra losses.

Even greater differences in efficiency are measured for the 28% CVR group between the cases examined. The difference in the ratio of axial to radial cavity wall is apparent when comparing the 28.0 with a/b=0.44 with the 28.1 that has an a/b=0.9. The almost square cavity shape provided an efficiency increase of 1.8% relative to the rectangular shape of 28.0. As it has been extensively presented and discussed by Barmpalias et al. [6] the ratio of a/b=0.44 eliminate the presence of the cavity vortex that continuously and smoothly regulated the in and out flows and strong radial jets dominated the cavity flow. These jets penetrate the main flow, abruptly redirect the flow from axial to radial direction and cause extensive mixing at the interaction zone. On the contrary, the almost square cavity of the 28.1 case provides a great efficiency advantage. The drifting mass flow between the cavity vortex and the wall is not present as well. The vortex core has now migrated at a

lower span position extending though still within the cavity area. The lower end of the cavity vortex during outflow reaches the interaction zone. The fluid that exits the inlet cavity is already orientated in the axial direction and a smooth re-entry angle is achieved. On the other hand, the rectangular cavity shape demands for a radial transport of the fluid inside the cavity, since the cavity vortex is stretched and at higher span location. In such a case the fluid will intersect with the main flow and will be abruptly re-directed to the axial direction being a major source of loss generation.

The flow path inside the cavity plays a key role inside the cavity. Nevertheless, it is of great importance the path of the mass flow that is to enter the cavity. The flow that exits the stator blade passage and is within the upper 10% of the blade span is prompt to enter the cavity or interact with the cavity flows. In Figure 5.5 a streamline that exits the stator and enters the cavity. The control volume presented in the Figure 5.5 is bordered by the axial planes located at c=0 and c=1. For the cases 14.0 and 28.0 the upstream axial plane is taken on c=0.17 and c=0.34, respectively. The inner surface was chosen to be at h=0.9. At this radial location the area integration delivers a net radial mass flow of approximately 0. The outer surface is at h=1.0, the interaction zone between the cavity and main flows. The local pressure gradient across this control volume is not sufficient enough to keep the flow at a constant radius. Streamlines originating from the stator side enter the cavity. Three are the driving mechanisms that bent the streamline upwards and inside the cavity. The radial pressure gradient between the two radial locations, the sudden area increase due to the cavity and the sucking of the leakage mass flow.

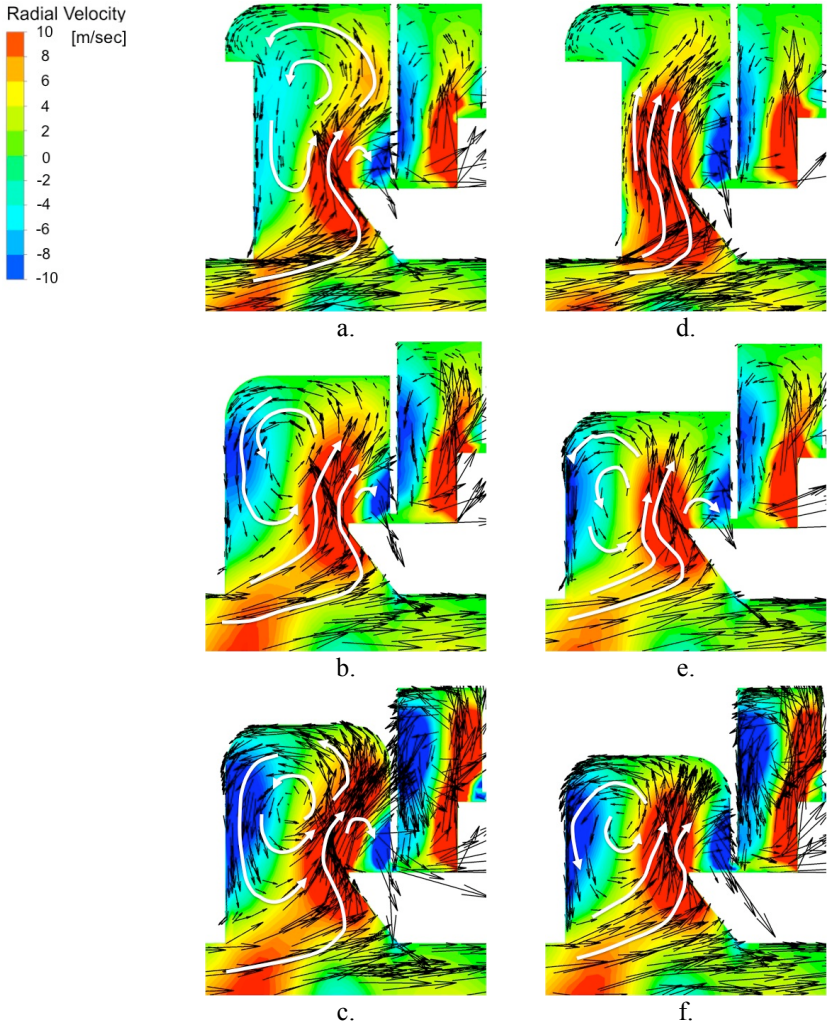

Figure 5.4: CFD computed results of the inflow for the cases (a) 14.0, (b) 14.1, (c) 14.2, (d) 28.0, (e) 28.1, and (f) 28.2. The simulations show a meridional cut. The planes are colored with radial velocity and the secondary flow vectors are projected onto them. The flow path is denoted by white lines.

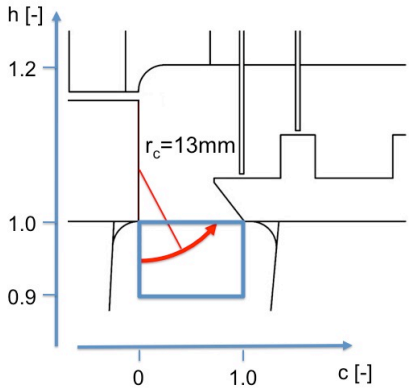

Figure 5.5: Streamline curvature of the mean streamline that enters the control volume bordered axially by planes at cavity inlet and exit and radially at h=1 and h=0.9.

For the case under study the radial equilibrium can be simplified to

$$\frac{v_z^2}{r_z} - \frac{v_\theta^2}{r} = -\frac{1}{\rho}\frac{\partial p}{\partial r} + \frac{F_r}{\rho V_{ConV}} \tag{5.1}$$

assuming that the mean streamline enters the control volume axially. Using CFD computed values over the control volume a representative streamline with an average meridian radius of r_c=13mm is calculated for all cases examined. For the cases with radial wall length shortening, the streamline enters the cavity at c=0.8. This coincides with the CFD results of Figure 5.4 where most of the inflow to the cavity takes place from c=0.8 to c=1.0. For the cases with axial wall length reduction, as the streamline curvature remains unaltered the main inflow region is moved to a more downstream position. The same streamline now impinges on the inclined surface of the shroud and gets abruptly redirected from the axial direction radially upwards, forming a strong jet. Even though, the overall mass flow leaking though the labyrinth remains the same for all cases examined, the stronger jet formed at the cases 14.0 and 28.0 leads to greater mixing at the interaction zone generating therefore more losses.

In Figure 5.6 the radial sum mass flux at the cavity inlet from c=0.85 to c=1.0 is plotted where most of the inflow takes place. The mass flux is axially summed over the last 15% of the cavity inlet. As seen in Figure 5.6 the peak values for the 14.0 case are increased up to 60% and 66% compared to the 14.1 and 14.2 cases, respectively. The formation of the strong jet in the 14.0 case in the last 15% of the cavity inlet leads to the increased mixing through abrupt fluid flow re-direction, causing efficiency deficits compared to the 14.1 and 14.2 cases. In Figure 5.6b the radial sum mass flux at the last 15% of the cavity inlet is presented for the cases with 28% cavity volume reduction.

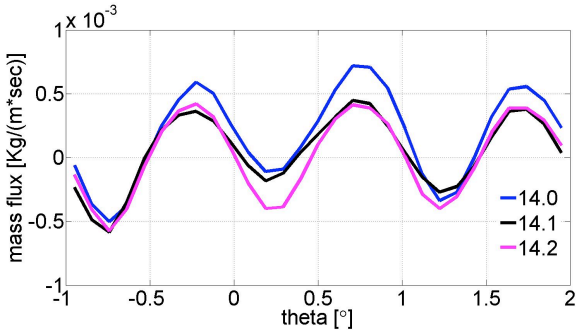

a.

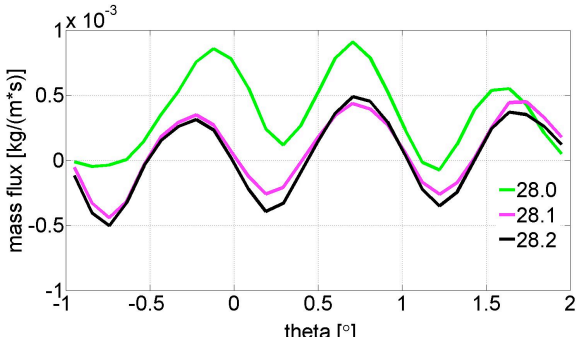

b.

Figure 5.6: Computed (steady CFD) mass flux at cavity inlet from c=0.85 till c=1. Data are axially summed

Among the cases with 28% cavity volume reduction the 28.0 meets an increase in peak values of 100% compared to the 28.1 and 28.2 cases. This leads to a considerable increase in the mixing and in the flow disturbance and impacts negatively on efficiency for the 28.0 case.

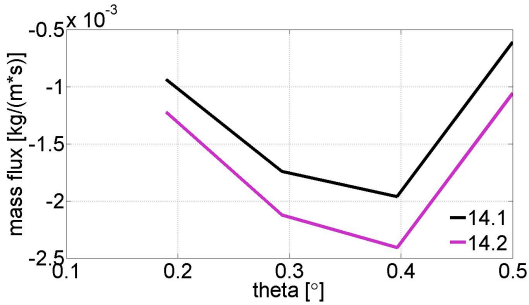

Figure 5.7: Mass flux of the cases 14.1 and 14.2 summed over from c=0 till c=0.17 at the circumferential location where the outflow from the cavity takes place.

The curvature introduced between the upper axial wall and the downstream radial wall at the 14.2 and 28.2 cases intensifies the vortex of the cavity. Although designed to eliminate the counter-rotating vortex of the upper right corner of the cavity and assist the flow re-direction from radial to axial direction it does not act beneficially. The mass flow initially trapped into the counter-rotating vortex is now circulating into the main vortex of the cavity. Therefore, more mass flow is exchanged in the interaction zone between the cavity and main flows. Greater mixing will take place. In Figure 13 the mass flux from c=0 till c=0.17, axially averaged is plotted for the cases 14.1 and 14.2 during the outflow from the cavity. The peak values of the outflow for the case 14.2 are increased by 25% compared to the 14.1 case. This is owed to the mass flow that is re-directed axially upstream and then radially downwards because of the rounding of the upper right corner of the cavity. The situation is identical between the 28.1 and 28.2 cases.

As already shown the curvature introduced at the upper right cavity corner increases the mass flow that is re-directed towards the main cavity vortex. The flow that enters the cavity once it reaches the upper axial wall will be re-directed left or right (Figure 5.8a). A percentage of the mass flow that initially enters the cavity is redirected left to the main cavity vortex. This mass

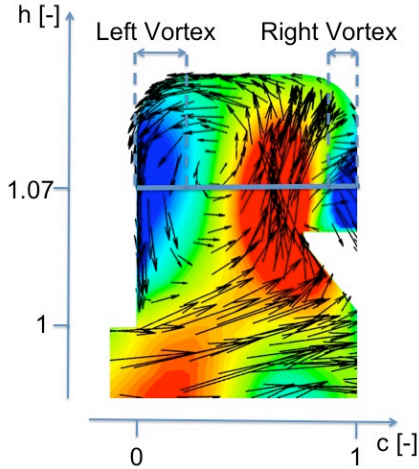

a.

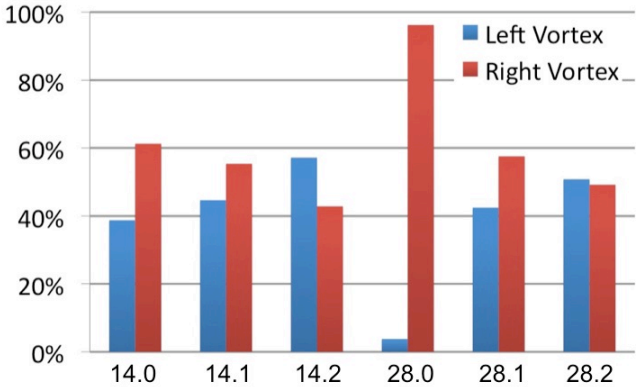

b.

Figure 5.8: Distribution of the flow between the left and the right vortex on a z-θ plane at the radial height of h=1.07.

flow will later interact with the main flow at the interaction zone. The remaining mass flow turns right to feed the counter-rotating vortex. Part of the mass flow of the counter-rotating vortex will escape through the cavity over the rotor. The left and right vortexes are shown in Figure 5.8a. The graph of

Figure 5.8b presents the percentage of the flow that follows the left or the right vortex. The data were taken from a z-θ plane at h=1.07, shown in Figure 5.8a. The rounding of the upper corner of the 14.2 and 28.2 cases redirects 13% and 8% more flow to the left vortex compared to 14.1 and 28.1 cases respectively. The high percentage of the right vortex for the 28.0 case is owed to the fact that the toroidal cavity vortex has given its place to strong radially moving jets that wash in and out the cavity, Barmpalias et al. [6]

Summary

This paper examines the impact of the mixing process occurring at the interaction zone between the cavity and main flows. A series of experiments has been carried out to investigate the influence of six different rotor inlet cavity designs that modify the cavity volume along with the length scale on efficiency. Experimental results were supported by computational analysis. The initial cavity volume of the baseline case was reduced by 14% and 28%. This was achieved by extending either the upper casing stator platform or through a radial wall length reduction.

In both groups of 14% and 28% the cases with radial wall length reduction performed better. The radial wall length reduction in the 14% case had an efficiency gain of 0.85%. Following the same trend, the radial wall length reduction in the 28%, namely the 28.1 case showed an efficiency benefit of 1.7% compared to the 28.0 case that served as a baseline case. Nevertheless this is owed to the presence of the strong radial jets that replaced the cavity vortex, causing extra losses in the 28.0 case.

The additional curvature introduced in the upper right corner of the cavity increased the efficiency by 0.15% in the 14% CVR group, which is within the efficiency accuracy measurement of the test facility. In the case of the 28% CVR group the efficiency was decreased by 0.7% owed to the increased mass flow that was circulated by the cavity vortex and interacted with the main flow. The additional mass flow originated by the mass flow that was trapped in the counter-rotating vortex of the upper right corner.

This study suggests that the square shaped cavity performs better compared to the rectangular cavity. Additionally, the presence of corners inside the cavity is beneficial, as the mass flow trapped does not interact with the main flow. Nevertheless, the turbine designer has to account for all reasons responsible for creating losses and balance them against each other.

5.2 Effect of 3D-shaped Inlet Cavity Geometry on Efficiency

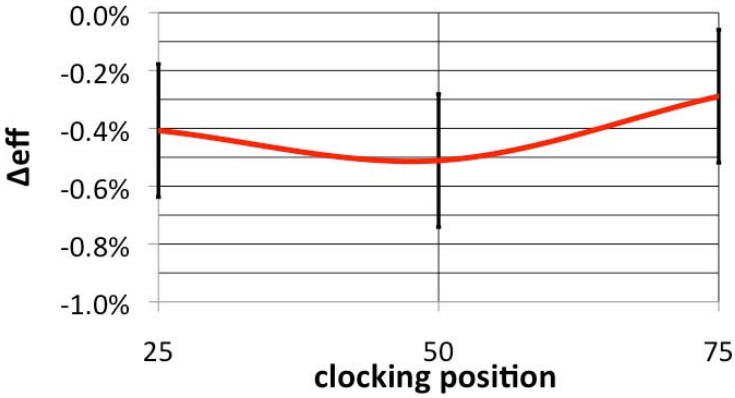

a.

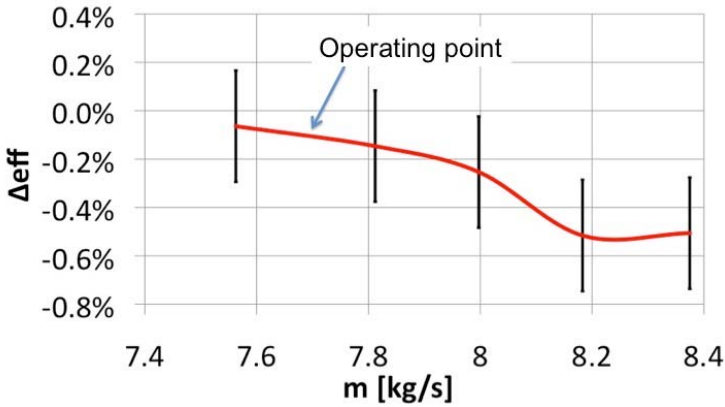

b.

Figure 5.9: Total to static efficiency changes between the cases with cavity volume reduction of
(a) 14% $Eff_{non-uniform}$ design B $- Eff_{14.0}$ **(b) 28%** $Eff_{slanted} - Eff_{28.0}$

Five cases are examined divided into two groups. Two non-uniform designs are compared against the 14.0 case that serves as a baseline. In the second group the slanted case is examined against the 28.0 case. The experimentally measured stage efficiency for the cases considered in this study is shown in Figure 5.9. The relative efficiency between the cases is presented. For the cases with 14% cavity volume reduction (14.0 and non-uniform) the improved design B relative to the 14.0 case experiences an efficiency drop. The worst circumferential clocking position is at 50% with 0.5% efficiency drop and the best circumferential position is the 75% with 0.3% efficiency drop. In Figure 5.9b the relative efficiency between the cases 28.0 and slanted vs. the turbine mass flow is presented. The comparison between the two cases with 28% cavity volume reduction shows a marginal efficiency gain of 0.1% at the operating point of the 28.0 case relative to the slanted case.

5.2.1 Cavity Volume Reduction of 14%

Initially the cases where the use of cavity inserts leads to a 14% cavity volume reduction compared to the baseline case are considered. Figures 2.6a and 2.9a show a schematic of these cases. In Figure 5.10a the time-averaged total pressure loss coefficient is presented for the first design of the non-uniform ring circumferentially clocked at 25% and 50% of the stator pitch together with the 14.0 case at the second stator exit. Measurements were made up to 85% of the blade span due to probe access restrictions. The plot covers 30° and three stator pitches. Dashed lines represent the upstream stator's trailing edge. The extensive losses in the vicinity of the blade's tip area are clearly identified for both the cases that the non-uniform ring is used. In particular in the case when the ring is circumferentially clocked at 25% of the stator's pitch, losses cover the last 10% of the span. Losses on the tip area of the 50% clocking position appeared to be considerably less though covering the 95% - 100% of the blade span. As the bump has circumferentially positioned itself towards the pressure side of the blade it is now located above the high pressure fluid. Therefore it prevents the latter from entering the cavity. Flow improves dramatically when the stator casing platform is uniformly extended (14.0). The use of the non-uniform ring pushes down radially the position of the upper passage vortex compared to the uniform case. This displacement of the vortex away from the casing is itself loss generating. The upper passage vortex expands and more mass is now involved in the circular motion. Additionally, for the 25% clocking position a downward flow movement can

be identified directly above the upper passage vortex, as shown in Figure 5.10b. It is fed by fluid exiting the cavity. The latter combined with the radially upward fluid movement on the pressure side of the blade gives rise to a vortical structure in the interaction zone between the main and cavity flows. Low values of total pressure loss coefficient are attributed to this additional mixing now present for the 25% clocking position. Moreover, both non-uniform cases experience a strong upward fluid motion on the pressure side of the blade that is intensified as we approach the cavity inlet. More fluid enters the cavity for both non-uniform cases and apparently exits at another plane when compared to the uniform case.

An additional vortex is present for the 25% circumferential clocking position, pushing the tip passage vortex to migrate radially lower, leading thus to greater mass flow being involved in that vortex, Figure 5.10. At the 50% clocking position a strong radial inflow into the cavity can be identified. A dramatic improvement of the flow field can be seen for the 14.0 case in terms of in and outflows.

Figure 5.11 presents the experimentally measured pitchwise mass-averaged pressure coefficient value for design B of the non-uniform ring clocked in 3 positions compared to the 14.0 case of 0.17c width. Measurements were made up to 40% of the blade span and inside the cavity. At the tip region, specifically at 95%, inside the main flow a slight difference between the cases can be identified. The uniform insert and the non-uniform cases clocked at 25% are identical. This implies that when the flow impinges on the upper wall casing it does so when the non-uniform ring has its lowest additional width. When the ring is clocked at 50% and 75% losses seem to gradually reduce, but on a marginal level. Below 95% of the blade span the flow field is identical for all 4 cases compared. Inside the cavity the pressure is reduced in particular for the 75% clocking position, leading to a potentially lower pressure difference across the labyrinth. This is expected as in the 75% clocking position the high-pressure fluid is prevented from entering the cavity. Less fluid will now be pumped over the shroud. The wider bump performs better compared to design A. The smother curvature along the circumference shows less loss being generated.

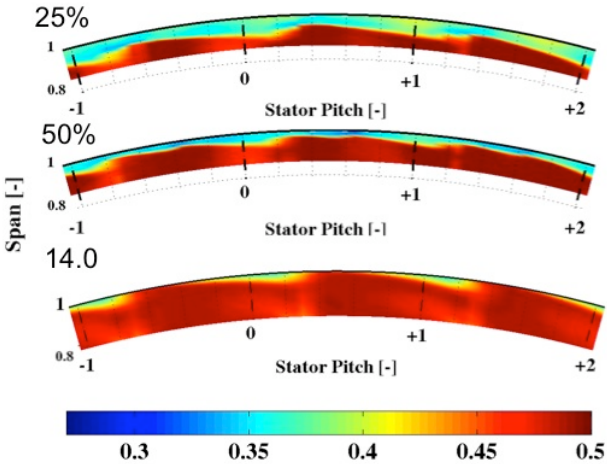

a.

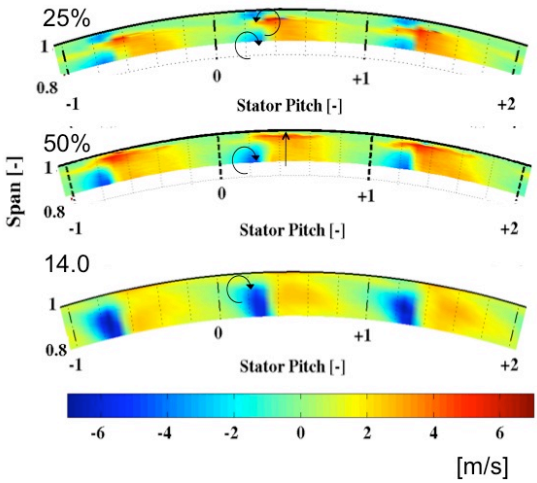

b.

Figure 5.10: Experimentally measured time-averaged (a) total pressure loss coefficient and (b) radial velocity. Comparison between the cases: non-uniform 25%, non-uniform 50% of the first design and 14.0. Stator exit

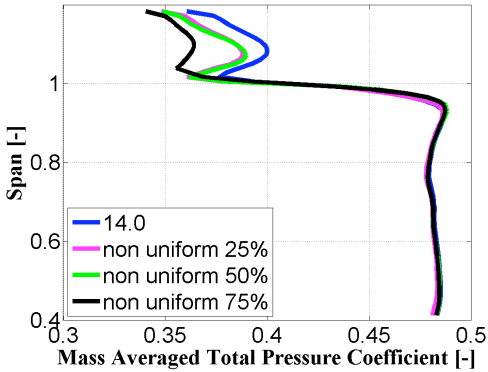

Figure 5.11: Experimentally measured pitchwise mass-averaged total to static pressure coefficient; comparison between the cases: non-uniform clocked at positions 25%, 50% and 75% of the design B and 14.0. Stator exit

Losses were expected to be higher at the tip region owing to the overall increased length of the non-uniform insert compared to the 14.0 case. The extended width should have provided the necessary space for the new boundary layer to develop, a process known to be loss generating. However, this was not experimentally observed. For the clocking positions of 50% and 75% the losses attributed to the upper casing boundary layer are reduced, whereas the 25% clocking position resembles the 14.0 case. Up to the trailing edge of the stator blade the new boundary layer generation mechanism is active. Once this is released from the blade passage the skewed boundary layer is subjected only to the main swirling flow. This causes the skewed boundary layer to straighten up. The longer length on the endwall provides the necessary space for the boundary layer development. As a result, a less skewed boundary layer appears at the sampling station.

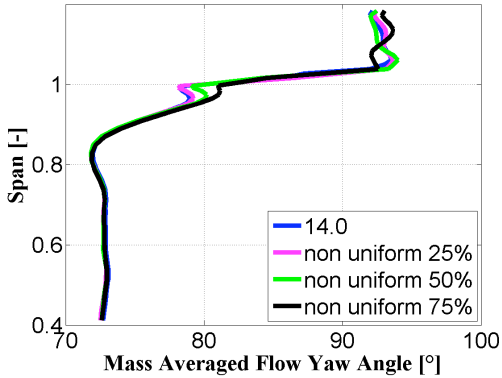

Figure 5.12: Experimentally measured pitchwise mass-averaged flow yaw angle; comparison between the cases: non-uniform clocked at positions 25%, 50% and 75% of the design B and 14.0. Stator exit

Another mechanism that also contributes to the reduction of losses in that area is the increased suction inside the cavity though the inlet area for the non-uniform cases which is now less with the pressure drop across the rotor acting as a driving force to remain the same. The new boundary layer forming at the casing is sucked into the cavity. The low momentum boundary layer originating from the upper casing fills the cavity instead of the high-energy fluid from the pressure side of the blade. When examining the absolute yaw angle at stator exit, Figure 5.12 shows that a difference from 95% - 100% of the blade span can be identified. While the uniform 2mm case is identical in the main flow with the non-uniform clocked at 25% as already mentioned the other 2 clocking positions differ. The overturning part of the upper passage vortex appears to be elongated, reaching 80° and 82° respectively for the 50% and 75% cases. Since the underturning part remains unaltered, the vortex is of the same size. The newly formed boundary layer of the upper wall casing is the one causing the elongation of the overturning leg. The 75% clocking position has the smallest boundary layer height forming at larger angles and while within the interaction zone between the two flows at the tip region the flow experiences a 10° jump from the main flow to the cavity. Shear stress in that region is high which is a loss-generating mechanism. Therefore, when the non-uniform ring is clocked at 75% of the stator pitch the lowest stresses are experienced since the smallest jump exists.

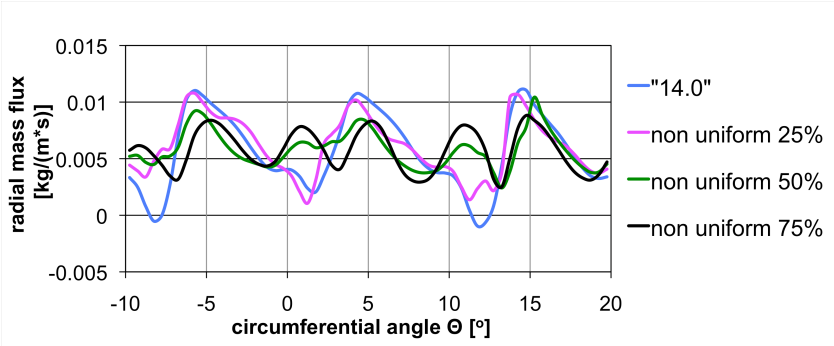

Figure 5.13: experimentally measured radial mass flux at h=0.994. Stator exit

A circumferential mass flux averaging on that measurement plane as shown in Figure 5.13 and with h=0.994 reveals that all cases compared experience radial mass flux variations. Oscillations on the balance of in and outflows owing to the potential rotor flow field are similar for all cases. Specifically, the uniform 2mm and 25% clocking position follow the same trend, and the 50% and 75% clocking positions experience almost identical oscillations. Nevertheless, the mass flux entering the cavity at this measurement plane is 7% less for the 14.0 case compared to the 25% clocking position, and respectively the 3% and 2% from the 50% and 75% clocking positions. This reveals that both the stator and the rotor are influencing cavity flow mechanisms. The stator dictates the amount of mass flux that finally enters the cavity, but the rotor in turn regulates the in and outflow oscillation.

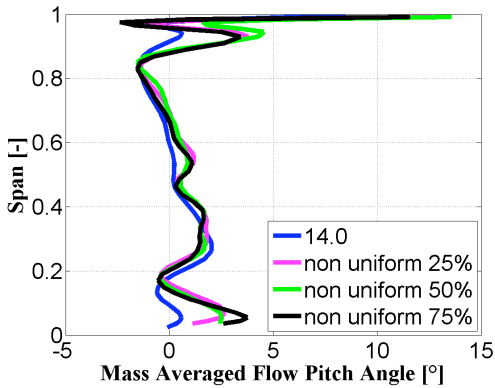

Figure 5.14: Experimentally measured pitchwise mass-averaged pitch angle: comparison between the cases with 14% cavity volume reduction. Rotor exit

Whereas at the stator exit there is a resemblance between the uniform insert of 0.17c width (14.0) and design B of the non-uniform insert, as far as the flow field is concerned this is not the case at the rotor exit. In Figure 5.14 the pitch-wise mass-averaged flow pitch angle distribution is shown for the cases mentioned above. Two main differences can be distinguished between the uniform 0.17c and the non-uniform cases. The tip passage vortex is considerably increased in size for the non-uniform cases and across the span non-uniformities are present. The onset of the rotor's tip passage vortex is at the rotor leading edge. Since the mass flow leaking through the labyrinth is of the same range for all four cases, the magnitude of the tip vortex is only influenced by the way the mass flow is being exchanged between the cavity and the main flow in front of the rotor inlet, namely the angle of the re-entry path, as well as the relative time frame within which this takes place. The extended tip passage vortex for the non-uniform cases is what influences the flow from span 0.2 – 0.8 causing increased secondary non-uniformities. A larger and more energetic vortex that has positioned itself at a lower span 'squeezes' the fluid underneath and at the same time a greater mass flow exchange takes place. In the wake region the flow breaks down and small vortices appear. The interaction between the vortices along the span influences the hub passage vortex as well.

A supplementary computational study for the cases of 14.0 and the non uniform design A is presented in Figure 5.12. In the upper row in Figures

5.12a, 5.12b and 5.12c a meridional cut of the inlet cavity is shown at the instant in time when they are in the PS of the rotor blade, whereas below, Figures 5.12d, 5.12e and 5.12f show the inlet cavity after the leading edge has passed. Two vortices that exist inside the cavity. The upper one resides in the upper half of the cavity, which remains unaffected by the blade pressure field in terms of size and magnitude, and the lower one that interacts with the main flow. This lower vortex is greatly influenced by both the stator and rotor pressure fields. When the high-pressure fluid originating from the stator's pressure side reaches the cavity entrance, fluid is pumped into the cavity. A small corner vortex is formed on the upstream radial wall of the cavity at the interaction zone. This vortex will grow in size, as it will start migrating radially upwards until the moment that the potential field of the rotor redirects fluid into the cavity, washing away the vortex, as in Figure 5.12. Although the non-uniformity of the insert was designed to block the high-pressure fluid coming from the pressure side of the stator blade to enter the cavity, it did not act in this direction. On the contrary, it blocked the flow only in a way that would potentially lead to greater loss generation. Right at the peak of the bump the flow experiences a sudden change in direction from an axial to a radial direction, as depicted in Figure 5.12b, towards the inside of the cavity regardless of the circumferential position of the bump relative to the stator's trailing edge. For the flow that is already circulating inside the cavity the bump acts as a deflector and redirects the flow that would have otherwise exited the cavity back into the axial direction and later into the vortex that dominates the upper part of the cavity. Although the mass flow that finally escapes through the labyrinth over to the exit cavity is computed to be greater for the uniform case of 0.17c width, as in Table 5.2, the extended in and out flows for the non uniform cases are what ultimately lead to greater mixing at the interaction zone, thus producing more losses.

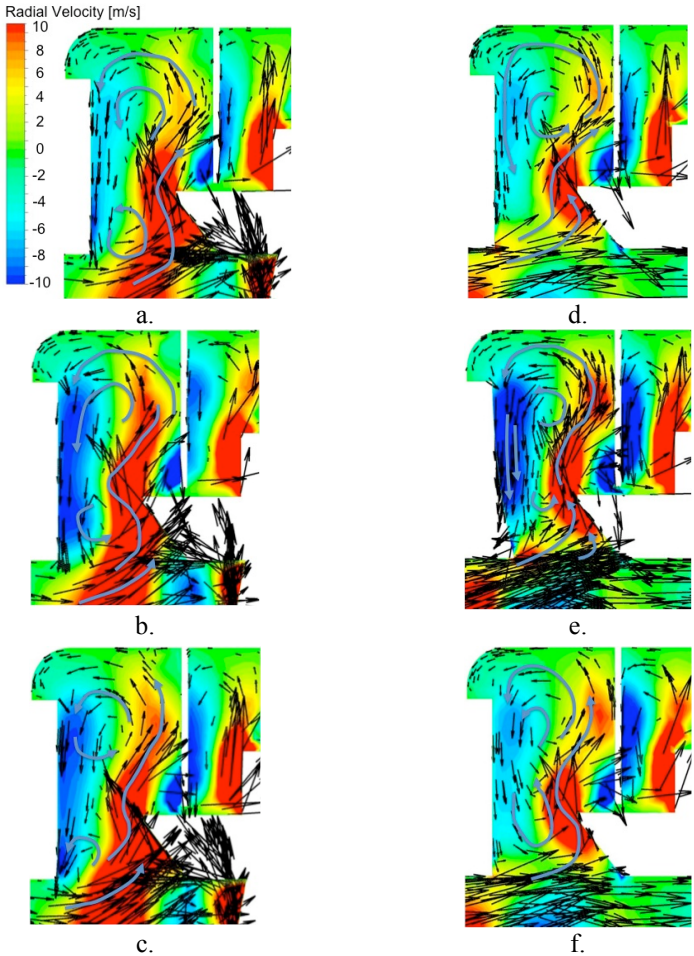

Figure 5.12: CFD simulations on the inflow at inlet cavity for the cases (a) uniform 0.17c, (b) design A of non-uniform clocked at 25%, (c) design A of non-uniform clocked at 50%; and the outflow for the cases (d) uniform 0.17c, (e) design A of non-uniform clocked at 25%, (f) design A of non-uniform clocked at 50%. The planes are coloured with radial velocity and the secondary flow vectors are projected onto them. The flow path is denoted by blue lines.

A computational study of the flow field during inflow and outflow is presented in Figure 5.13 for the non-uniform design B. In the upper row in Figures 5.13a, 5.13b and 5.13c a meridional cut of the inlet cavity is shown for the instant in time when they are in the PS of the rotor blade, whereas below, Figures 5.13d, 5.13e and 5.13f show the inlet cavity after the leading edge has passed. The sudden change in direction from axial to radial at the lower corner of the upstream radial wall of the cavity is still present. Nevertheless, it is now reduced in magnitude and less fluid is involved, even when compared to the uniform case. It is this fluid that destroys the lower vortex of the cavity that interacts with the main flow. This outward radial movement contradicts the fluid that has been involved in the circular motion and had already started moving downwards staying attached to the upstream radial wall of the cavity towards the exits and back into the main flow. The vortex is re-energized by the high-pressure fluid originating from the stator that follows right after this flow.

The circumferential position of the non-uniform ring has only a minor influence on the path of the high-pressure fluid that finally finds its way into the cavity, as shown by Figure 5.13. The 75% circumferential clocking position is the one that has the bump positioned exactly on the path of the fluid that is to go into the cavity, see Figure 5.13f. The slightly reduced inflow for the 75% circumferential clocking position pushes the fluid residing close to the interaction zone at h=1 upwards. For both other circumferential clocking positions presented in Figure 5.13d and 5.13e a vortex is present at the lower end of the cavity that interacts with the main flow. On the other hand, the circumferential position of the non-uniform ring greatly influences the downward moving fluid moves to exit the cavity. Especially because of the curvature of the cavity's upstream wall the fluid is redirected towards the axial position and back into the upper vortex residing in the cavity. In such a way the interaction between the main flow and the cavity exiting flow is substantially reduced. The fluid will exit the cavity when low-pressure fluid of the stator's suction side passes underneath the cavity.

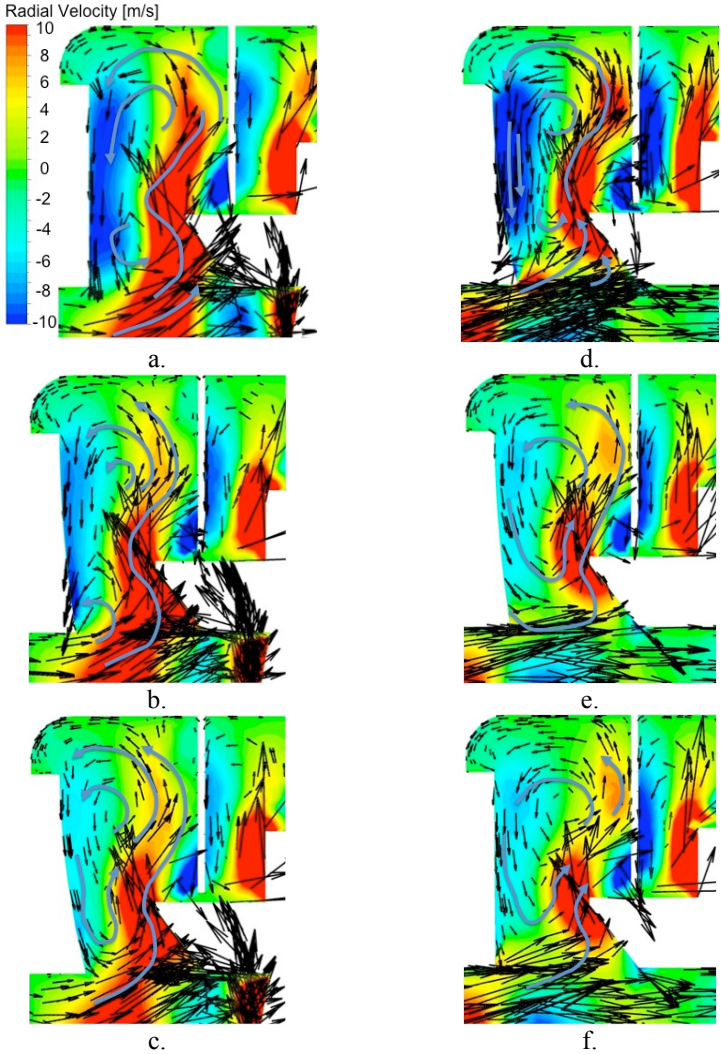

Figure 5.13: CFD simulations on the inflow at inlet cavity for the non uniform design B cases (a) 25%, (b) 50%, (c) 75%; and the outflow for the cases (d) 25%, (e) 50%, (f) 75%. The planes are coloured with radial velocity and the secondary flow vectors are projected onto them. The flow path is denoted by blue lines.

At the time the non-uniform ring is at its closest to the rotor's shroud point the cavity fluid will not manage to exit the cavity. In the 25% clocking position the bump intensifies the downward movement of the cavity flow, although the flow will not manage to interact with the main flow. It is important to note the increased interaction for the 25% and 50% cases at the PS of the blade with the lower cavity vortex still present. On the contrary the 75% case experienced only a decreased inflow and reduced interaction as shown in Figure 5.13f.

5.2.2 Cavity Volume Reduction of 28%

In this group two cases were examined. They are shown in Figures 2.6b and 2.9b. Both of them have a cavity volume reduction of 28% relative to the initial cavity volume shown in Figure 2.5. The use of the 28.0 ring covers 1/3 of the available inlet to cavity area whereas the slanted case employed an insert that blocked 85% of the available area while maintaining the necessary safety distance of 0.16c from the shroud. This configuration did not allow for measurements in the main flow at stator exit, as the probe cannot pass through. For the slanted insert (Figure 2.9b) it should be noted that fluid cannot migrate radially outward towards the inside of the cavity. If fluid moves into the cavity it has to travel backwards. A look into the cavity region would reveal that the slanted insert blocks most of the fluid that would have

Case	Mass flow leaking through the labyrinth [g/s]
28.0	73
Slanted	50

Table 5.2: Mass flow in g/s leaking through the labyrinth for the cases uniform 0.34c and slanted

entered if the cavity entry was free of blockages. The flow only entered the cavity and never went back into the main flow. Interaction with the main flow was limited only to the inflow. One big vortex dominated the cavity (Figure 5.14), maintaining the same position and magnitude independently of the positioning of both the stator and rotor blades. Due to flow strangling in the slanted case, the mass flow leaking through the labyrinth was reduced by approximately 30% relative to the 28.0 case (Table 5.2). Nevertheless, the leakage fraction did not seem to greatly influence the flow kinematics of the

region. The steady state results for the 28.0 case revealed a rather weakened inflow into the cavity spread over 30 degrees that was intensified when in the PS of the downstream rotor. The upper vortex inside the cavity was also present for the 28.0 case, which did not interact at all with the main flow. In the lower corner of the upstream radial wall of the cavity in the place where the insert was positioned in the slanted case a rather small vortex appeared when in the SS of the blade.

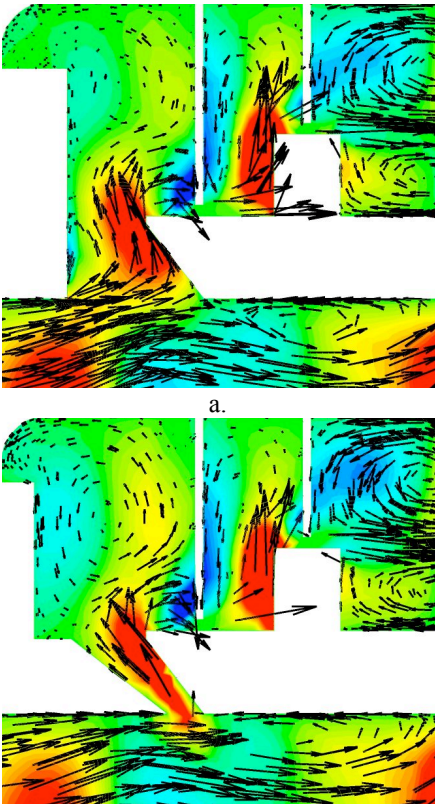

a.

b.

Figure 5.14: Meridional cut of the rotor inlet cavity when on he pressure side of the rotor blade for (a) 28.0 and (b) slanted. The plane is colored with radial velocity and the secondary vectors are projected on the plane.

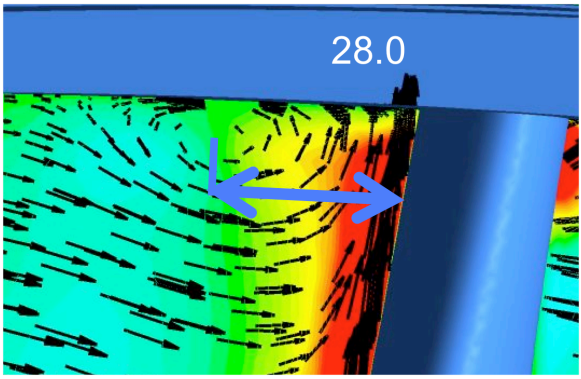

a.

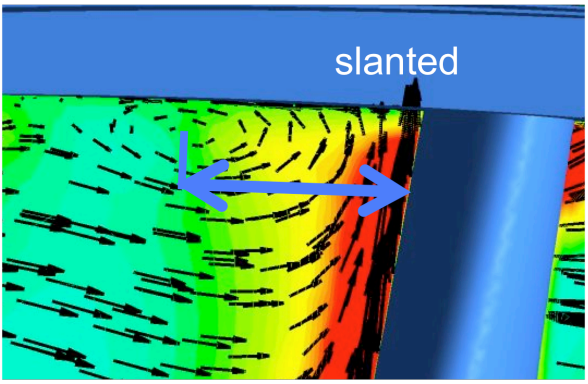

b.

Figure 5.15: Downstream view of the rotor passage with the horseshoe vortex formation for the cases (a) 28.0 and (b) slanted. The plane is colored with radial velocity and the secondary vectors are projected on the plane.

Despite the resemblance of the flow at the area of the cavity entrance when the flow enters the rotor passage there is a difference in the horseshoe vortex formation between the two cases. In Figure 5.15 the downstream view inside the rotor passage shows the onset of the horseshoe vortex. The plane is perpendicular to the pressure side of the rotor blade, colored with radial velocity and the secondary velocity vectors are projected onto the plane. It is apparent that the horseshoe vortex that will later develop to the passage vortex

has already started migrating towards the suction side of the adjacent rotor blade. For the slanted case the vortex core is a distance greater from the rotor blade compared to the 28.0 case. A vortex, which is not confined by walls expands more enabling more mass flow, introducing potentially greater mixing.

This vortex remains inside the cavity area detached from both the upper vortex as well as from the main flow and was flushed away when high-pressure fluid was pumped into the cavity. The axial extent of this jet that penetrates the cavity did not appear to be bigger than that of the slanted case. Therefore, the influence of these 2 inserts on the main flow does not differ considerably. Consequently, when examining the flow field at rotor exit in Figure 12 it is easy to identify the expected scenario of the 2 cases as being profoundly similar.

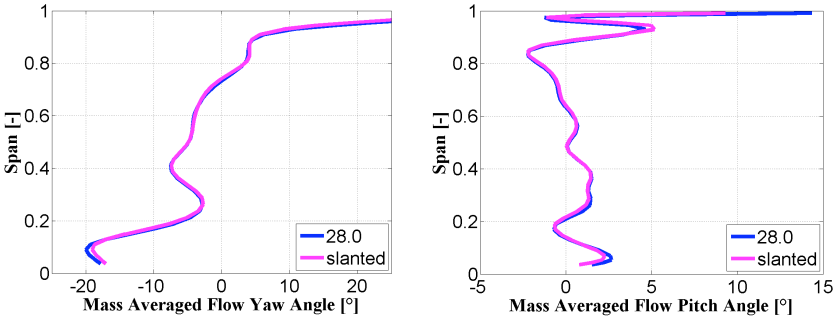

a. b.

Figure 5.16: Experimentally measured pitchwise mass-averaged flow yaw (a) and pitch (b) angles at rotor exit. Comparison between the 28.0 and the slanted cases

Summary

This paper presented a systematic and coherent investigation on the rotor inlet cavity of a two-stage axial steam turbine. A number of modifications of the inlet cavity geometry were studied while maintaining the same volume. Two sets of inserts were tested, offering a cavity volume reduction of 14% and 28% relative to the initial cavity volume of the baseline case. The impact of these inserts on stage efficiency through the handling of the leakage flows was investigated.

The use of the simplest geometry variation, namely an extension of 0.17c and 0.34c of the upper stator casing wall, performed the best compared to all other cases examined here. The uniform 0.17c insert showed an efficiency gain of at least 0.3% compared to the non-uniform cases, whereas in the second group the uniform 0.34c insert showed only marginal efficiency gain of 0.1%, which is within the efficiency accuracy measurement range of the test turbine employed.

The leakage mass fraction, as predicted by the simulation, showed no measurable influence on the performance as it was measured to be of the same range for all cases examined. On the other hand, what is of crucial importance is the way mass flow is exchanged between the cavity and the main flow. The second non-uniform design performed the best as it forced the downward moving fluid to remain inside the cavity, thus reducing the mixing in the interaction zone. Nevertheless, at the rotor exit a greater tip passage vortex for all non-uniform cases seemed to worsen the flow field and create overall a stage efficiency deficit. The second group examined, which had the 0.34c insert added, performed similarly to the slanted case, where 85% of the available inlet area was blocked. The two cases showed an identical flow field at rotor exit, a fact that also points to the similarity of the flow conditions at the rotor inlet.

This study made evident the importance of the inlet cavity geometry. Maintaining the same cavity volume while changing the geometry leads to similar mass flows leaking through the labyrinth. However, what changes dramatically is the mass flow exchange taking place between the cavity and main flow. The re-entry path greatly influences the onset of the rotor tip passage vortex regulating the size and position of the latter at the rotor exit. The smoother the re-entry angle is, the smaller the vortex that appears at rotor exit and the less the non-uniformities across the span, thereby leading to increased efficiency.

Overall, this study suggests that the mixing occurring in the interaction zone is greatly affected by small, targeted changes in the geometry of the inlet cavity. Prints of these changes can be identified at the exit of the downstream blade row.

6. Sensitivity Analysis On The Impact Of Rotor Leading Edge And Tip Clearance Gap On The Overall Aerodynamic Cavity Performance

With the use of computational resources a sensitivity analysis has been performed on the impact of rotor leading edge and tip clearance gap on the aerodynamic cavity performance. On a first approach the downstream rotor leading edge geometry is modified to investigate to what extend it influences the mass flow oscillations at the interaction zone and consequently the mixing and the losses. Originating from a baseline case the leading edge is turned to generate a smaller positive incidence compared to the baseline case (Design A) and more positive one (Design B). On a second step the tip clearance gap is modified to study its effect on the mass flux balance inside the cavity and the generated losses. The amount of leakage mass flow through the labyrinth directly impacts on the mixing losses at the interaction zone, as the mass flow not escaping will be circulating in the cavity vortex and ultimately interact with the main flow.

6.1 Leading edge modification

In Figure 6.1 the experimentally measured flow relative yaw angle is shown against the rotor design blade metal angle at rotor inlet. The effect of the cavity flows is evident on the upper 20 percent of the blade span. Although the flow yaw angle follows the design angle till span 0.8 a large, increasing with span offset, is present from span 0.8 till 1.0. The mixing of the cavity and main flows results on the large positive yaw angle at the rotor blade reaching up to 40°-50° at the tip of the blade.

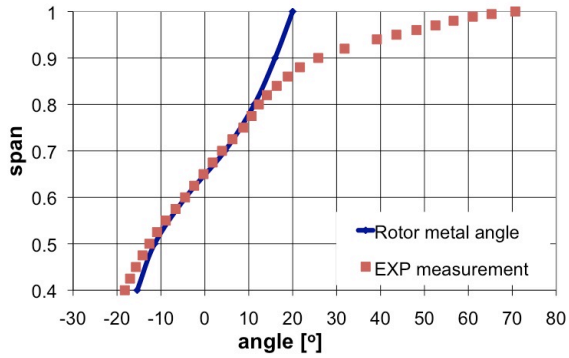

Figure 6.1: Metal angle of the 2nd rotor blade at leading edge (blue line) and flow relative yaw angle experimentally measured at inlet of the rotor (red dots)

The impact of the positive incidence on efficiency compared to the other two cases computationally studied is presented in Figure 6.2. Design A having a positive metal angle (+12 degrees) compared to the baseline case (-19 degrees) balances the large positive incidence of the baseline case. Therefore, an increase in efficiency is calculated of 0.21%. On the other hand, a turn of the metal angle towards more negative values also led to an increase of 0.19% in efficiency. This is owed to the off-loading of the tip section. The camper angle of the blade is reduced and so do the losses because of the blade turning.

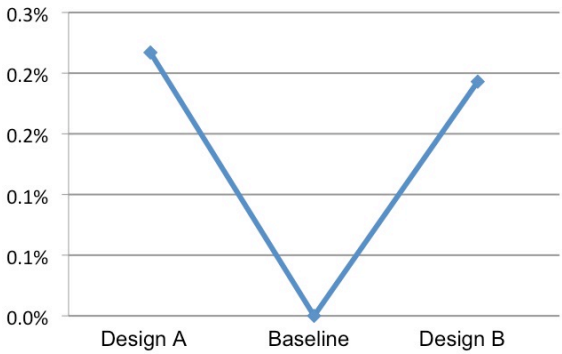

Figure 6.2: Total-to-total efficiency (computationally calculated) of the three cases compared in this study. The efficiency of the baseline case is used as reference.

As expected the modification of the rotor leading edge towards more negative values results in a suction side flow diffusion, leading to an adverse pressure gradient shown in Figure 6.3a and a consequential flow separation. Contrary to the Design B, Design A exhibits no suction side flow diffusion. The stagnation point has moved closer to the leading edge with the flow being accelerated already from the leading edge. The computations do not predict any influence of the leading edge modifications between the cases on the pressure side of the blade. The leading edge modifications affect the flow field down to 70 percent of the rotor blade span. The leading edge modification at the tip of the blade required for a smearing out of this geometrical change down to 70 percent of the blade span. A slight difference of the loading between the cases is still visible at this blade span (Figure 6.3b).

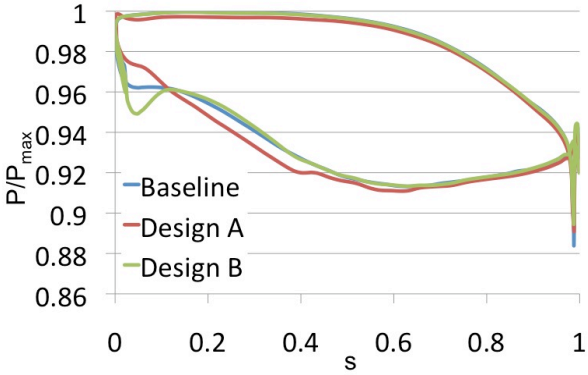

a.

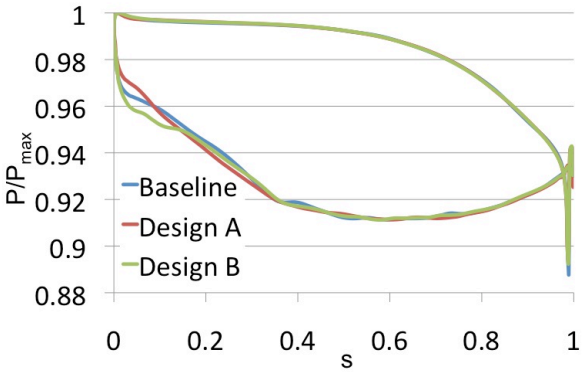

b.

Figure 6.3: Blade loading of the cases examined at (a) 95 percent and (b) 70 percent of the blade span.

The formation of the corner vortex at the rotor blade for the three cases examined is shown in Figure 6.4 with a downstream view. The r-θ planes are colored with radial velocity, with red colored areas depicting upwards moving fluid and transient averaged velocity vectors are projected on the planes. The two planes are axially distanced from the stator's trailing edge Z=0.968 and Z=1.126. The axial stator rotor distance at span=1.0 is used to non-

dimensionalize. The backwards swept of the leading edge of the baseline rotor causes the flow to migrate upwards in its vicinity, Figure 6.4a. Because of the positive incidence (Figure 6.1) the flow travels around the leading edge and over to the suction side. This results in the flow migrating in positive radial and circumferential direction. The merge with the flow of the blade suction side that moves under negative flow yaw angle leads to a counter clockwise rotating vortex being formed on the suction side close to the upper casing. Design A faces a reduced downward flow movement of the flow that is to travel around the blade, Figure 6.4c, as well as less pronounced upward movement that is attached to the blade. As a result, the vortex formed although at the same span location it is profoundly weaker leading to less mixing and hence less losses are produced. Additionally, the counter-rotating vortex which was underneath the corner vortex in the baseline case is not present in the Design A case. On the other hand, Design B as having a leading edge design similar to the baseline case the flow field is comparable with the on from the baseline case. Nevertheless, the intensity of the flow travelling over to the suction side is reduced. Moreover, the lean onto the suction side pushed the corner vortex to migrate at a lower span and loose strength. The small counter-rotting vortex underneath is now smaller.

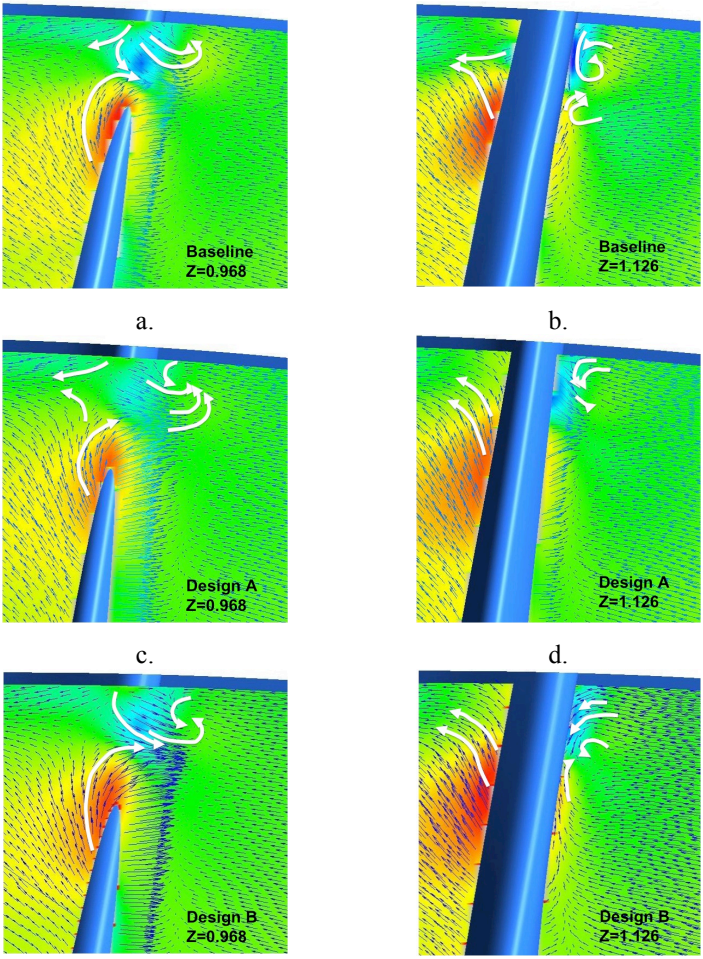

Figure 6.4: Downstream looking r-θ planes at rotor inlet and for Z=0.968 (a, c and e) and Z=1.126 (b, d and f). The distance is non-dimensionalize with the stator-rotor distance at span 1.0. The planes are colored with radial velocity and secondary flow vectors are projected onto the planes. The flow path is denoted with white lines.

In Figure 6.5 the radial mass flux into the cavity at cavity inlet (span 1.0) is shown for the three cases. The mass flux is axially summed and circumferentially plotted. Between the cases no measurable differences can be identified. Therefore, the leading edge geometry does not influence the oscillating cavity flow in and out of the cavity and hence the mixing process taking place at the interaction area. Nevertheless, it has to be mentioned that only the rotor inlet cavity was modeled introducing a constant leakage flow through the labyrinth for all cases.

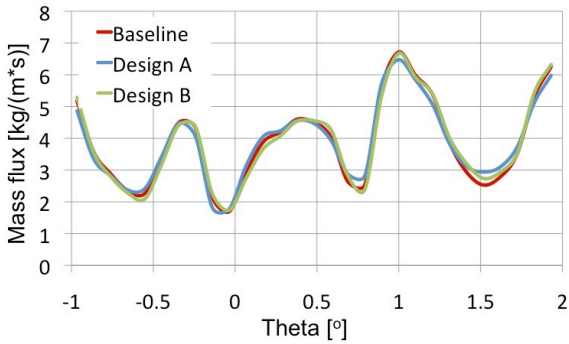

Figure 6.5: Radial mass flux into the cavity at cavity inlet (span 1.0) for all three cases examined in this study.

In Figure 6.6 the flow conditions at cavity inlet verify the Figure 6.5. It is qualitatively shown that the leading edge modification does not influence the flow field at the cavity inlet.

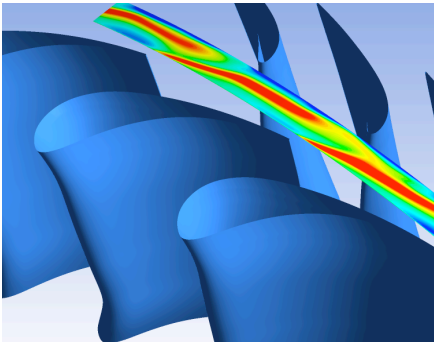

a.

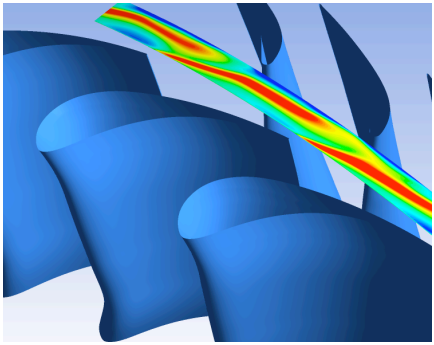

b.

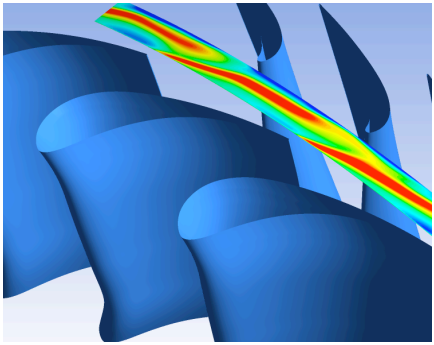

c.

Figure 6.6: Cavity inflow flow field for (a) baseline, (b) design A and (c) design B. The plane has been colored with radial velocity with red color showing the inflow to the cavity.

6.2 Impact of Tip Clearance Gap

The tip clearance is fixed by mechanical constraints such as thermal loads. Although not applicable in reality the gap size through a computationally study was reduced to half (case B) its experimental size of 0.44% of the span height (case A). Although, a smaller gap size potentially leads to lower losses through reduced leakage mass flow the study revealed an increased mixing at the interaction zone when reducing the gap size.

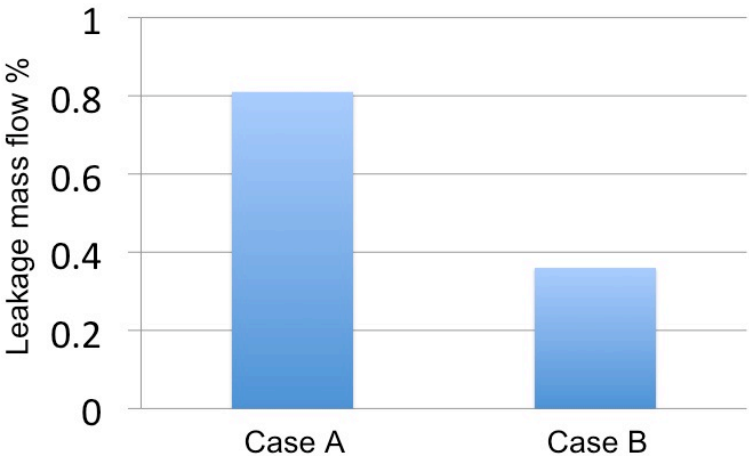

Figure 6.7: Mass leakage flow that escapes through the labyrinth for the two cases expressed as a percentage of the main mass flow

The computation performed could only predict an efficiency change of 0.04% between the cases. Nevertheless, the flowfield is greatly affected. In Figure 6.7 the percentage of the leakage mass flow against the main mass flow is presented for the two cases. There is a reduction of 53.1% with half the gap size indicating a linear relationship.

The inflow to the cavity is presented in Figure 6.8 for both cases. Qualitatively, the flow features between the two cases do not differ. Nevertheless, the cavity vortex is stronger for the case A. Although it was expected that the smaller gap would re-direct more mass flow towards the main cavity vortex though the leakage mass flow is reduced, the cavity vortex of the case B is not as strong. The counter-rotating vortex that is positioned above the shroud on the bottom right corner of the cavity circulates the mass flow that did not escape through the labyrinth. The existence of the counter-rotating vortex it also incorporates in its circular movement the mass flow that previously stagnated on the top right corner of the cavity. It also ensures a continuously regulated escape of the leakage mass flow as opposed to the downwards moving jet that pushes the flow through the gap in case A. On the left side of the cavity the downwards moving flow is similar.

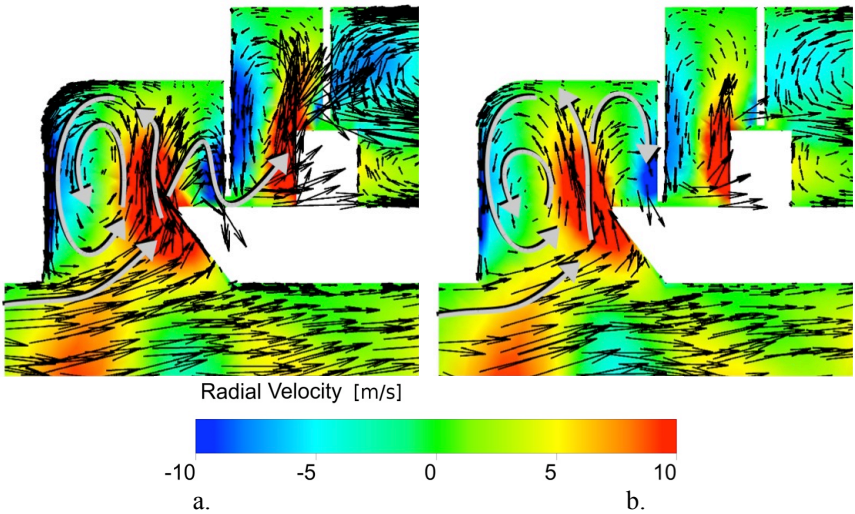

Figure 6.8: CFD simulations on the inflow at inlet cavity for (a) the case A and (b) case B. The planes are colored with radial velocity and the secondary flow vectors are projected onto them. The flow path is denoted by white lines.

During outflow (Figure 6.9) the situation remains unaltered. The case B experiences the same flow features but with a reduced intensity. It is worth mentioning the lower span position of the cavity vortex center that is even

below the shroud. The outflow region of case A is more expanded, confining the upwards moving jet resulting thus in higher radial velocities.

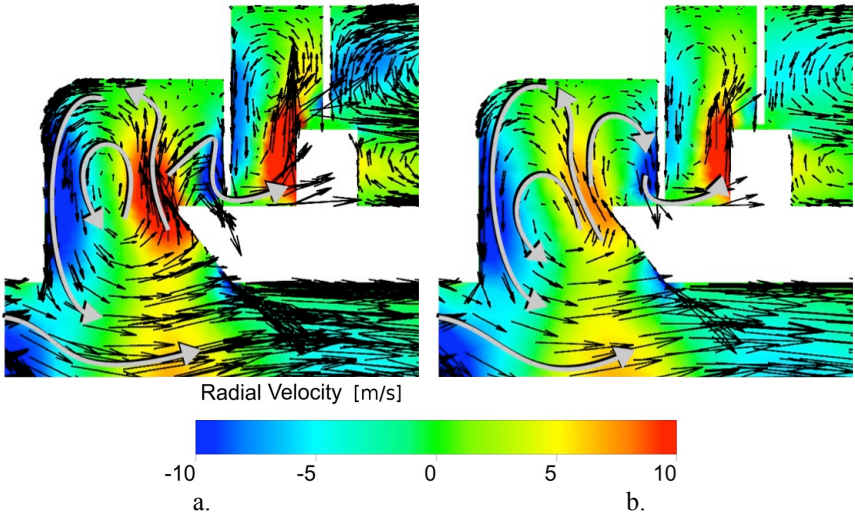

Figure 6.9: CFD simulations on the outflow at inlet cavity for (a) the case A and (b) case B. The planes are colored with radial velocity and the secondary flow vectors are projected onto them. The flow path is denoted by white lines.

In Figure 6.10 the mass flux at the cavity inlet is presented. The mass flux is time averaged so the impact of the stator pressure exit field at the cavity flow at the interaction zone is evident. The mass flux at case A receives higher values.

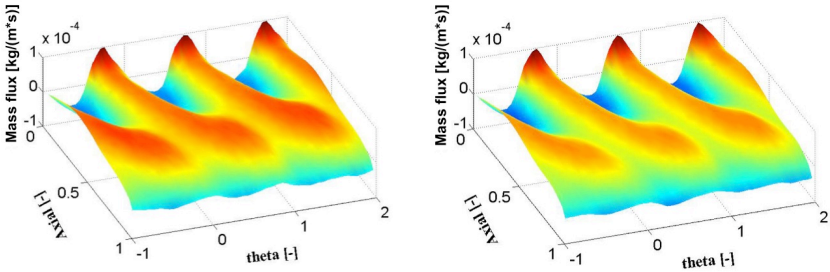

a. b.

Figure 6.11: Time-averaged unsteady mass flux at the cavity inlet (h=1) for (a) case A and (b) case B. The mass flux is averaged over 20 time steps

The peak values of the mass flux for case A for both the in and outflow are increased as shown in Figure 6.11a. The mass flow into the cavity is smaller by 58.5% for the case B. On the contrary the outflow is increased by 44.5%. Therefore, the leakage flow although decreased in case B the mass flux oscillations are increased at the cavity inlet leading potentially to more losses being generated because of greater mixing. In Figure 6.11b the averaged mass flux over the circumferential direction is plotted along the axial cavity length. The portion of the mass flow, of the upwards moving jet that is redirected to the right towards the gap is reduced by 50% in case B.

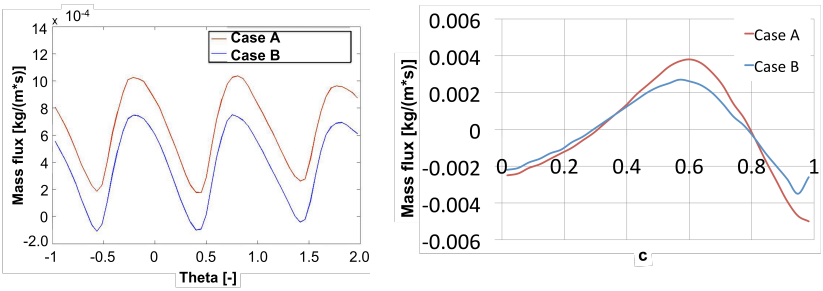

a. b.

Figure 6.12: (a) Time averaged mass flux at cavity inlet (h=1) summed over the axial cavity length and (b) mass flux inside the cavity at h=1.06 summed over the circumferential direction against the axial cavity length.

Summary

The impact of geometrical modifications of the rotor leading edge geometry on stage efficiency is examined. An initially experimental work was supplemented with computational analysis. Three different leading edge geometries have been studied.

The baseline leading edge was modified from an initial value of -19° compared to the axial direction to +12°, Design A and to -30°, Design B. Design A intended to better match the flow conditions, namely the large positive incidence encountered by the rotor leading edge in the baseline case due to the influence of the cavity flows onto the main flow. Design B indented to examine the influence of off-loading the tip of the rotor blade.

Both modifications showed an efficiency increase relative to the baseline case. Although the leading edge modification had no measurable influence at the inlet cavity area, it did influence the flow around the leading edge as well as the corner vortex formation on the suction side of the rotor blade. This resulted in an efficiency increase of 0.21% for the Design A and 0.19% for the Design B relative to the baseline case.

The corner vortex formed on the suction side of the rotor blade and close to the upper casing was noticeably reduced for the Design A. The leading edge modification led to weak crossing over of the fluid from the pressure to the suction side. Since the positive incidence was reduced less mass flow traveled to the suction side hence, a weaker corner vortex was formed. The off-loading of the tip through the Design B modification resulted in an also weaker vortex migrated to a lower span location. Additionally, the modification created an adverse pressure gradient in the suction side.

The influence of the geometry of the rotor blade leading edge on the flow field from the flow at the interaction zone is decoupled. The inflow to the cavity although dictated by the potential flow field of the rotor shows no direct influence by the leading edge geometry itself. Therefore, the rotor leading edge can be modified to better match the cavity outflow increasing thus efficiency without influencing the performance of the cavity.

Overall, this study suggests that the design of the rotor leading edge is not trivial. Slight modifications on the geometry alternate the flow field around the blade leading to efficiency increase.

Additionally, a computational study on the impact of the tip clearance gap has been performed for the case with the highest efficiency. The tip clearance was reduced to half its initial size while all other parameters remain unaltered.

The leakage mass flow was reduced to half compared to the reference case and therefore the efficiency losses owing to this. Additionally the flow that was re-directed towards the gap was reduced to half as well indicating a linear relationship between them.

The overall mass flow that entered the cavity was reduced by 58.5%, nevertheless the mass flux oscillations point towards a greater loss production at cavity inlet.

7. Conclusions and Summary

7.1 Conclusions

An experimental work complemented by a computational analysis on the effective reduction of the leakage flow interactions of a two stage axial shrouded turbine has been presented. The blade geometry is characteristic of a high-pressure steam turbine section. The experimental work has been performed in 'LISA', the turbine test facility of the Laboratory for Energy Conversion at the ETH Zürich. Pressure measurements were performed using miniature in size probes for minimum blockage effects that have been in-house developed. The computational study supported the experimental work providing both qualitative and quantitative results.

Various rotor inlet cavity modifications were studied. The geometry as well as the volume were varied to examine their impact on stage efficiency. Overall the 28.1 case performed the best. An efficiency increase was measured of 1.6% compared to the baseline case. The 28.1 case had a 28% cavity volume reduction compared to the baseline case whereas the axial to radial cavity wall ratio was increased from being 0.66 for the baseline to 0.9 for the 28.1 case. The square-shaped cavity reduced not only the mass flow oscillations at the cavity inlet by 20%, but also the leakage mass flow by 1.6% compared to the baseline case. The reduced radial cavity length pushes the vortex to migrate at a lower span position having its lower side close to the cavity inlet area. Therefore, there was no need for the fluid entering the cavity to be radially transported before it got trapped into the cavity vortex reducing thus the mass flux oscillations and hence improving performance. The cavity volume reduction of 14% through radial cavity wall length reduction did also improve the stage performance by 1.1%. Although in this case there was no leakage flow or mass flux oscillation reduction the position of the cavity vortex played as well a key role in circulating the flow and re-injecting it back into the main flow.

On the other hand, the cavity volume reduction through extension of the upper casing stator platform did not show a monotonic behavior in terms of

efficiency against cavity volume. The axial extension of the upper casing influences the flow in and outside the cavity. Extending the casing allows the main flow to continue overturning once outside the stator blade passage and before it enters the cavity. Therefore, the step in yaw angle experienced by the flow is reduced and so does the shear.

The zone of influence of the upstream stator pressure exit field and the downstream rotor potential flow field on the cavity were quantified. They both extend 60% of the axial cavity distance on either side. The high pressure fluid originating from the pressure side of the stator blade facilitated with mass flow the cavity vortex whereas the rotor potential flow field regulated the in and out flows. The extension of the upper stator casing platform by 34% of the initial axial cavity length as being close to the onset of the rotor zone of influence minimized the influence of the upstream stator. The cavity vortex was eliminated as well giving rise to radially aligned jets that washed in and out the cavity.

The main reason of the non-monotonic efficiency behavior lies on the flow conditions inside the cavity. Reducing the axial to radial cavity wall ratio impacts on the cavity vortex formation. As the axial cavity length decreases a single cavity vortex is not sustainable and breaks up into two smaller vertically aligned. The smaller vortex of the 14.0 case was engulfed inside the cavity area and did not extend beyond the interaction zone causing thus less mixing. Additionally, the lower vortex that still spined at the same frequency, handled only half the mass flow. Therefore, less mass flow mixed at the interaction zone with the main flow resulting in lower losses. The two smaller vortices of the 14.0 case resulted in an efficiency increase of 0.33% relative to the baseline case. A further extension of the upper casing stator platform caused only efficiency deficit. The efficiency dropped by 0.2% compared to the baseline case. The presence of jets that abruptly washed in and out the cavity without having the mass flow being smoothly regulated by the vortex caused the efficiency deficit. The jets penetrated into the main flow causing extensive mixing.

The mean streamline curvature of the mass flow entering the cavity driven by the radial pressure gradient, the area increase due to the cavity and the leakage mass flow was derived. For all cases was found to be 13 mm assuming an axial entry into the control volume bordered by the cavity inlet and the upper 10 percent of the blade span. For the cases with no axial extension of the upper stator casing the mass flow entry into the cavity was took place at the last 20 percent of the cavity inlet. Increased losses were observed for the cases with axial extension of the upper stator casing. As the

mass flow entry was moved downstream the entering fluid impinged on the inclined surface of the rotor shroud. The abrupt re-direction caused stronger jets, greater mixing and therefore more losses.

The additional rounding of the upper right corner between the upper cavity wall and downstream radial wall only deteriorated efficiency. The rounding introduced, pushed out the mass flow, formerly residing in the corner and the cavity vortex was intensified. That mass flow was previously trapped in the cavity corner. Although, no potential work production was possible there was no interaction of that trapped fluid with the main flow. The cavity vortex circulated 8%-10% more mass flow that interacted with the main flow at the interaction zone generating thus more losses. The intensification of the cavity vortex enabled also the fluid that used to drift between the vortex and the upper wall increasing even more the interacting mass flow. Additionally, the leakage mass flow experienced by the cases with the rounding was increased by 10% compared to the cases with the corner. The intensification of the cavity vortex led to its expansion inside the cavity. The incoming jet formed during ingress was bend towards the labyrinth reducing thus the volume in front of the gap. A reduced volume pumped more fluid across the labyrinth.

The use of non-axissymetric rotor inlet cavity geometry was in general not advantageous in terms of efficiency. All clocking positions deteriorated stage efficiency compared to the 14.0 case that served as a baseline case. The best clocking position was 75%, which reduced efficiency by 0.3% relative to the 14.0 case. Although, a correct positioning of the non-uniform ring blocked the mass flow from entering the cavity (75%), the egress from the cavity was such that the rotor tip passage vortex was enhanced at the rotor exit. Therefore, the gain at stator exit was lost by the bigger tip passage vortex at rotor exit.

The almost complete coverage (85%) of the rotor inlet cavity with the use of the slanted insert did not improve efficiency compared to the 28.0 that had the same cavity volume reduction and covered only 35% of the available inlet area. The 0.11% efficiency reduction, which is within the efficiency uncertainty measurement of the test facility used, points towards a greater mixing occurring at rotor inlet since at rotor exit the flow field was measured to be identical.

Two rotor leading edge geometry modifications were studied. Design A intended to better much the flow field experimentally measured and numerically verified at rotor inlet whereas Design B examined the influence of off-loading the tip of the rotor blade. An efficiency increase was computed

for both cases, of 0.21% for the Design A and 0.19% for the Design B relative to the baseline case. Although the leading edge modification had no measurable influence at the inlet cavity area, it did influence the flow around the leading edge as well as the corner vortex formation on the suction side of the rotor blade.

The use of swirl brakers inside the cavity to break the toroidal vortex led to increased losses being generated. Mass flow was abruptly re-directed back into the main flow introducing extensive mixing on the upper 15 – 20 percent of the blade span. Efficiency was deteriorated by 0.3% compared to the baseline case.

The impact of the reduction of the tip clearance gap to half its original value was computationally studied. The leakage mass flow escaping through the gap over to the first closed cavity reduced to half indicating a linear behavior between gap size and leakage flow. On the other hand, the mass flow that did not escape through the labyrinth was re-directed towards the main cavity vortex leading to greater mass flux oscillations at the interaction zone.

7.2 Summary

The length scale, the volume and the geometry of the cavity are of crucial importance when aerodynamic losses owed to cavity flows in axial turbines are addressed. Although leading unavoidably to loss production, the toroidal vortex inside the rotor inlet cavity plays the important role of smoothly circulating the flow inside the cavity, leading part of it to the labyrinth and the remaining back into the main flow. Therefore, it is of central importance for the turbine designer to fully incorporate the calculation of shroud leakage modeling in multistage turbine flow calculations. The mass flow that enters the cavity originates from the pressure side of the stator blade. As the high pressure fluid exits the stator passage once it confronts the pressure side of the potential flow field of the downstream rotor it will be re-directed upwards and inside the cavity. Part of the flow will pass through the gap over to the first closed cavity. The major part consists the cavity vortex. As the vortex center circumferentially moves with approximately 80 percent of the shroud's speed, a spiral is formed and the fluid will exit the cavity after one stator pitch. The fluid exits to fill in the gap of the low-pressure fluid of the stator wake. Inside the cavity, on both the upper corners a counter-rotating vortex is located.

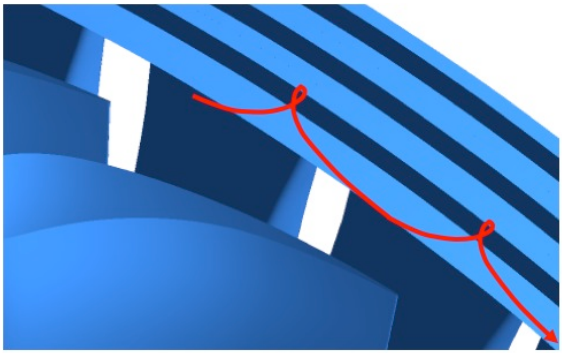

Figure 7.1: Rotor inlet cavity flow model.

Although the mass flow that enters the cavity is guided by the stator, the rotor regulates the in and out flows. Both the stator and the rotor influence the cavity flows. A zone of influence extends on either side for both the stator and the rotor. This zone extends approximately 60% on either side and was made evident through the different stator-rotor blade count. Reducing the axial to radial cavity wall length ratio by extending the upper casing stator platform results in reducing the influence of the stator exit pressure field on the cavity flows. On the other hand, the ellipsoidal cavity vortex as it gets squeezed it finally breaks up into two smaller vortices vertically aligned (Figure 7.2). Aerodynamic losses will decrease as long as the lower part of the vortex is close to the cavity entrance but not exceeding the later. Minimizing the axial to radial cavity wall length ratio acts beneficially till the point where zone of influence of the rotor is reached. That is 35-40 percent from the stator side. The vortex at that point is eliminated and radial jets dominate the in and outflows instead. The jets abruptly wash out the cavity plenum as they are only controlled by the rotor.

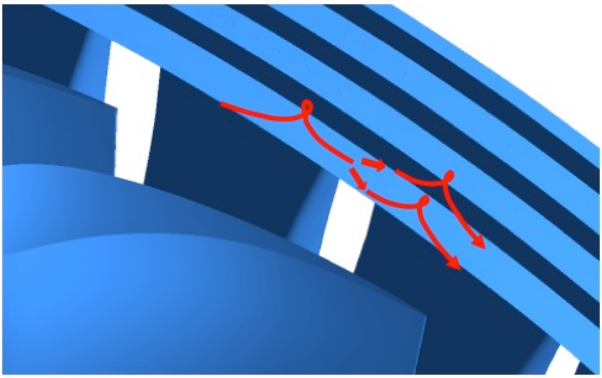

Figure 7.2: Rotor inlet cavity flow model when axial to radial cavity wall length leads to the formation of two vortices vertically aligned.

On the other hand, a square-shaped cavity leads to higher performance through better control of the cavity vortex. The closest the vortex gets to the cavity inlet the better performance is achieved. If the lower part of the vortex is at the cavity entrance there is no need for the flow that is to enter and exit the cavity to be redirected from the axial to radial direction, consuming energy and introducing additional losses. Especially while exiting the cavity if a radial distance is to be covered the flow is accelerated in the radial direction increasing the strength of the correspondent velocity vector leading to greater mismatch between cavity and main flows while re-entering the main flow area.

Nevertheless, as the size of the cavities is merely controlled by the axial thrust during operation and the thermal growth of the materials used, great care needs to be undertaken so as to avoid contact between the rotating and stationary parts. Following the main conclusion drawn out of this study of the square-shaped cavity having a comparative advantage over the rectangular ones, the necessary space for the turbine designer is given to reduce the radial height of the cavities without endangering an undesirable contact of the rotating and stationary parts. Bearing in mind that in HP turbines the aspect ratio is 1-2 and that an axial cavity gap of 50% of the bladerow spacing is used to ensure a safe operation, a square-shaped cavity would require a radial cavity height of 10-15% of the blade span in HP turbines. The percentage will drastically decrease in LP turbines where the aspect ratio is in the order of 4. Additionally, to be considered is the stator blade count as there is a direct

influence on the pitch size of the cavity vortex helix formed and therefore the leakage flow re-entry flow path angle.

Overall, modern sealing arrangements have reduced leakage fractions considerably, meaning that further improvements can only be obtained by controlling the leakage flow in such a way so as to minimize the aerodynamic losses incurred by the extraction and re-injection of the leakage flow into the mainstream and therefore the entropy generated because of the mixing process at the interaction area. The shape and volume cavity modifications examined in this study revealed their important role of reducing the aerodynamic losses in steam turbines. The cumulative conclusion drawn out of this work is that a square-shaped rotor inlet cavity that pushes the cavity vortex towards the vicinity of the interaction zone leads to increased stage performance.

The modifications as presented in this work can be materialized in real steam turbines in the form of rings that will be added in the existing designs. The fact that simple design rings can be installed and modify the cavity geometry accordingly makes the conclusions of this work relatively realizable, in terms of manufacturing cost and assembly time. Based on the simple concept of confining the cavity vortex in a square-shaped cavity with its lower side being close to the interaction zone the turbine designer can incorporate these modifications adjusting the existing design.

Future Work

The results of this study made evident the importance of the rotor inlet cavity design on turbine efficiency. It has been shown that cavity volume and length scale little influence have on the amount of leakage flow itself. Nevertheless, they considerably impact the mixing process occurring at the interaction zone. With reducing mass flux oscillations efficiency increases. Another important parameter that influences the mass flux oscillations is the radial position of the cavity vortex. The continuous presence of the vortex should be ensured, which should not however exceed the cavity volume into the main flow area.

The cavity vortex should be as close to the cavity inlet area. It is therefore suggested that the radial cavity wall length is reduced further till the lower side of the vortex reaches the cavity inlet. In such a way there will be no need for radial transport of the fluid that enters the cavity hence reduced torque loss and less mixing due to the re-direction (from axial to radial to axial) and weaker radial jets. Additionally, it is suggested to simultaneously reduce the axial and radial wall length that would break the cavity vortex into two smaller vertically aligned and bring the lower vortex close to the cavity inlet area.

It is additionally suggested to study the influence of the stator blade count on the leakage flow path. As the stator pitch regulates the pitch of the cavity vortex helix and therefore the re-entry flow path angles the number of stator blades can be used to correctly tune the size and position of the cavity vortex.

The shroud shape including the shroud platform should be reconsidered through a parametric study. The backwards-inclined surface of the shroud assists in the re-direction of the fluid that enters the cavity increasing the axial velocity component towards upstream. The fluid is accelerated and mixing is increased. A vertical surface with rounded edges or even forward inclined would eliminate the jet that generates losses through mixing.

The stator-rotor distance should be reconsidered to allow for multiplane probe accessibility. Unsteady pressure and entropy measurements will allow for an experimental quantification of the loss generated by the cavity vortex through its stretching both in space and time.

Further efficiency increase can be achieved through examining the rotor exit cavity flow field. A parametric study on the volume and length scale should be carried out. Mixing losses because of the re-entry of the leakage

mass flow impose heavy disturbance on the upper 10-15 percent of the downstream bladerow.

REFERENCES

[1] www.eia.doe.gov/iea/elec.html

[2] www.airports.org

[3] Adami, P., Martelli, F. and Cecchi, C., 2007, "Analysis of the Shroud Leakage Flow and Mainflow Interactions in High-Pressure Turbines Using an Unsteady Computational Fluid Dynamics Approach," Proceedings of the Institution of Mechanical Engineers, Part A: Journal of Power and Energy, Vol. 221, pp. 837-848

[4] Ainsworth, R. W., Allen, J. L. and Batt J. J. M., 1995, "The Development of Fast Response Aerodynamic Probes for Flow Measurements in Turbomachinery," ASME journal of Turbomachinery, vol. 117, pp. 625-634

[5] Anker, J. E., Mayer, J. F. and Casey, M. V., 2005, "The Impact of Rotor Labyrinth Seal Leakage Flow on the Loss Generation in an Axial Turbine," Proceedings of the Institution of Mechanical Engineers, Part A: Journal of Power and Energy, Vol. 219, pp. 481-490

[6] Barmpalias, K. G., Kalfas, A. I., Abhari, R. S., Hirano, T. and Shibukawa, N., 2010, "Effects of Design Variations of Rotor Entry Cavity Geometry on Shrouded Steam Turbine Performance," Proceedings of the ASME, paper No. GT2010-22279

[7] Becz, S., Majewski, M. S. and Langston, L. S., 2003, "Leading Edge Modification Effects on Turbine Cascade Endwall Loss," Proceedings of the ASME, paper No. GT2003-38898

[8] Behr, T., 2007, "Control of Rotor Tip Leakage and Secondary Flow by Casing Air Injection in Unshrouded Axial Turbines," PhD Thesis, diss. ETH No. 17283

[9] Binder, A., Foster, A., Mach, K. and Rogge, H., 1987, "Unsteady Flow Interaction Caused by Stator Secondary Vortices in a Turbine Rotor," Journal of Turbomachinery, Vol. 109, pp. 251-257

[10] Brenner, M. W., Sjolander, S. A. and Moustapha, S. H., 2003, "The Influence of Leading-Edge Geometry on Secondary Losses in a Turbine Cascade at the Design Incidence," Proceedings of the ASME, paper No. GT2003-38107

[11] Brouckaert, J. F., Sieverding, C. H. and Manna, M., 1998, "Development of a Fast-Reponse 3-Hole Pressure Probe," Proceedings of the 14th Symposium on Measuring Techniques for Transonic and Supersonic Flows in Cascades and Turbomachines, Limerick, Ireland

[12] Chaluvadi, V. S. P., Kalfas., A. I. and Hodson, H. P., 2001, "Blade Row Interaction In a High-Pressure Steam Turbine," Journal of Turbomachinery, Vol. 125, pp. 14-24

[13] Chaluvadi, V. S. P., Kalfas, I. A. and Hodson, H. P., 2003, "Vortex Transport and Blade Interactions in High Pressure Turbines," Proceedings of the ASME, paper No. GT2003-38389

[14] Denton, J. D., 1993, "Loss Mechanisms in Turbomachines," The 1993 IGTI Scholar Lecture, Journal of Turbomachinery, Vol. 115, pp. 621-656.

[15] Egli, A., 1935, "The Leakage of Steam Through Labyrinth Seals," Transactions of the ASME, Vol. 57, pp. 115-122

[16] Epstein A. H., 1985, "High Frequency Response Measurements in Turbomachinery," Measurements Techniques in Turbomachinery, VKI Lecture Series

[17] Evans, N. M., Hayton, P. and Hill, S. P., 1995, "Gas Turbine Blade having Improved Thermanl Stress Cooling Ducts," US Patent 4560486 October 24

[18] Farenkopf, D., 2006, "Applications of the GUM-method in the Field of Turbomachinery," Semester Thesis for the Institute of Energy Technology, Laboratory of Energy Conversion, Zürich, Switzerland

[19] Fujita, H. and Kovasznay, L. S. G., 1968, "Measurements of Reynolds Stress by a Single Rotated Hot Wire Anemometer," The review of Scientific Instruments, Vol. 39, No. 9, pp. 1352-1355

[20] Gier, J., Stubert, B., Brouillet, B. and de Vito, L., 2005, "Interaction of Shrouded Leakage Flow and Main Flow in a Three-Stage LP Turbine," ASME Journal of Turbomachinery, Vol. 125, pp. 649-658

[21] Goldstein, R. J. and Spores., R. A., 1988, "Turbulent Transport on the Endwall in the Region Between Adjacent Turbine Blades," Journal of Heat Transfer, Vol. 110, pp. 862-869

[22] Gossweiler, C., Humm, H. J. and Kupferschmied, P., 1990, "The Use of Piezoresistive Semi-Conductor Pressure Transducer for Fast-Response Probe Measurements in Turbomachinery," Proceedings of the 10th Symposium on Measuring Techniques for Transonic and Supersonic Flows in Cascades and Turbomachines, Brussels, Belgium

[23] Gossweiler, C., Herter, D. and Kupferschmied, P., 1992, "Fast-Response Aerodynamic Probe Measurements in a Turbulent Pipe Flow," Proceedings of the 11th Symposium on Measuring Techniques for Transonic and Supersonic Flows in Cascades and Turbomachines, Münich, Germany

[24] Gregory-Smith, D. G., Graves., C. P. and Walsh, J. A., 1988, "Growth of Secondary Losses and Vorticity in an Axial Turbine Cascade," Journal of Turbomachinery, Vol. 110, pp. 1-8

[25] Gregory-Smith, D. G., Ingram, G. and Jayaraman, P., Harvey, N. W. and Rose, M. G., 2001, "Non-Axisymetric Turbine Endwall Profiling," Proceedings of the Institution of Mechanical Engineers, Part A: Journal of Power and Energy, Vol. 215, pp. 721-734

[26] Hawthorne, W. R., 1951, "Secondary circulation in fluid flow," Proceedings of the Royal Society A, Vol. 206, pp. 374-387

[27] Hawthorne, W. R., 1955, "Rotational Flow Through Cascades Part I – The Components of Vorticity," Journal of Mechanics and Applied Mathematics, Vol. 8, pp. 266-279

[28] Heneka, A., 1983 “Entwicklung und Erprobung einer Keilsonde für Instationäre Dreidimensionale Strömungsmessungen in Turbomaschinen,” PhD Thesis, Stuttgart

[29] Hodson, H. P. and Dawes, W. N., 1998, “On the Interpretation of Measured Profile Losses in Unsteady Wake-Turbine Blade Interaction Studies,” ASME Journal of Turbomachinery, Vol. 120, pp. 276-284

[30] Hodson, H. P. and Howell, R. J., 2005, “Bladerow Interactions, Transition and High-Lift Aerofoils in Low-Pressure Turbines,” Annual Reviews of Fluid Mechanics, Vol. 37, pp. 71-98

[31] Howell, R. J., Ramesh, O. N., Hodson, H. P., Harvey, N. W. and Schulte, V., 2001, “High Lift and Aft Loaded Profiles for Low Pressure Turbines,” Journal of Turbomachinery, Vol. 123, pp. 181-188

[32] Hunter, S. D. and Manwaring, S. R., 2000, “Endwall Cavity Flow Effects on Gas Path Aerodynamics in an Axial Flow Turbine: Part 1 - Experimental and Numerical Investigation,” Proceedings of ASME 2000-GT-651

[33] ISO Guide to the Expression of Uncertainty in Measurement (GUM). Interanational Organization for Standardisation (Geneva, Switzerland), ISBN 92-67-1011889, 1st edition, 1993

[34] Janke, E., Haselbach, F., Whitney, C.,Kanjirakkad, V., Thomas, R. and Hodson, H., 2006, “Passive Shroud Cooling Concepts for HP Turbines: CFD Based Design Approach,” Proceedings of ASME GT2006 – 91194

[35] Kanjirakkad, V., Thomas, R., Hodson, H., Janke, E., Haselbach, F. and Whitney, C., 2008, “Passive Shroud Cooling Concepts for HP Turbines: Experimental Investigations,” Journal of Turbomachinery, Vol. 130, pp. 011017-1-9

[36] Kerrebrock, J. L., Thomkins, W. T. and Epstein, A. H., 1980, “A Miniature High Sphere Probe,” Measurements methods in Rotating Components of Turbomachinery, Lakshminarayama Ed. B. and Runstandler P. W. (New York ASME)

[37] Kupferschmied, P., 1998, "Zur Methodik zeitaufgelöster Messungen mit Strömungssonden in Verdichtern und Turbinen," PhD Thesis, Diss. ETH No. 12474, Zuerich, Switzerland

[38] Langston, L.S., Nice, M. L., and Hooper, R. M., 1977, "Three-Dimensional Flow Within a Turbine Cascade Passage," Journal of Engineering for Power, Vol. 99, pp. 21-28

[39] Langston, L.S., 1980, "Crossflows in a Turbine Cascade Passage," Journal of Engineering for Power, Vol. 102, pp. 866-874

[40] Langston, L.S., 2001, "Secondary Flows In Axial Turbines – A Review," Annals of the New York Academy of Sciences, Vol. 934(1), pp. 11-26

[41] Laufer, J., 1975, "The Structure of Turbulence in Fully Developed Pipe Flow," National Advisory Committee for Aeronautics, Technical report No. 1174

[42] Lenherr, C., Kalfas, A. I. and Abhari, R. S., 2007, "A Flow Adaptive Aerodynamic Probe Concept for Turbomachinery," Measurement Science and Technology Vol. 18, pp. 2599-2608

[43] Lehmann, K., Thomas, R., Hodson, H. and Vassilis S., 2009, "Heat Transfer and Aerodynamics of Over-Shroud Leakage Flows in a High Pressure Turbine," Proceedings of ASME GT2009 – 59531

[44] Li, J., Yan, X., LV, Q., Xie, Y. and Feng Z., "The Effect of the Shrouded Rotor Blade Tip Leakage Flow on the Aerodynamic Performance of a One and Half Turbine Stage," Challenges of Power Engineering and Environment, Vol. 5, pp. 275-280

[45] Limmat Scientific AG, Pneumatic Measurement System, User Manual

[46] Mahle, I., 2010, "Improving the Interaction Between Leakage Flows and Main Flow in a Low Pressure Turbine," Proceedings of the ASME, paper No. GT2010-22448

[47] Matsubaga, S., Ishibashi, H. and Nishi, M., 1978, "Accurate Measurements of Non-Steady Three Dimensional Incompressible Flow by Means of a Combined Five Hole Probe," Non-Steady Fluid Dynamics, Winter ASME Meeting, San Fransisco

[48] Meyer, R. X., 1958, "The Effect of Wakes on the Transient Pressure and Velocity Distributions in Turbomachines," Journal of Basic Engineering, Vol. 80, pp. 1544-42

[49] Parker, R. and Watson, J. F., 1972, "Interaction Effects Between Blade Rows in Turbomachines," Proceedings of the Institution of Mechanical Engineers, Vol. 186, pp. 331-340

[50] Pau, M., Cambuli, F. and Mandas, N., 2008, "Shroud Leakage Modeling of the Flow in a Two-Stage Axial Test Turbine," Proceedings of the ASME, paper No. GT2008-51093

[51] Perdichizzi, A. and Dossena, V., 1993, "Incidence Angle and Pitch-Chord Effects on Secondary Flows Downsrteam of a Turbine Cascade," ASME Journal of Turbomachinery, Vol. 115, pp. 383-391

[52] Peters, P., Giboni, A., Menter, J. R., Pfost, H. and Wolter, K., 2005, "Unsteady Interaction of Labyrinth Seal Leakage Flow and Downstream Stator Flow in a Shrouded 1.5 Stage Axial Turbine," Proceedings of ASME GT2005-68065

[53] Pfau, A., 2003, "Loss Mechanisms in Labyrinth Seals of Shrouded Axial Turbines," PhD Thesis, Diss. ETH No. 15226

[54] Pfau, A., Kalfas, A. I. and Abhari, R. S., 2004, "Making use of Labyrinth Interaction Flow," Proceedings of ASME GT2004-53797

[55] Pfau, A., Schlienger, J., Kalfas, A. I. and Abhari, R. S., 2003, "Unsteady Flow Interactions within the Inlet Cavity of a Turbine Rotor Tip Labyrinth Seal," Proceedings of ASME GT2003-38271

[56] Pfau, A., Schlienger, J., Kalfas, A. I. and Abhari, R. S., 2003, "Unsteady, 3-Dimensional Flow Measurement using a Miniature Virtual 4-

sensor Fast Response Aerodynamic Probe (FRAP)," Proceedings of ASME GT2003-38128

[57] Porreca, L., 2007, "Aerothermal Optimization of Partially Shrouded Axial Turbines," PhD Thesis, Diss. ETH No. 17138

[58] Rhode, D. L., Johnson, J. W. and Broussard, D. H., 1997, "Flow Visualization and Leakage Measurements of Stepped Seals: Part 1 – Annular Groove," Journal of Turbomachinery, Vol. 119, pp 839-848

[59] Rhode, D. L., Johnson, J. W. and Broussard, D. H., 1997, "Flow Visualization and Leakage Measurements of Stepped Seals: Part 2 – Sloping Surfaces," Journal of Turbomachinery, Vol. 119, pp. 844-848

[60] Rosic, B. and Denton, J. D., 2008, "Control of Shroud Leakage Loss by Reducing Circumferential Mixing," ASME Journal of Turbomachinery, Vol. 130, pp. 021010-1 – 021010-7

[61] Rosic, B., Denton, J. D. and Curtis, E. M., 2007, "The Influence of Shroud and Cavity Geometry on Turbine Performance – An Experimental and Computational Study, Part 1: Shroud Geometry," Proceedings of ASME GT2007 – 27769

[62] Sauer, H., Müller, R., and Vogeler, K., 2001, "Reduction of Secondary Flow Losses in Turbine Cascades by Leading Edge Modifications at the Endwall," ASME Journal of Turbomachinery, Vol. 123, pp. 207-213

[63] Schlienger, J., 2003, "Evolution of unsteady Secondary Flows in a Multistage Shrouded Axial Turbine," PhD Thesis, Diss. ETH No. 15230

[64] Schlieger, J., 2003, "Evolution of Unsteady Secondary Flows in a Multistage shrouded Axial Turbine," PhD Thesis, Diss. ETH No. 15230, Zuerich, Switzerland

[65] Schlienger, J., Kalfas, A. I. and Abhari, R. S., 2004, "Vortex-Wake-Blade Interaction in a Shrouded Axial Turbine," Proceedings of ASME GT-2004-53915

[66] Schlienger, J., Pfau, A., Kalfas, A. I. and Abhari, R. S., 2003, "Effects of Labyrinth Seal Variation on Multistage Axial Turbine Flow," Proceedings of ASME GT2003-38270

[67] Seeno, Y., Kita, Y. and Ookuma, K., 1973, "Measurements of Two-Dimensional Periodic Flow With a Cobra Probe," Journal of Fluids Engineering, pp. 295

[68] Sharma, O. P. and Butler, T. L., 1987, "Predictions of Endwall Losses and Secondary Flows in Axial Flow Turbine Cascades," Journal of Turbomachinery, Vol. 109, pp. 229-236

[69] Sharma, O. P., Butler, T. L., Joslyn, H. D. and Dring, R. P, 1985, "Three-Dimensional Unsteady Flow in an Axial Flow Turbine," Journal of Propulsion, Vol. 1, pp. 29-38

[70] Sieverding, C. H., 1985, "Recent Progress in the Understanding of Basic Aspects of Secondary Turbine Blade Passages," Journal of Engineering for Gas Turbines and Power, Vol. 107(2), pp. 248-257

[71] Smith, L. H., 1966, "Wake Dissipation in Turbomachines," Journal of Basic Engineering, Vol. 88, pp. 688-690

[72] Solomon, W. J., 2000, "Effects of Turbulence and Solidity on the Boundary Layer Development in a Low Pressure Turbine," Proceedings of ASME, 2000-GT-273

[73] Song, B., Wing, F. N., Controneo, J. A., Hofer, D. C. and Siden, G., 2004, "Aerodynamic Design and Testing of Three Low Solidity Steam Turbine Nozzle Cascades," Proceedings of ASME, GT2004-53329

[74] Tashima, T., Sasaki, T., Kalfas, A. I. and Abhari, R. S., 2007, "Blade Loading Influence on Unsteady Flow Interactions in Axial Steam Turbines," Proceedings of ASME, GT2007-27452

[75] Traupel, W., 1973. Thermische Turbomaschinen. Springer-Verlang, Berlin

[76] U.S. Energy information Administration

[77] Vakili, A. D., Meganathan, A. J., Michaud, M. and Radhakrishnan, S., 2005, "An Experimental and Numerical Study of Labyrinth Seal Flow," Proceedings of ASME GT2005-68224

[78] Wallace, I. and Davies, M., 1996, "Turbulence Measurements With a Calibrated Pitot Mounted Pressure Transducer," Proceedings of the 13th Symposium on Measuring Techniques for Transonic and Supersonic Flows in Cascades and Turbomachines, Zürich, Switzerland

[79] Wallis A. M., Denton J. D. and Demargne A. A. J., 2001, "The Control of Shroud Leakage Flows to Reduce Aerodynamic Losses in a Low Aspect Ratio Shrouded Axial Flow Turbine," Journal of Turbomachinery, Vol. 123, pp. 334-341

[80] Wang, H. P., Olson., S. J., Goldstein, R. J. and Eckert, E. R. G., 1997, "Flow Visualization in a Linear Turbine Cascade of High Performance Turbine Blades," Journal of Turbomachinery, Vol. 119, pp. 1-8

[81] Wellborn, S. R. and Okiishi, T. H., 1999, "The Influence of Shrouded Stator Cavity Flows on Multistage Compressor Performance," Journal of Turbomachinery, Vol. 121, pp. 486-497

NOMENCLATURE

Symbols

a	cavity's axial wall length
b	cavity's radial wall length
c	normalized cavity axial length
C	blade chord
C_p	specific heat
C_{pt}	pressure coefficient $(P_t - P_{s,exit})/(P_{t,inlet} - P_{s,exit})$
C_z	axial chord length
D	probe head diameter
Eff	efficiency
F	force
h	normalized blade span
$\dot{m}$	massflow
P	pressure
r	radius
r_z	radius of the streamline
s	non dimensional streamwise direction
R1	1st rotor
R2	2nd rotor
SB	swirl brakers
S1	1st stator
S2	2nd stator
T	temperature
v	velocity
V	volume
y^+	dimensionless wall distance
z	axial direction
Z	normalized stator rotor distance
θ	circumferential direction
σ	solidity

Greek

α	absolute flow yaw angle

γ	flow pitch angle
η	efficiency
ρ	density
ω	torque

Subscripts

2nd,stage	second stage
exit	turbine exit condition
inlet	turbine inlet condition
max	maximum
r	radial direction
R	rotor
s	static
S	stator
t	total
z	axial direction
θ	tangential direction

Abbreviation

5HP	five hole probe
CFD	computational fluid dynamic
CV	cavity volume
ConV	control volume
CVR	cavity volume reduction
EXP	experiment
FRAP	fast response aerodynamic probe
HS	high solidity
LE	leading edge
LS	low solidity
PIV	particle image velocimetry
TE	trailing edge
Δeff	efficiency difference

LIST OF PUBLICATIONS

Barmpalias, G. K., Chokani, N., Kalfas, I. A. and Abhari, S. R., 2006, "Estimation of Spectra by a Data Adaptive Spectral Method," Proceedings of the 18th Symposium on Measuring Techniques for Transonic and Supersonic Flows in Cascades and Turbomachines, Thessaloniki, Greece

Barmpalias, G. K., Kalfas, I. A., Chokani, N. and Abhari, S. R., 2008, "The Dynamics of the Vorticity Field in a Low Solidity Axial Turbine," Proceedings of the ASME Turbo Expo, Paper No. GT2008-51142, Berlin, Germany

Barmpalias, G. K., Kalfas, I. A., Abhari, S. R., Hirano, T. and Shibukawa, N., 2010, "Effects of Designs Variations of Rotor Entry Cavity Geometry on Shrouded Steam Turbine Performance," Proceedings of the ASME Turbo Expo, Paper No. GT2010-22279, Glasgow, Scotland

Barmpalias, G. K., Kalfas, I. A., Abhari, S. R., Hirano, T., Shibukawa, N. and Sasaki, T., 2011, "Design Considerations for Axial Steam Turbine Rotor Inlet Cavity Volume and Length Scale," Proceedings of the ASME Turbo Expo, Paper No. GT2011-45127, Vancouver, Canada (accepted for publication in ASME Journal of Turbomachinery

Barmpalias, G. K., Kalfas, I. A., Abhari, S. R. and Shibukawa, N., 2011, "Impact of Rotor Inlet Cavity Geometry on Shrouded Turbine Performance," The 9th European Turbomachinery Conference on Turbomachinery Fluid Dynamics and Thermodynamics, Istanbul, Turkey

Barmpalias, G. K., Kalfas, I. A., Abhari, S. R., Shibukawa, N. and Sasaki, T., 2011, "Intergraded Design of Rotor Leading Edge and Cavity Flows in an Axial shrouded Turbine," International Society for Airbreathing Engines, Gohenburg, Sweden

Barmpalias, G. K., Kalfas, I. A., Abhari, S. R., Hirano, T., Shibukawa, N. and Sasaki, T., 2011, "Controlling Mixing at the Interaction Zone Through Systematic Variation of the Inlet Rotor Cavity Volume and Length Scale," International Gas Turbine Congress 2011 Osaka, 10th Congress in Japan

CURICULUM VITAE

Personal data

Name	Barmpalias G. Konstantinos
Born	02 May 1980, Thessaloniki, Greece
Citizenship	Greek

Education

1993-1998	Nineteenth high school of Thessaloniki, Greece
1999-2005	Bachelor's and Master's studies in the Department of Mechanical Engineering, School of Engineering, Aristotle University of Thessaloniki, Greece
2006-2011	Doctoral studies at the Laboratory for Energy Conversion in the Department of Mechanical and Process Engineering at the Swiss Federal Institute of Technology Zurich, Zurich, Switzerland